Case Study: Settlement at Nepal Hydropower Dam during the 2014-2015 Gorkha Earthquake Sequence

Ailie Marie Vuper

Thesis submitted to the faculty of the Virginia Polytechnic Institute and State University in partial fulfillment of the requirements for the degree of

Master of Science
In
Civil Engineering

Russell A. Green, Chair
James K. Mitchell
Adrian Rodriguez-Marek

Feb. 26, 2021
Blacksburg, VA

Keywords: Seismic Compression, Expanded Byrne Model, Liquefaction

Case Study: Settlement at Nepal Hydropower Dam during the 2014- 2015 Gorkha Earthquake Sequence

Ailie Marie Vuper

ABSTRACT

The Tamakoshi Dam in Nepal experienced 19 cm of settlement due to three earthquakes that took place from December 14, 2014 to May 12, 2015. This settlement caused massive damage and halted construction and was believed to have been caused by seismic compression. Seismic compression is the accrual of contractive volumetric strain in sandy soils during earthquake shaking for cases where the generated excess pore water pressures are low. The purpose of this case study is to investigate the settlements of the dam intake block relative to the right abutment block of the dam during the three earthquakes. Towards this end, soil profiles for the dam were developed from the boring logs and suites of ground motions were selected and scaled to be representative of the shaking at the base of the dam for the two of the three earthquakes which were well documented. Equivalent linear analysis was completed for the suites of ground motions to produce shear strain time histories which were then utilized in the Jiang et al. (2020) proposed procedure for seismic compression prediction. The results were found to not align with the settlement that was observed in the field, so post-liquefaction consolidation was also considered to be a possible cause of the settlement. The results from that analysis also showed that consideration of post-liquefaction consolidation did not yield settlements representative of those observed in the field. More detailed studies are recommended to assess the settlements that were observed at the dam site, particularly analyses that take into account below and above grade topographic effects on the ground motions and settlements at the ground surface.

Case Study: Settlement at Nepal Hydropower Dam during the 2014- 2015 Gorkha Earthquake Sequence

Ailie Marie Vuper

GENERAL AUDIENCE ABSTRACT

The Tamakoshi Dam in Nepal experienced 19 cm of settlement due to three earthquakes that took place from December 14, 2014 to May 12, 2015. This settlement caused massive damage and halted construction and was believed to have been caused by seismic compression. Seismic compression is the accrual of contractive volumetric strain in sandy soils during earthquake shaking for cases where the generated excess pore water pressures are low. The purpose of this case study is to investigate the settlements of the dam intake block relative to the right abutment block of the dam during the three earthquakes. Representative soil profiles were developed based on data collected from the site for analysis of the settlement. Two approaches were used to compute predicted settlement, one which considered only seismic compression as the cause of settlement and a hybrid method that considered both seismic compression and post-liquefaction consolidation. Both approaches predicted settlement values that were less than what was observed in the field. It was found that the ground motion prediction equations used in the analysis were not representative of the tectonic setting in Nepal and thus was the main reason for the under-prediction. The relevance of this research lies in using methodology developed in academia to analyze a real world event and draw conclusions about the methodology's applicability.

Table of Contents

List of Tables

List of Figures

Chapter 1: Introduction

The Upper Tamakoshi Hydroelectric Project began in 2007 and is projected to be the largest hydropower dam in Nepal. It is located in Lamabagar in the Dolakha District in the Central Development region of Nepal (UTHL 2020). The dam sits on the Tamakoshi River and is expected to generate 2,281 GWh per year with a maximum output of 456MW (UTHL 2020). The dam was subjected to shaking from three earthquakes that occurred from December 2014 through May 2015 and as a result, experienced 19 cm of settlement between the right abutment block and the dam intake block. The settlement caused extensive damage and halted construction of the dam until repairs could be completed. It is thought that the settlement was due to seismic compression because there was no evidence of the occurrence of liquefaction, although preservation of liquefaction manifestations at the site was far less than optimal due to precipitation and river flow. Seismic compression is the accrual of contractive volumetric strain in unsaturated or saturated sandy soils during earthquake shaking for cases where the generated excess pore water pressures are low (Jiang et al. 2020).

The three earthquakes that affected the Tamakoshi dam ranged in magnitude and distance from the dam site. The December 2014 earthquake had a moment magnitude (M_w) of 5.3 and its epicenter was approximately 21 km from the site. The April 2015 earthquake had M_w = 7.8 and its epicenter was 150 km away, and the May 2015 earthquake had M_w = 7.3 and its epicenter was 14 km away from the dam. The M_w7.8, April 2015 earthquake caused the most settlement, as well as the most damage to the dam and surrounding area. This included triggering a landslide that cut off road access to the dam (Hashash et al.

2015). The delays in construction of the dam were particularly detrimental because the Upper Tamakoshi Dam would help provide electricity to the citizens of Nepal who lack reliable electricity supply (Hashash et al. 2015).

The focus of this case study is to compare predicted versus observed settlements during the two larger events that impacted the dam site, because these events were well documented. This entailed evaluating seismic compression using the approach proposed by Jiang et al. (2020) and evaluating a combination of seismic compression and post-liquefaction consolidation using the Zhang et al. (2002) implementation of the Ishihara and Yoshimine (1992) approach.

Jiang et al. (2020) proposed the use of the Expanded Byrne Model for evaluating seismic compression which can be implemented in "simplified" and "non-simplified" manners, where the non-simplified implementation entails performing numerical site response analyses and the simplified implementation does not. The non-simplified implementation is used in this study. The soil profiles used in the analyses were derived from boring logs at the dam site, and the ground motions used were selected and scaled to predicted motions using the NGA-West2 Ground Motion Prediction Equations (GMPE). These scaled ground motions were used to compute shear strain time histories which were, in turn, used in the non-simplified Expanded Byrne Model to predict seismic compression.

Despite there being no evidence of liquefaction at the site following the events, liquefaction triggering is evaluated at the site to assess whether the predicted excess pore

water pressures are sufficient to cause post-liquefaction consolidation settlement. Note that the preservation of liquefaction manifiestion at the site was far less than optimal due to precipitation and river flow, and as a result the lack of observations of liquefaction manifestations does not necessarily mean that liquefaction did not trigger. Ishihara and Yoshimine (1992) developed a correlation relating post-liquefaction consolidation settlement to relative density (D_r) and factor of safety against liquefaction triggering (FS_{liq}). Zhang et al. (2002) modified the procedure by relating post-liquefaction consolidation settlement to penetration resistance and FS_{liq}, where FS_{liq} can be evaluated using the stress-based simplified procedure.

In the following, first an overview of approaches for evaluating seismic compression are presented, followed by a presentation of the simplified and non-simplified Expanded Byrne Models. The application of the Expanded Byrne Model, how representative ground motions were selected, scaled, and utilized to calculate shear strain time histories, and the predicted settlements are discussed. A hybrid analysis that considers both seismic compression and post-liquefaction consolidation is presented, including liquefaction evaluation, predicting the amount of post-liquefaction consolidation and comparing the result to the analysis that considers settlement to only be caused by seismic compression. The results are evaluated and compared to what was measured in the field and discussed. Finally, recommendations for future work are given.

Chapter 2: Background

2.1 Tamakoshi Dam Site

The Tamakoshi dam is in the lower region of the Higher Himalayas and sits on the Tamakoshi River, near the Nepal-Tibet border, as shown in Figure 2.1 (UTHL 2020). The dam sits on a thick alluvial deposit that is mostly comprised of fine to coarse sand with larger particles (gravel to boulders) scattered throughout. Figure 2.2 shows an overview of the dam site with important components of the dam and deep boring locations noted. Bedrock was encountered in one of the boreholes at the site at ~121 m below the ground surface, while the other borehole was terminated at ~113.5m before reaching bedrock. Standard Penetration Tests (SPT) were performed in both boreholes down to depths of ~100 m. These results were used to develop the two soil profiles that are used in this study to analyze seismic compression as shown in Figures 2.3 and 2.4. The SPT corrected "N-values" are shown in Figure 2.5 where the correction is for energy ratio, borehole diameter, overburden stress, rod length and omitting sampler liners. The small strain shear wave velocity values versus depth are shown in Figure 2.6. The data from the boring logs were evaluated and discretized to representative strata for each soil profile. In total, 27 soil categories based on the descriptions in the boring log and 105 soil strata were used to model Soil Profile 2 and 16 soil categories based on the descriptions in the boring log, and 129 soil strata were used to model Soil Profile 3.

Nepal sits on both the Indian and Eurasian tectonic plates which are currently converging with each other. As a result, this region is known for high amounts of seismicity (Hashash et al. 2015). There is not much information about the seismic hazard of the

Tamakoshi Dam site other than it was built 1 km upstream from a landslide dam that formed over 500 years ago (Tiwari et al. 2019).

Figure 2.1 Location of Tamakoshi Dam site (Karan, P.P., Encyclopedia Britannica 2021).

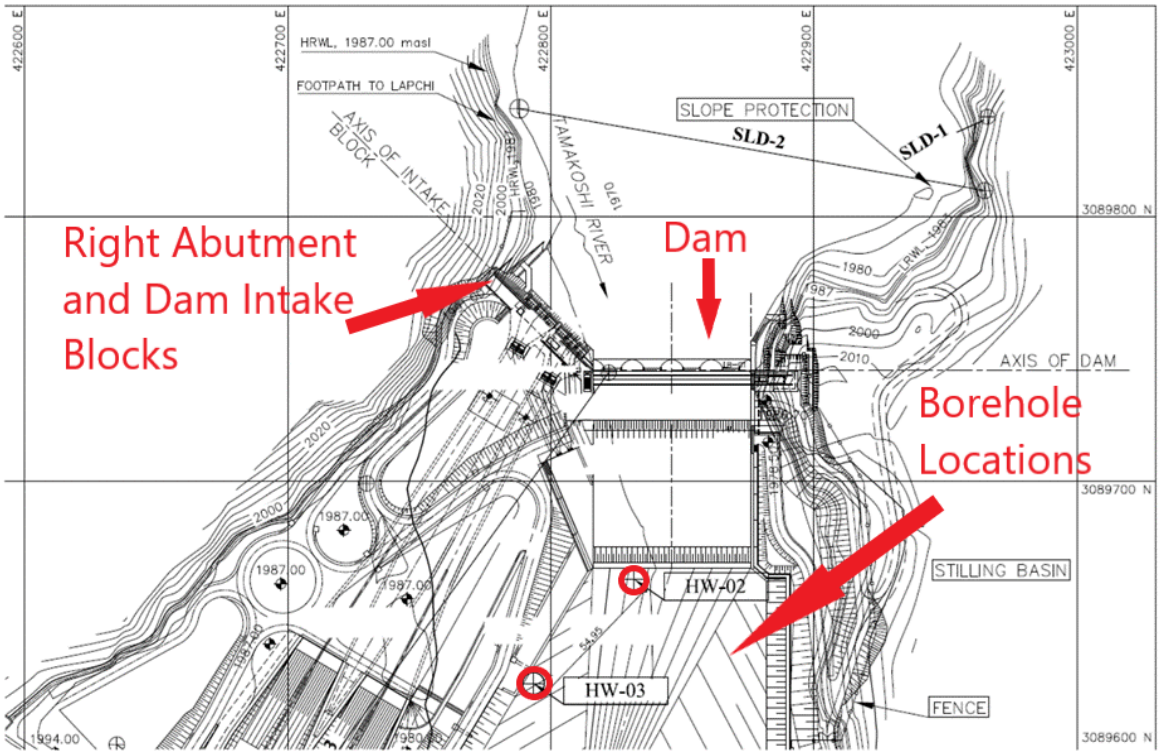

Figure 2.2 Borehole location from the 2016 field reconnaissance of the Tamakoshi Dam site (Tiwari et al. 2019)

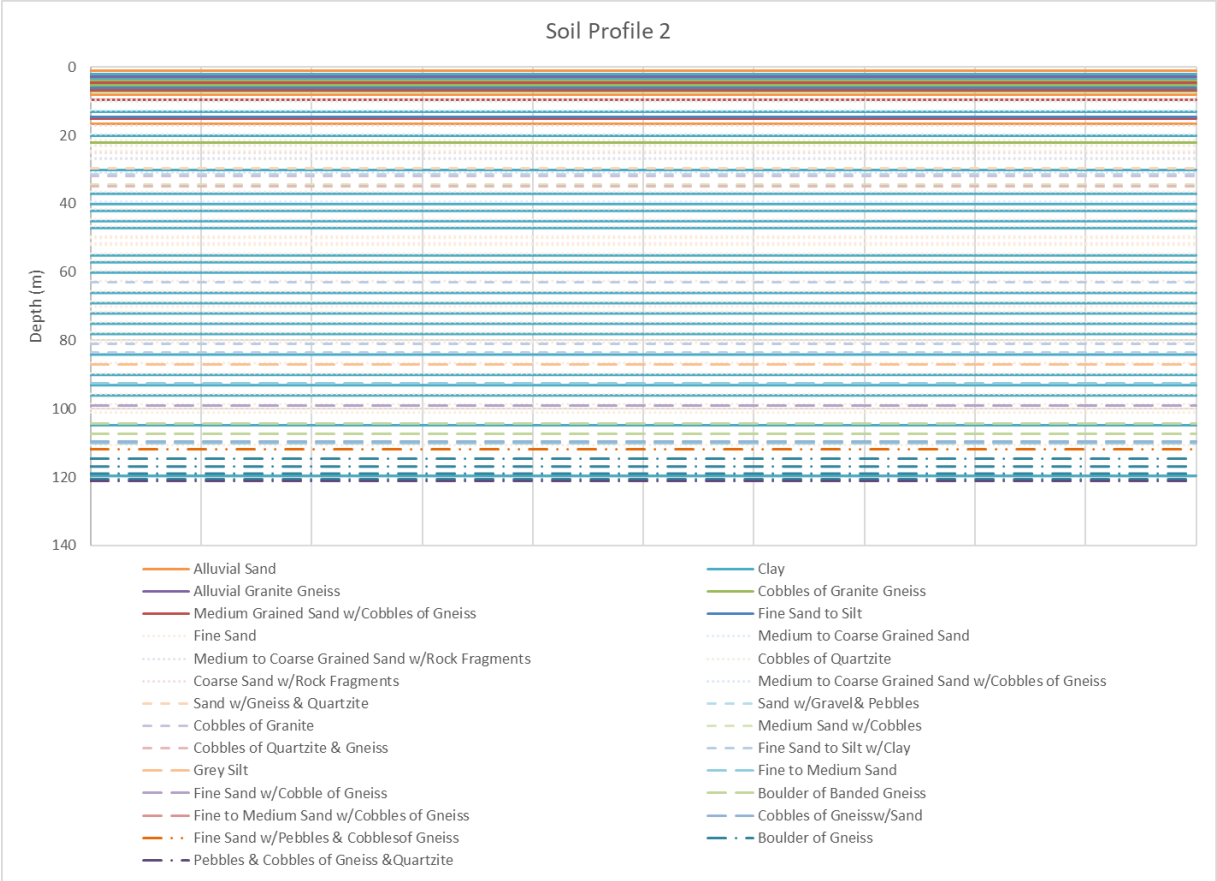

Figure 2.3 Discretized Soil Profile 2 developed from Boring Log 2.

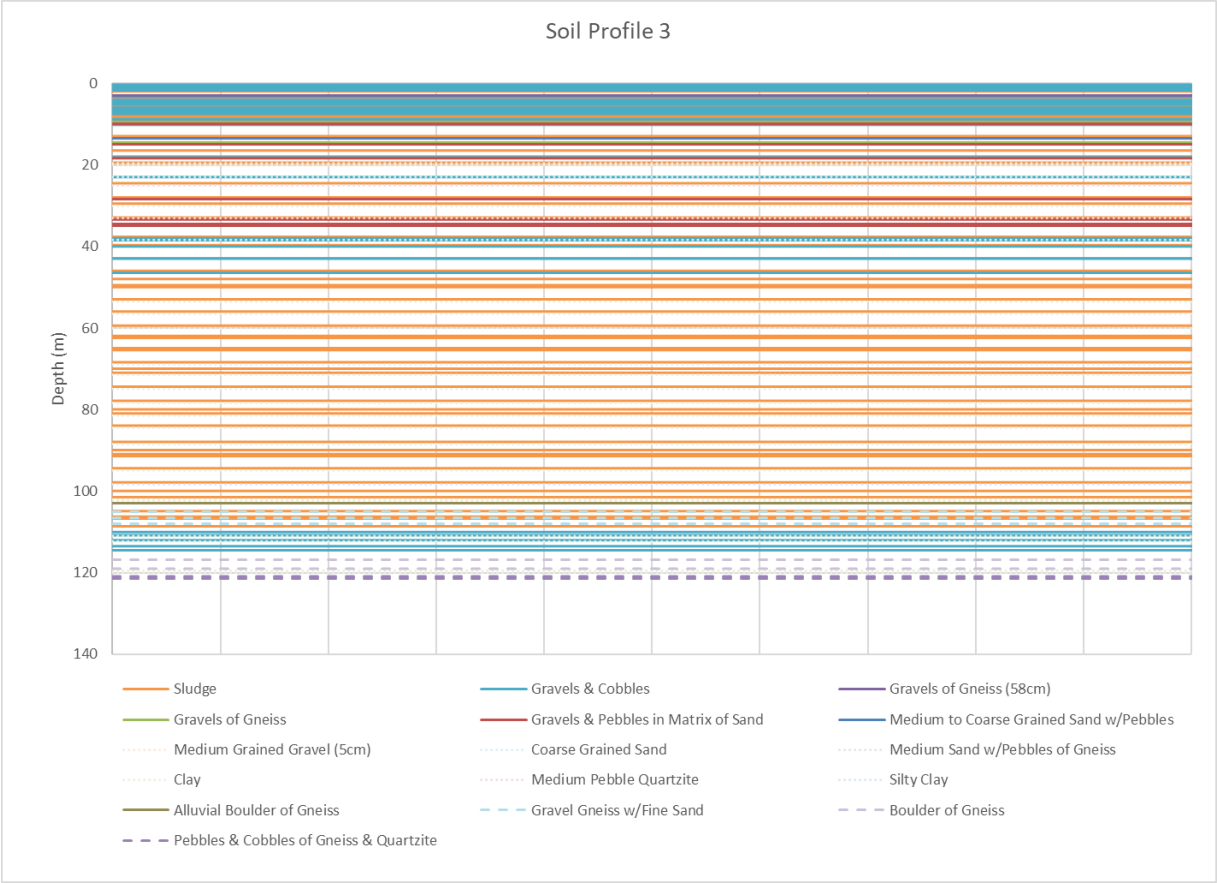

Figure 2.4 Discretized Soil Profile 3 developed from Boring Log 3.

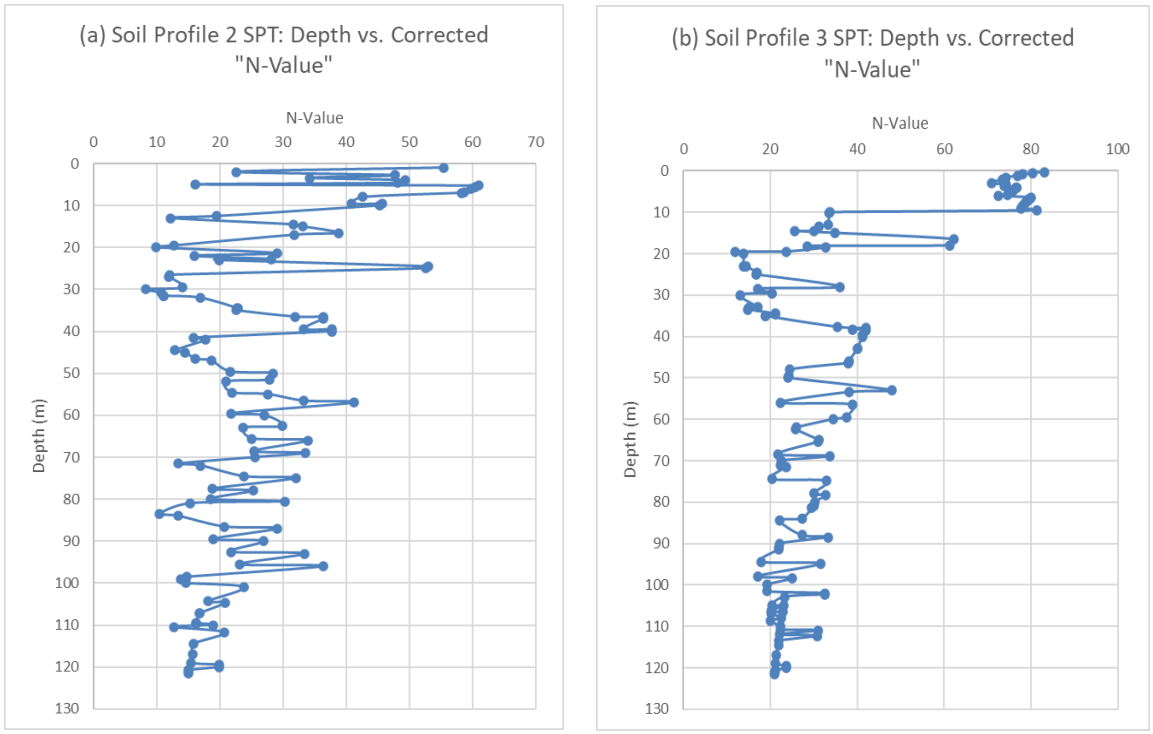

Figure 2.5 Corrected SPT "N-values" versus depth: (a) Soil Profile 2; (b) Soil Profile 3

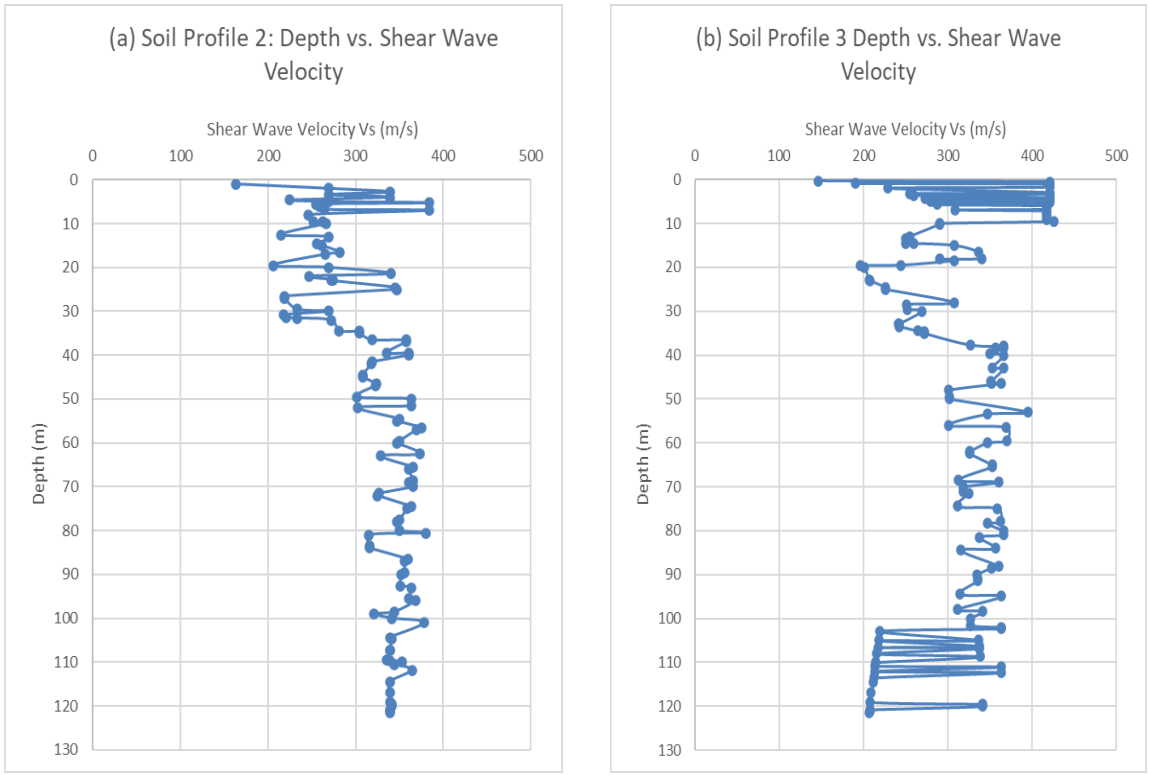

Figure 2.6 Small strain shear wave velocity determined using the relationship from Ulmer et al. (2020) versus depth: (a) Soil Profile 2; (b) Soil Profile 3.

2.2 Earthquake Sequence

The Tamakoshi Dam site was subjected to earthquake shaking from three earthquakes that occurred from December 2014 to May 2015. The first earthquake, an M_w5.3 event occurred on December 18, 2014 with its epicenter 21 km from site and resulted in 5 cm of settlement at the site. The second earthquake, an M_w7.8 event occurred on April 25, 2015 with its epicenter 150 km away from the dam site and resulted in an additional 11 cm of settlement at the site. The third and final event, an M_w7.3 aftershock of the April 25 event, occurred on May 12, 2015, and its epicenter was approximately 14 km from the dam site. An additional 3 cm of settlement occurred during this aftershock, totaling 19 cm of settlement for the three events. All settlements were measured between the right abutment block and dam intake block. Figure 2.7 shows the locations of the epicenters for all three earthquakes relative to the Tamakoshi Dam.

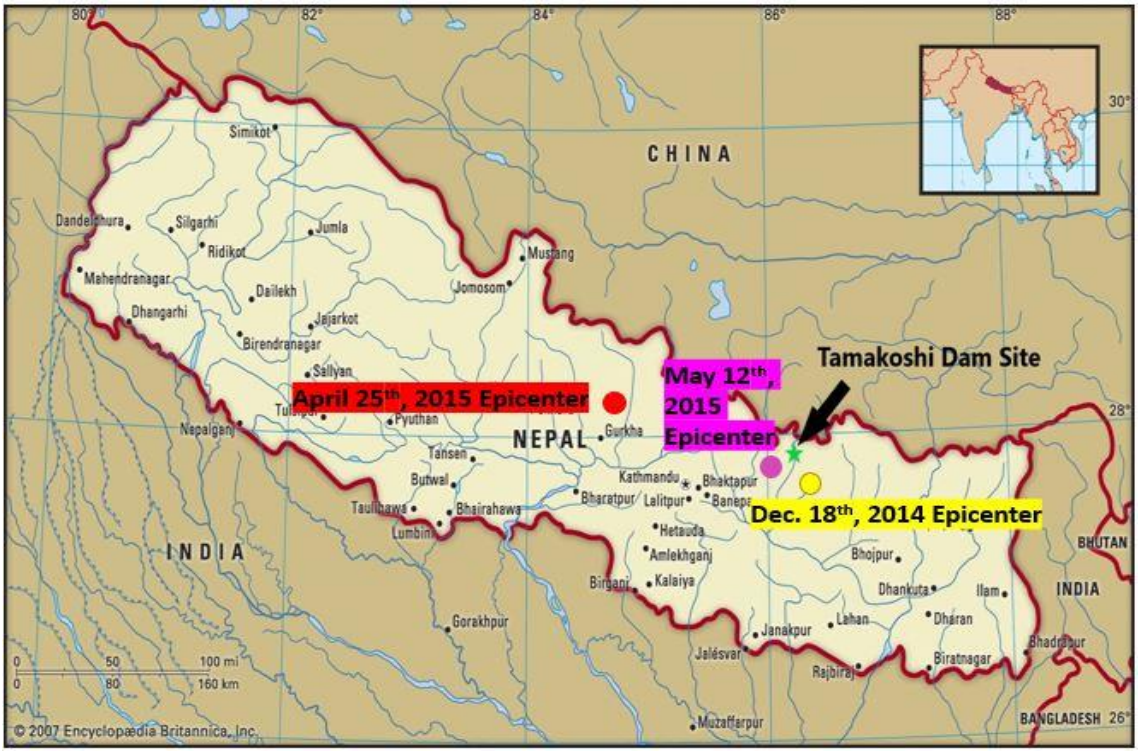

Figure 2.7 Relative location of the epicenters from the three earthquakes that affected the Tamakoshi Dam.

The M_w7.8 April 2015 and M_w7.3 May 2015 earthquakes were the result of two separate slips of the Main Himalayan Thrust (MHT) fault located near Kathmandu, Nepal (Moss et al. 2015). This fault is the underground convergence of three surface faults known as the Main Central Thrust fault, Main Boundary Thrust fault, and Main Frontal thrust fault, which subsequently divide the region into the Sub Himalaya, Lesser Himalaya, and High Himalaya (Seeber and Armbruster, 1981; DeCelles et al. 2002; Bollinger et al. 2006). The epicenter of the M_w7.8 April 2015 earthquake was located approximately 150 km away from the dam site and had a focal depth of 15 km (Hashash et al. 2015). The epicenter of the M_w7.3 May 2015 aftershock was located 14 km away from the dam site and was the result of further slip along the MHT (Hashash et al. 2015). Due to lack of information regarding the M_w5.3 December 18, 2014 earthquake, this study focuses on the settlement that occurred during the M_w7.8 April 25, 2015 main shock and M_w7.3 May 12, 2015 aftershock.

Due to lack of information regarding the M_w5.3 December 18, 2014 earthquake, this study focuses on the settlements that occurred during the M_w7.8 April 25, 2015 main shock and M_w7.3 May 12, 2015 aftershock.

2.3 Overview of Evaluating Seismic Compression

Procedures for evaluating seismic compression can be broadly classified as being "simplified" or "non-simplified" (Jiang et al. 2020). The difference between the two is the method of characterizing the seismic loading used in the analysis. For simplified procedures, seismic loading is generally characterized by amplitude and duration metrics, e.g., effective shear strain, γ_{eff}, and number of equivalent strain cycles, $n_{eq\gamma}$. In general,

numerical site response analyses are not required by simplified procedures to obtain, γ_{eff} and $n_{eq\gamma,}$ but rather correlations with seismic design parameters (e.g., peak ground acceleration, a_{max}, and earthquake magnitude, M_w) are used to estimate these variables. For non-simplified procedures, the seismic loading is characterized in much more detail, e.g., shear strain time histories, which are often computed via numerical and site response analyses, where seismic design parameters are used to select input motions for the analyses. The majority of the proposed of seismic compression models are simplified, with the state-of-practice simplified procedure being a modified/updated version of the Tokimatsu and Seed (1987) procedure (e.g., Duku et al. 2008).

The Tokimatsu and Seed (1987) model quantifies the seismic loading in terms of γ_{eff} and $n_{eq\gamma}$ to evaluate the magnitude of seismic compression. In this procedure, a reference magnitude of M_w7.5 is used, and correction factors are applied to the computed seismic compression for other magnitude events. Tokimatsu and Seed (1987) utilized laboratory data and the relationships developed by Silver and Seed (1971) and Seed and Silver (1972) to develop their seismic compression evaluation procedure. A group of researchers at UCLA (Duku et al. 2008, Yee et al. 2014), built upon this model by considering the influence of degree of saturation, relative density, fines content, plasticity index, effective overburden stress and overconsolidation ratio.

Jiang et al. (2020) expanded the Byrne (1991) cyclic shear-volumetric strain coupling model and calibrated it for evaluating seismic compression for multiple soil types in a non-simplified manner using the data from Duku et al. 2008 and Yee et al. 2014. Jiang et

al. (2020) also "transformed" Byrne (1991) to allow it to be implemented in a simplified manner. An overview of both the simplified and non-simplified variants of the Expanded Byrne Model are presented in the following.

The Byrne (1991) model is a variation on Martin et al. (1975) volumetric strain-shear strain coupling model for sand under drained conditions in which the cumulative volumetric strain is computed incrementally due to being subjected to a sequence of half cycles of shear strain loading.

$$\varepsilon_v = \sum_i \left(\Delta\varepsilon_{v,1/2}\right)_i \tag{1}$$

where ε_v is the cumulative volumetric strain (in percent) at the end of loading, and $\left(\Delta\varepsilon_{v,1/2}\right)_i$ is the volumetric strain (in percent) at the end of the i^{th} half-shear strain cycle of loading with amplitude of γ_i, where γ_i is taken as the peak shear strain between two zero crossings in the shear strain time history.

Per the Byrne (1991) model, $(\Delta\varepsilon_{v,1/2})_i$ is determined as:

$$\left(\Delta\varepsilon_{v,1/2}\right)_i = 0.5 \cdot (\gamma_i - \gamma_{tv}) \cdot C_1 \cdot exp\left[-C_2 \frac{\varepsilon_{vi}}{(\gamma_i - \gamma_{tv})}\right] \tag{2}$$

where γ_{tv} is threshold strain in percent, C_1 and C_2 are material-specific parameters, and ε_{vi} is the volumetric strain in percent at the beginning of the i^{th} load increment. Byrne (1991) provided correlations relating C_1 and C_2 to D_r and normalized SPT blow count ($N_{1,60}$) for Crystal Silica No. 20 sand, based on data from Seed and Silver (1972) and Silver and Seed (1971). Based on the work of researchers at UCLA (e.g., Whang 2001; Whang et al. 2004; Stewart et al. 2004a.b. Duku et al. 2008; Yee 2001; and Yee et al. 2014), Jiang et

al. (2020) "expanded" the Byrne (1991) model to be applicable to soils other than clean sand:

$$\left(\Delta\varepsilon_{v,1/2}\right)_i = 0.5 \cdot (\gamma_i - \gamma_{tv})^{C_3} \cdot C_1 \cdot exp\left[-C_2 \frac{\varepsilon_{vi}}{(\gamma_i - \gamma_{tv})^{C_3}}\right] \quad (3)$$

where C_1 and C_2 are the same material-specific parameters in the Byrne (1991) model and C_3 is an additional constant included by Jiang et al (2020) based on predicted versus observed soil response. The coefficients, C_1, C_2, and C_3 were calibrated for use with clean sands using data from Duku et al. (2008) and for non-plastic to moderately plastic silty sands/sandy silts using data from Yee et al. (2014). For the purposes of this case study, the Yee et al. (2014) equations were used because it was determined that most of the soil was silty sand with fines content (FC) ranging from 0-35%. These equations are:

$$C_1 = \frac{1}{F_p(\gamma)} \cdot K_{FC} \cdot K_S \cdot K_{\sigma,\varepsilon} \cdot a_{1\,atm\ \&\ FC=0\ \&\ S=0} \quad (4a)$$

$$F_p(\gamma) = 2.149 \cdot \gamma^{-0.2343} + 4.337 \cdot e^{-66.56 \cdot \gamma} \quad (4b)$$

$$K_{FC} = \frac{a_{FC}}{a_{FC=0}} = \begin{Bmatrix} 1 & if & 0 \le FC \le 10\% \\ e^{-0.042 \cdot (FC-10)} & if & 10\% < FC < \sim 35\% \\ 0.35 & if & FC > \sim 35\% \end{Bmatrix} \quad (4c)$$

$$K_S = \frac{a_S}{a_{S=0}} = \begin{Bmatrix} -0.017 \cdot S + 1 & if & S < 30\% \\ 0.5 & if & 30\% \le S < 50\% \\ 0.05 \cdot S - 2 & if & 50\% \le S < 60\% \\ 1 & if & S \ge 60\% \end{Bmatrix} \quad (4d)$$

$$K_{\sigma,\varepsilon} = \frac{a_\sigma}{a_{1\ atm}} = \left(\frac{\sigma_v'}{P_a}\right)^{-0.29} \quad (4e)$$

$$a_{1\,atm} = 5.38 \cdot e^{-0.023 \cdot Dr} \quad (4f)$$

$$Dr = 100 \cdot \sqrt{\frac{N_{1,60}}{C_d}} \quad (4g)$$

$$C_2 = \frac{P(\gamma)}{C_1} \quad (4h)$$

$$P(\gamma) = e^{0.405} \cdot (\gamma - \gamma_{tv})^{0.3291} \quad (4i)$$

$$C_3 = 1.2 \quad (4j)$$

where FC is in percent, S is degree of saturation in percent, σ'_v is the effective overburden pressure, P_a is atmospheric pressure, D_r is in percent, C_d is a soil-specific parameter determined by Skempton (1986) for relating $N_{1,60}$ and D_r, and γ and γ_{tv} are in percent. C_d values were determined by comparing the description of the soil from the boring logs to the data from Skempton (1986). These values are as follows: fine sand: 55, coarse sand: 65, cobbles of granite gneiss: 85, cobbles of quartzite: 100, and boulders of gneiss: 145. Fines content was estimated based on descriptions from the boring logs. The effective overburden pressure was calculated from the unit weights determined from the boring logs performed at the dam site.

The Expanded Byrne Model can also be used in a simplified form (Jiang et al. 2020):

$$\varepsilon_v = -ln\left(\prod_{i=1}^{2 \cdot n_{eqy}} t_i\right) \cdot \frac{(\gamma_{eff} - \gamma_{tv})^{C_3}}{C_n} \quad (5)$$

where

$$t_i = \begin{cases} e^{-0.5 \cdot C_1 \cdot C_2} & if\ i = 1 \\ (t_{i-1})^{t_{i-1}} & if\ i > 1 \end{cases} \quad (6)$$

The necessary parameters for using the simplified version are γ_{eff} and n_{eqy}. Correlations to determine $n_{eq\gamma}$ are typically a variant of the Palmgren-Miner fatigue theory such as those proposed by Seed et al. 1975 and Stafford and Bommer 2009 (Lasley et al. 2017), and γ_{eff} is solved for in a similar manner proposed in the threshold strain criterion proposed by Dobry et al. (1982)

Both the simplified and non-simplified variants of the Expanded Byrne Model are accumulative, meaning that the total volumetric strain is a function of the amplitude of the earthquake loading and is dependent upon previous loading increment. To this end, volumetric strain due to seismic compression is computed at the center of each soil layer in the soil profiles based on the loading. The volumetric strain is then multiplied by the thickness of the layer to determine the seismic compression of the layer due to earthquake loading. Finally, the seismic compression experienced by all soil layers is added together to find the settlement due to seismic compression of the whole soil profile.

Chapter 3: Application of the Expanded Byrne Model to the Tamakoshi Dam

3.1 Development of Soil Profiles for Analysis

To apply the Expanded Byrne Model, soil profiles were developed for analysis based on boring log data from the Tamakoshi Dam site. As stated previously, 27 unique soil types were identified in Boring Log 2 and 16 unique soil types in Boring Log 3. A noticeable difference between the two boring logs is the wider variety of soil in Boring Log 2, which included fine to coarse grained sand, clay, and gravel to cobbles of gneiss and other rock. Boring Log 3 consists mostly of similar layers of coarse-grained sand, clay, and gravel to boulders of gneiss. The location of these boreholes can be seen in Figure 2.2. Per Figure 2.2, Borehole 2 is closest to the flow path of the Tamakoshi River and therefore includes alluvial deposits, whereas Borehole 3 is closer to the abutment block and has layers designated as fine grained to course grained sand with fines and gravel. There is about 54 m laterally between the two boring locations. Ground water was encountered at 0.44 m in

Boring Log 2 and at 1.44 m in Boring Log 3, leading to the assumption that the profiles are mostly saturated.

Both boring logs showed very dense (measured SPT N values >50 blows/30cm) gravelly sand within the top 10 m of the profile. At deeper elevations, the measured SPT values varied between 10-60 blows/30cm with the higher SPT values typically being in clay or clayey material. Boring Log 3 generally showed higher SPT values than Boring Log 2. It should be noted that a limited amount of SPT data were available from the boring logs and, therefore, engineering judgment was used to extrapolate N-values for soil layers that did not have SPT data in modeling the soil profiles.

In total, 105 layers were used to model Soil Profile 2 and 129 were used for Soil Profile 3. Bedrock was hit at 121 m in Boring Log 2 but was not hit in Boring Log 3 because drilling stopped at 113.5 m. Therefore, layers in the Boring Log 3 soil profile from a depth of 113.5 m to 121.5 m were used to develop Soil Profile 2. The bedrock encountered was light gray banded gneiss that had several layers of weathered gravel and boulders of gneiss over it. As stated previously, groundwater was encountered at a depth of 0.44 m in Boring Log 2 and 1.44 m in Boring Log 3.

3.2 Liquefaction Evaluation

Seismic compression is generally considered to occur in unsaturated or partially saturated soil or in saturated soil where the excess pore water pressure is relatively low (Pyke 2019). Although there was no visual evidence of the occurrence of liquefaction at the site,

because of the shallow groundwater table at the dam site, it is possible that some of the layers under the dam liquefied. Thus, evaluating for liquefaction triggering and post-liquefaction consolidation in layers predicted to liquefy, rather than seismic compression is deemed appropriate. Liquefaction occurs when loose saturated sandy soil contracts under cyclic loading from earthquake shaking, resulting in the overburden stress being transferred from the soil matrix to the pore water as soil structure collapses, either rapidly or progressively. In such cases, the soil consolidates as the excess pore water pressures dissipate (Idriss and Boulanger 2008). The mechanics of seismic compression and post-liquefaction consolidation differ, and thus are evaluated using different models. While many of the sand layers in both profiles analyzed are dense (measured SPT values >30 blows/30 cm), there are enough that have lower SPT values (<20 blows/30 cm), and hence are considered as potentially liquefiable.

Both the volumetric threshold strain criterion proposed by Dobry et al. (1982) and the SPT-based Boulanger and Idriss (2014) simplified liquefaction procedure are used to evaluate the liquefaction potential of the profile. The Dobry et al. (1982) volumetric threshold strain criterion is applied to the two soil profiles developed from Boring Logs 2 and 3 to determine whether the induced strains were sufficient to potentially trigger liquefaction. The induced cyclic strain is estimated as (Dobry et al. 1982):

$$\gamma = \frac{0.65 \frac{a_{max}}{g} \sigma_v \cdot r_d}{G_{max}\left(\frac{G}{G_{max}}\right)_\gamma} \tag{7}$$

where a_{max} is the peak ground acceleration at the profile surface, g is acceleration due to gravity in the same units as a_{max}, σ_v is total overburden pressure at the specified depth, r_d is a phenomenological parameter that accounts for the non-rigid response of the soil

column, G_{max} is the small-strain shear modulus in the same units as σ_v, and G/G_{max} is the shear modulus ratio corresponding to the induced shear strain.

Per the USGS Shakemaps for the events, a_{max} was estimated to be ~0.24 g for the M_w7.3 May 12, 2015 aftershock and ~0.5g for the M_w7.8 April 25, 2015 main shock (USGS 2015). The total overburden pressure was computed based on estimated soil parameters from the boring logs, and r_d was calculated using the relationship given in Boulanger and Idriss (2014). G_{max} was calculated from the small-strain shear wave velocity (V_S) as:

$$G_{max} = V_s^2 \cdot \frac{\gamma_t}{g} \tag{8}$$

where γ_t is total unit weight of soil. The following relationship proposed by Ulmer et al. (2020) for liquefiable soils was used to estimate V_S:

$$V_s(^m/_S) = 60.01(N_{1,60cs})^{0.369}\left(\frac{\sigma'_{vo}}{P_a}\right)^{0.25} \tag{9}$$

Because G/G_{max} is a function of the induced shear strain, Eq. (7) is solved iteratively, as illustrated in Figure 3.1 for a fine sand layer from Soil Profile 2 (i.e., the soil profile model based on Boring Log 2). Two different shear modulus degradation curves were used in the analyses based on soil type. For sand, the Darendeli and Stokoe (2001) curves were used, and for gravels, the Rollins et al. (1998) curves, as modified by LoPresti et al. (2006), were used. Clay layers were not evaluated because they are not susceptible to liquefaction triggering. If the final computed shear strain was greater than the volumetric threshold shear strain, $\gamma > \gamma_{tv}$ where γ_{tv} = 0.01%, the layer was further evaluated using the Boulanger and Idriss (2014) simplified liquefaction triggering procedure. Based on the application of the Dobry et al. (1982) threshold strain criterion, 78 model layers in Soil Profile 2 and 109 model layers in Soil Profile 3 for the M_w7.8 April 25, 2015 main shock

had strain values greater than 0.01% and were thus further analyzed for liquefaction triggering. For the M_w7.3 May 12, 2015 aftershock, 73 model layers in Soil Profile 2 and 73 model layers in Soil Profile 3 had strain values greater than 0.01% and were also further analyzed for liquefaction triggering.

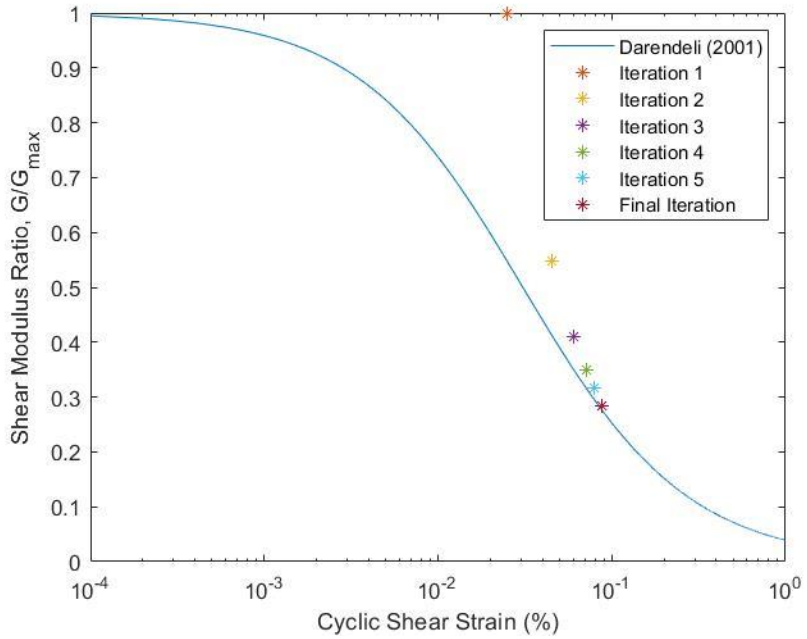

Figure 3.1 Application of Dobry et al. (1982) threshold strain criterion to a fine sand layer in the soil profile developed from Soil Profile 2.

The SPT-based Boulanger and Idriss (2014) simplified liquefaction procedure was used to evaluate whether liquefaction triggering is predicted to occur, where the factor of safety against liquefaction triggering (FS_{liq}) is defined as:

$$FS_{Liq} = \frac{CRR_{M7.5}}{CSR^*} \tag{10}$$

where CSR^* is the cyclic stress ratio normalized to 1 atm effective overburden stress, level ground, and an earthquake with M_w7.5, and $CRR_{M7.5}$ is the cyclic resistance ratio normalized for the same conditions as CSR^*. In this study, $CRR_{M7.5}$ is estimated from the normalized SPT blow count, $N_{1,60cs}$, per (Boulanger and Idriss 2014):

$$CRR_{M7.5} = exp\left\{\frac{N_{1,60cs}}{14.1} + \left(\frac{N_{1,60cs}}{126}\right)^2 - \left(\frac{N_{1,60cs}}{23.6}\right)^3 + \left(\frac{N_{1,60cs}}{25.4}\right)^4 - 28\right\} \leq 0.6 \qquad (11)$$

CSR^* is estimated as follows:

$$CSR^* = 0.65\frac{a_{max}}{g}\frac{\sigma_v}{\sigma'_{vo}}r_d\frac{1}{MSF}\frac{1}{K_\sigma \cdot K_\alpha} \qquad (12)$$

where MSF is the magnitude scaling factor and accounts for the influence of shaking duration on liquefaction trigger, K_σ is overburden correction factor, and K_α is the static shear stress correction factor determine using the procedures proposed in Boulanger and Idriss 2014.

The results of this evaluation predicted that 55 sandy model layers in Soil Profile 2 and 60 sandy model layers in Soil Profile 3 have $FS_{liq} < 1$ for the April 25, 2015 main shock, and 27 model layers in Soil Profile 2 and 28 layers in Soil Profile 3 have $FS_{liq} < 1$ for the May 12, 2015 aftershock. It should be noted that this is a smaller number of layers than that indicated by the application of the proposed threshold criterion by Dobry et al. (1982) These layers were primarily 20 m or deeper and thus it is likely that if liquefaction was triggered that it did not manifest at the ground surface (Iwasaki et al. 1978; Iwasaki et al. 1982). Additionally, as noted previously, preservation of liquefaction manifestation at the site was far less than optimal due to precipitation and river flow. As a result, if liquefaction did manifest at the ground surface, it is very possible that the features were washed away and not observed.

3.3 Selection of Appropriate Ground Motions

The non-simplified implementation of the Expanded Byrne Model for computing seismic compression requires shear strain time histories to be computed at varying depths within

the soil profile (e.g., depths corresponding to the center of each profile model layer). Towards this end, numerical site response analyses need to be performed; per Jiang et al. (2020), equivalent linear site response analyses can be used for this purpose. However, no strong motion recording stations were located on rock outcrops near the dam at the time of the earthquakes that are being analyzed in this study. As a result, the NGA West-2 ground motion prediction equations (GMPE) are used to estimate the input motions for numerical site response analyses for the M_w7.8, April 25, 2015 main shock and M_w7.3, May 12, 2015 aftershock. The use of these GMPEs is elaborated on in the Discussion section. Table 3.1 lists the parameters used in the GMPE to estimate the input motions. Figures 3.2 and 3.3 are the target spectra for the M_w7.8, April 25, 2015 main shock and M_w7.3, May 12, 2015 aftershock, respectively. Because there is uncertainty about the small-strain shear wave velocity (V_S) of the bedrock beneath the dam, spectra for both events were computed for V_S = 1000 m/s and 3000 m/s. The spectra for V_S = 1000 m/s were computed directly using the NGA West-2 Abrahamson et al. (2014), Campbell and Bozonrgnia (2014), and Chiou and Youngs (2014) GMPEs and scaling factors from Yenier and Atkinson (2015) were then used to modify these spectra for V_S = 3000 m/s.

Table 3.1 Parameters utilized in the NGA West-2 GMPEs for input motions. (e.g., Hashash et al. 2015, USGS 2015)

Parameter	Definition	Main Shock April 25, 2015	Aftershock May 12, 2015
M_w	Moment magnitude	7.8	7.3
R_{rup}	Closest distance to coseismic rupture (km)	34 km	30 km
R_{JB}	Closest distance to surface projection of coseismic rupture (km)	29 km	23 km
R_x	Horizontal distance from the top of the rupture measured perpendicular to fault strike (km)	81 km	39 km
R_{y0}	The horizontal distance off the end of the rupture measured parallel to strike (km)	0	0
V_{S30}	The average shear-wave velocity (m/sec) over a subsurface depth of 30m	1000 m/s	1000 m/s
F_{RV}	Reverse-faulting factor; 0 for strike slip, normal, normal-oblique; 1 for reverse, reverse-oblique	1	1
F_{NM}	Normal-faulting factor; 0 for strike slip, reverse, reverse-oblique, thrust and normal-oblique; 1 for normal	0	0
F_{HW}	Hanging-wall factor; 1 for site on down-dip side of top of rupture; 0 otherwise	1	1
Dip	Average dip of rupture plane (degrees)	11°	11°
Z_{TOR}	Depth to top of coseismic rupture (km)	15 km	15 km
Z_{HYP}	Hypocentral depth from the earthquake	15 km	15 km
$Z_{1.0}$	Depth to V_S = 1 km/sec (km)	0.005 km	0.005 km
$Z_{2.5}$	Depth to V_S = 2.5 km/sec (km)	1 km	1 km
W	Fault rupture width (km)	50 km	20 km

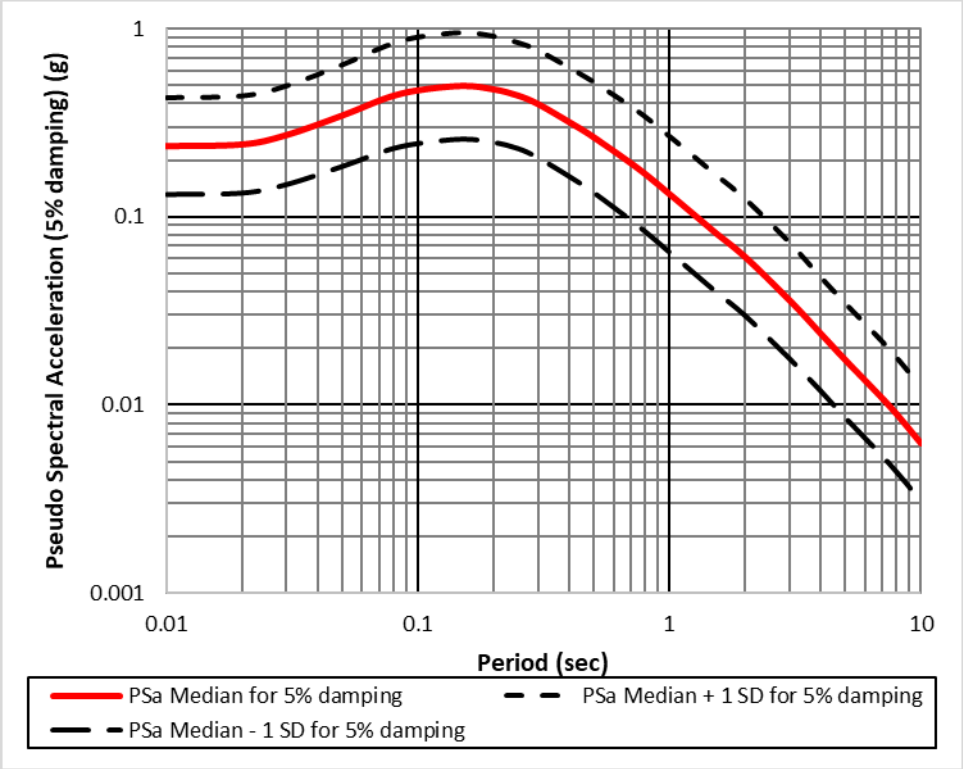

Figure 3.2 Target Spectra estimated from the NGA West-2 GMPE for the M_w7.8, April 25, 2015 main shock.

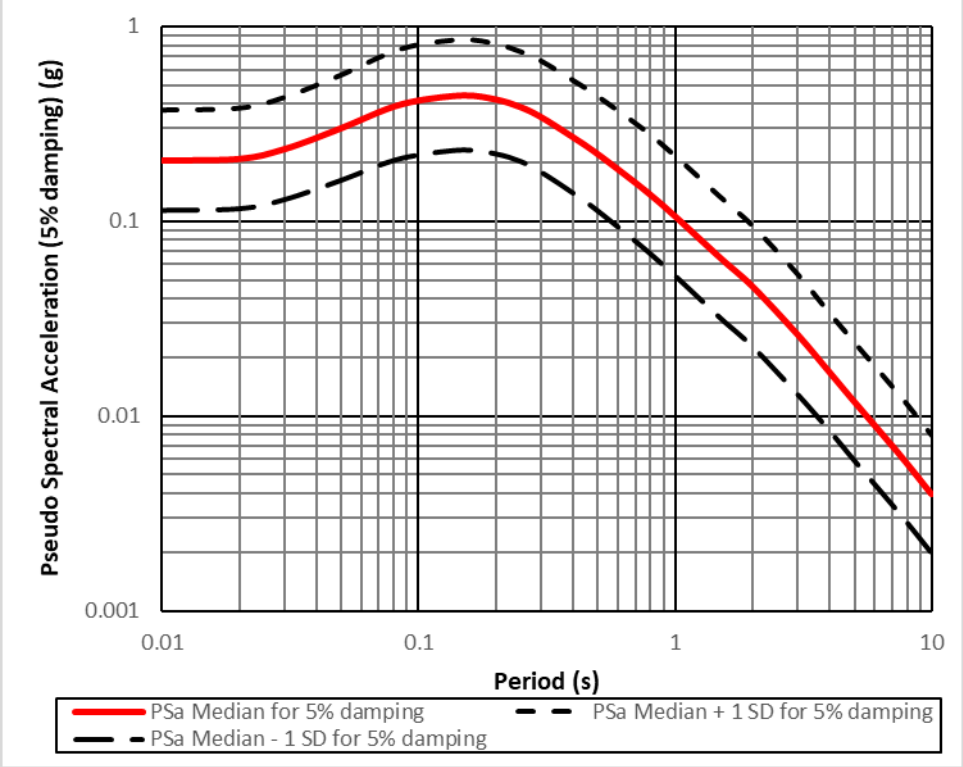

Figure 3.3 Target spectra estimated from the NGA West-2 GMPE for the M_w7.3, May 12, 2015 aftershock.

The spectra generated using the NGA West-2 GMPEs for the two events were used as target spectra in SigmaSpectra to select and scale suites of acceleration time histories to be used as input motions in the equivalent linear site response analyses. The acceleration time histories were selected from 124 motions from the PEER NGA West-2 ground motion database, where only motions having similar magnitudes and V_{S30} values were considered. The target spectrum for each event was separately loaded into SigmaSpectra and 5 sets of 15 representative ground motions were selected for each event. Figure 3.4 shows the target spectrum for the M_w7.8, April 25, 2015 main shock and the spectra for 1 set of 15 ground motions. Similar plots were created for all other sets of ground motions for the M_w7.8 April 25, 2015 main shock and M_w7.3 May 12, 2015 aftershock and are in Appendix A.

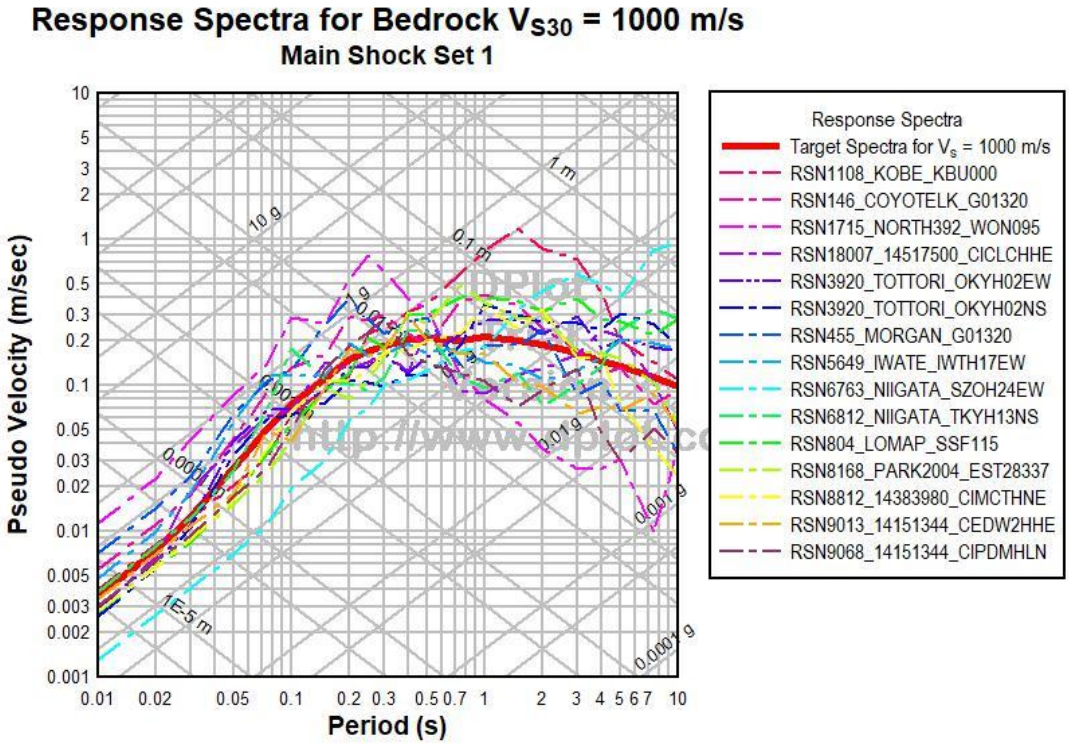

Figure 3.4 Scaled response spectra for selected ground motions for the M_w7.8, April 25, 2015 main shock with target spectra for a V_{S30} = 1000 m/s bedrock.

3.4 Shear Strain Time Histories – STRATA

As stated previously, equivalent linear site response analyses are used to compute shear strain time histories at varying depths within the soil profile as part of the non-simplified implementation of the Expanded Byrne Model for computing seismic compression. Towards this end, the same soil profiles used for the liquefaction triggering and threshold strain analyses are used in these numerical analyses.

Site response analyses were performed using each set of 15 ground motions and shear strain time histories at the center of each soil layer were computed. The shear strain time histories were used to compute seismic compression using the Expanded Byrne Model.

3.5 Computation of Settlement

Two approaches are used to compute settlement at the dam site. The first, as has been outlined, is via the implementation of the Expanded Byrne Model and assumes that the settlement experienced as a result of the earthquake is solely due to seismic compression. The second is a hybrid approach that assumes that the observed settlement is due to seismic compression in sandy layers that are not predicted to liquefy and post-liquefaction consolidation in the layers that are predicted to liquefy. In this hybrid approach the Expanded Byrne Model is used to compute the seismic compression and the Ishihara and Yoshimine (1992) model is used to compute post-liquefaction consolidation, implemented per Zhang et al. (2002).

In order to implement the Expanded Byrne Model, the shear strain time histories, corrected SPT N-value, fines content, effective confining stress, layer thickness, and soil specific parameter, C_d (Skempton 1986), are needed for all soil layers being analyzed. Clay layers are assumed to not be susceptible to seismic compression and are excluded from the analyses. The settlement for the entire profile is assumed to equal the sum of the settlements experienced by all the layers in the profile. A 1D-to-2D scaling factor is also included to account for the two-dimensional horizontal shaking during the earthquakes shown in Table 3.2 (Lasley and Green 2012; also see Nie et al. 2017). Additionally, a vertical-motion scaling factor per Pyke et al. (1975) is also applied to compute the final predicted value of seismic compression (e.g., Yee et al. 2011; Jiang et al. 2020). This vertical-motion scaling factor is used to account for the multi-directional shaking that occurs during earthquakes. Pyke et al. (1975) proposed that the effect of vertical motion on the sand, while thought to be negligible, did have some effect on the amount of compression a layer of sand would experience during earthquake shaking. This led to shake table tests that evaluated this effect and developed a relationship between the ratio of settlement with and without vertical motions and the equivalent vertical acceleration. It is this relationship that is used to determine the scaling factor for vertical motions.

Table 3.2 Correction Factor, C_{2D}, for Two-Dimensional Shaking (Lasley and Green 2012; also see Nie et al. 2017)

D_r (%) ($N_{1,60}$)	Moment Magnitude, M_w		
	5-6	6-7	7-8
45 (9)	1.5	1.6	1.7
60 (17)	1.9	1.8	1.8
80 (30)	2	1.9	1.8
100 (46)	2	2.1	2.1

The results from the analyses that assume settlement is solely due to seismic compression follow a log-normal distribution. Figure 3.5a and 3.5b show the results for all the sets for ground motions scaled to the V_{S30} = 1000 m/s bedrock spectra for Soil Profile 2 for the M_w7.8, April 25, 2015 main shock and M_w7.3, May 12, 2015 aftershock, respectively. Dashed-dot lines are superimposed on the plots and show the medians of the predicted settlements. Also, black dashed lines are superimposed on the graphs and denote the observed settlement in the field for each event. The standard deviation of the natural log of the predicted settlements are also noted on the graphs. Similar trends to these results are observed for input ground motions scaled to the V_{S30} = 3000 m/s bedrock spectra for Soil Profile 2, as well as for ground motions scaled to both V_{S30} = 1000 and 3000 m/s bedrock spectra for Soil Profile 3. These can be seen in Appendix B. Figure 3.6 shows how the settlements are distributed versus depth for a ground motion that predicted the median amount of settlement for the M_w7.8 April 25, 2015 main shock computed in Soil Profile 2 with bedrock V_{S30} = 1000 m/s. Similar plots were created for input ground motions scaled to the V_{S30} = 3000 m/s bedrock spectra for Soil Profile 2, as well as for ground motions scaled to both V_{S30} = 1000 and 3000 m/s bedrock spectra for Soil Profile 3. These can be seen in Appendix C.

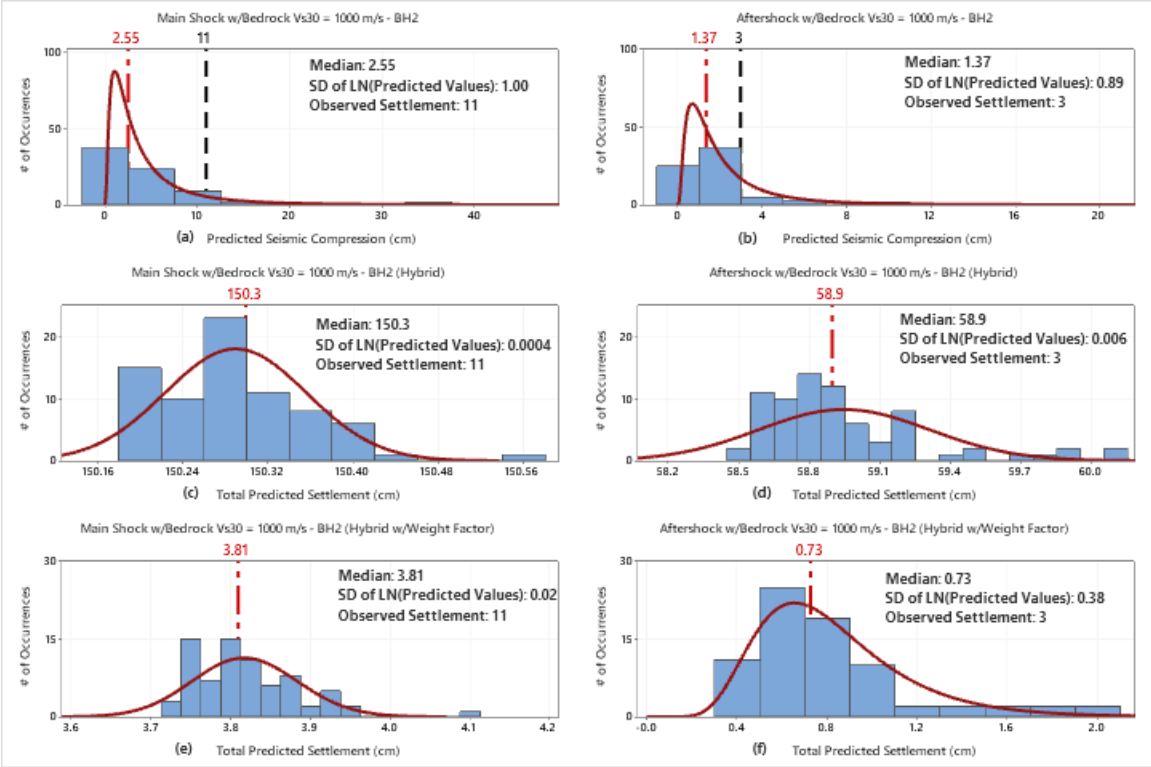

Figure 3.5 Results from Soil Profile 2 for bedrock V_{S30} = 1000 m/s: (a) settlements assuming strata only underwent seismic compression for the M_w7.8, April 25, 2015 main shock; (b) settlements assuming strata only underwent seismic compression for M_w7.3, May 12, 2015 aftershock; (c) settlements assuming strata underwent seismic compression and post-liquefaction consolidation for M_w7.8, April 25, 2015 main shock with no weight factor; (d) settlements assuming strata underwent seismic compression and post-liquefaction consolidation for M_w7.3, May 12, 2015 aftershock with no weight factor; (e) settlements assuming strata underwent seismic compression and post-liquefaction consolidation for M_w7.8, April 25, 2015 main shock with weight factor; and (f) settlements assuming strata underwent seismic compression and post-liquefaction consolidation for M_w7.3, May 12, 2015 aftershock with weight factor.

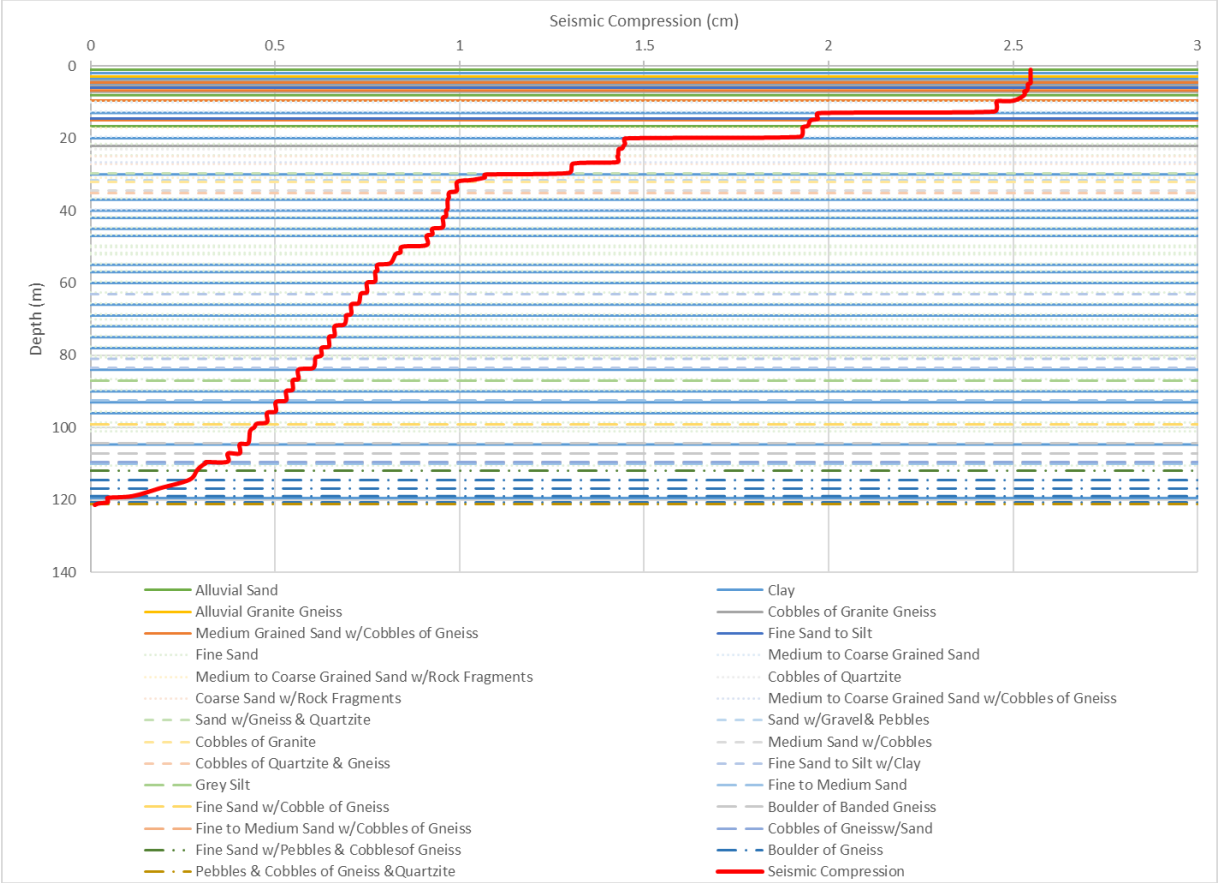

Figure 3.6 Predicted settlement for each layer in Soil Profile 2 for one representative ground motion scaled for the M_w7.8 April 25, 2015 main shock with bedrock V_{S30} = 1000 m/s assuming strata only underwent seismic compression.

For the hybrid analyses, settlements due to seismic compression are computed for sandy layers having a $FS_{liq} > 1$ and settlements due to post-liquefaction consolidation are computed for sandy layers having $FS_{liq} \leq 1$. For the seismic compression analyses, both the 1D-to-2D scaling factor and vertical-motion scaling factor are used in computing settlement. The results of the hybrid approach are also log-normally distributed. Figures 3.5c and 3.5d show the results for all sets of selected ground motions scaled to a V_{S30} = 1000 m/s bedrock spectrum for Soil Profile 2 for the main shock and aftershock, respectively. Figure 3.7 shows the distribution of settlement versus depth for a

representative ground motion for the M_w7.8 April 25, 2015 main shock computed in Soil Profile 2 with bedrock V_{S30} = 1000 m/s for this hybrid analysis.

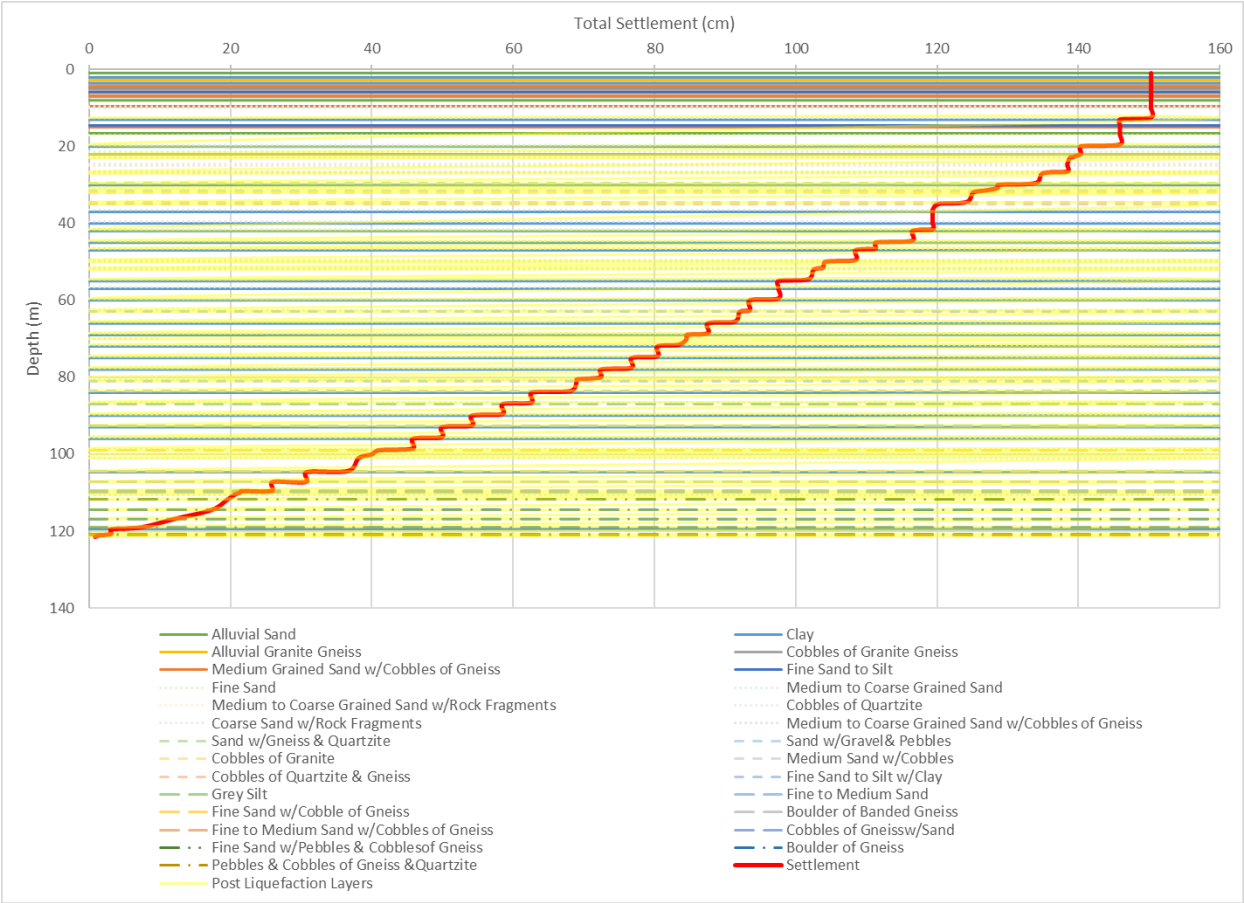

Figure 3.7 Predicted settlement for each layer in Soil Profile 2 for one representative ground motion scaled for the M_w7.8 April 25, 2015 main shock with bedrock V_{S30} = 1000 m/s assuming strata underwent seismic compression and post-liquefaction consolidation with no weight factor.

Due to the large, predicted settlement values from the hybrid analysis, a weighting factor from Cetin et al. (2009) that decreased with depth similar to that used by Iwasaki et al. (1982) for predicting the severity of surficial liquefaction manifestion was implemented. Utilizing this weighting factor, the effects of any liquefaction that occurred below 18 m

would not manifest at the surface and thus not contribute to surface settlement (Iwasaki et al. 1982). Figures 3.5e and 3.5f show the results for all sets of selected ground motions scaled to a V_{S30} = 1000 m/s bedrock spectrum for Soil Profile 2 for the main shock and aftershock with the weighting factor applied. As stated previously, the dashed-dot lines superimposed on the log-normal distributions are the medians of the predicted settlements. Also, the standard deviation of the natural log of the predicted settlements are noted on the log-normal graphs. Similar trends to these results are observed for input ground motions scaled to the V_{S30} = 3000 m/s bedrock spectra, for Soil Profile 2, as well as for ground motions scaled to both V_{S30} = 1000 and 3000 m/s bedrock spectra for Soil Profile 3. These can be seen in Appendix B. Figure 3.8 shows the distribution of settlement versus depth for a representative ground motion for the M_w7.8 April 25, 2015 main shock computed in Soil Profile 2 with bedrock V_{S30} = 1000 m/s for the hybrid analysis with the weight factor.

The median predicted settlements for Soil Profile 2 assuming solely seismic compression occurred are closer to the observed field settlements for all cases except the M_w7.8, April 25, 2015 main shock with input ground motions scaled to the V_{S30} = 3000 m/s bedrock spectra. The Soil Profile 2 median predicted settlements for the hybrid analysis are also closer to the observed field settlements except when no weight factor was applied for the M_w7.8 April 25, 2015 main shock. Soil Profile 3 median predicted values largely underpredicted the settlement values observed in the field. Tables 3.3 and 3.4 show a comparison of the median predicted values, standard deviation of the natural log of the predicted values and observed settlements for each event based on the bedrock V_{S30}.

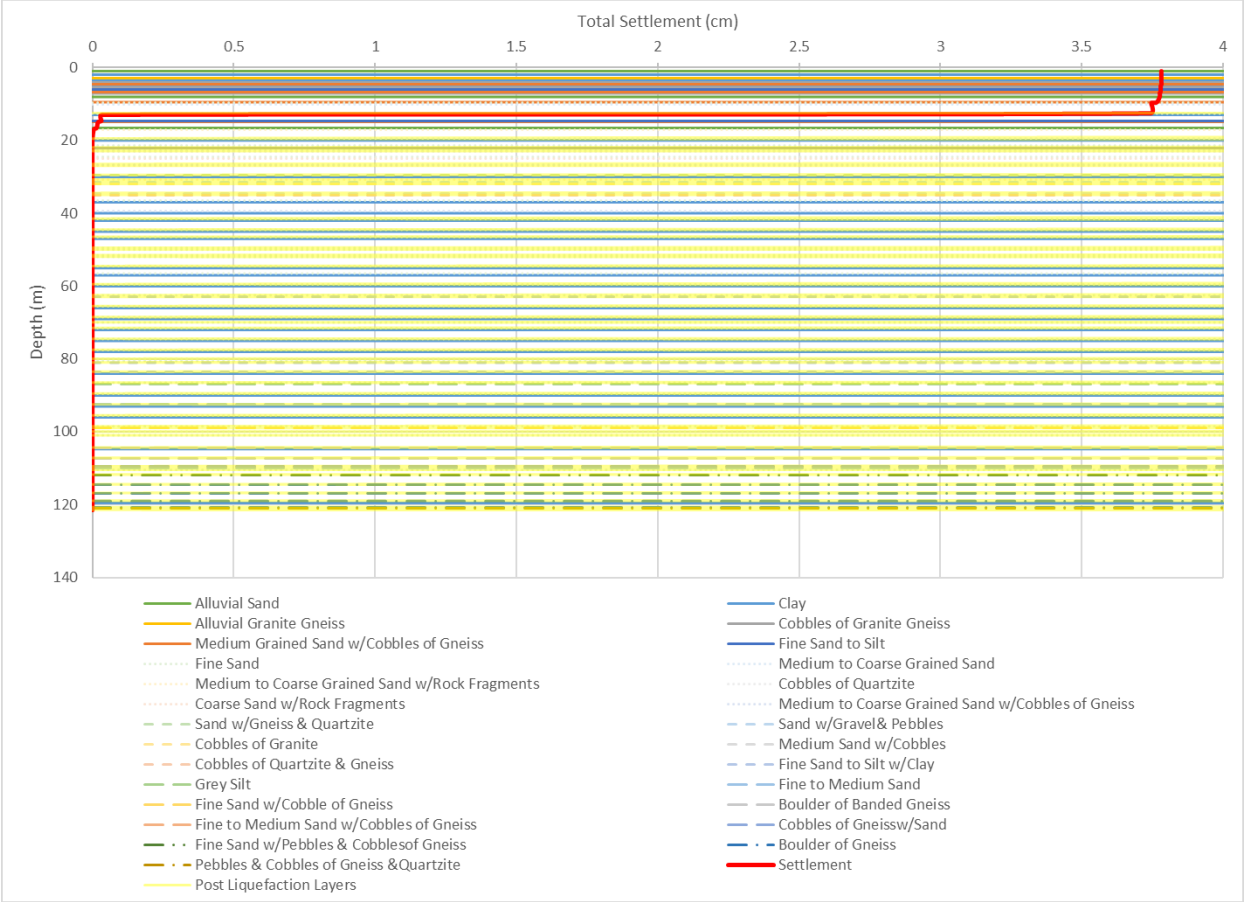

Figure 3.8 Predicted settlement for each layer in Soil Profile 2 for one representative ground motion scaled for the M_w7.8 April 25, 2015 main shock with bedrock V_{S30} = 1000 m/s assuming strata underwent seismic compression and post-liquefaction consolidation with weight factor.

Table 3.3 Comparison of median predicted settlement, standard deviation of the natural log of predicted values and observed settlement for both earthquakes and bedrock V_{S30} = 1000 m/s.

Soil Profile	Earthquake	Analysis Type	Median Predicted Settlement (cm)	SD of LN(Predicted Values)	Observed Settlement (cm)
Soil Profile 2	M_w7.8 April 25, 2015 Main shock	Seismic Compression Only	2.55	1	11
Soil Profile 3	M_w7.8 April 25, 2015 Main shock	Seismic Compression Only	2	0.95	11
Soil Profile 2	M_w7.8 April 25, 2015 Main shock	Hybrid with no weight factor	150.3	0.0004	11
Soil Profile 3	M_w7.8 April 25, 2015 Main shock	Hybrid with no weight factor	134.6	0.0005	11
Soil Profile 2	M_w7.8 April 25, 2015 Main shock	Hybrid with weight factor	3.81	0.02	11
Soil Profile 3	M_w7.8 April 25, 2015 Main shock	Hybrid with weight factor	1.32	0.04	11
Soil Profile 2	M_w7.3 May 12, 2015 aftershock	Seismic Compression Only	1.37	0.89	3
Soil Profile 3	M_w7.3 May 12, 2015 aftershock	Seismic Compression Only	1.21	0.9	3
Soil Profile 2	M_w7.3 May 12, 2015 aftershock	Hybrid with no weight factor	58.9	0.006	3
Soil Profile 3	M_w7.3 May 12, 2015 aftershock	Hybrid with no weight factor	61.3	0.02	3
Soil Profile 2	M_w7.3 May 12, 2015 aftershock	Hybrid with weight factor	0.73	0.38	3
Soil Profile 3	M_w7.3 May 12, 2015 aftershock	Hybrid with weight factor	0.41	0.88	3

Table 3.4 Comparison of median predicted settlement, standard deviation of the natural log of predicted values and observed settlement for both earthquakes and bedrock V_{S30} = 3000 m/s.

Soil Profile	Earthquake	Analysis Type	Median Predicted Settlement (cm)	SD of LN(Predicted Values)	Observed Settlement (cm)
Soil Profile 2	M_w7.8 April 25, 2015 Main shock	Seismic Compression Only	2.32	1.2	11
Soil Profile 3	M_w7.8 April 25, 2015 Main shock	Seismic Compression Only	3.23	1	11
Soil Profile 2	M_w7.8 April 25, 2015 Main shock	Hybrid with no weight factor	150.3	0.001	11
Soil Profile 3	M_w7.8 April 25, 2015 Main shock	Hybrid with no weight factor	134.6	0.0008	11
Soil Profile 2	M_w7.8 April 25, 2015 Main shock	Hybrid with weight factor	3.83	0.03	11
Soil Profile 3	M_w7.8 April 25, 2015 Main shock	Hybrid with weight factor	1.35	0.07	11
Soil Profile 2	M_w7.3 May 12, 2015 aftershock	Seismic Compression Only	1.87	1.1	3
Soil Profile 3	M_w7.3 May 12, 2015 aftershock	Seismic Compression Only	1.28	0.93	3
Soil Profile 2	M_w7.3 May 12, 2015 aftershock	Hybrid with no weight factor	59.2	0.01	3
Soil Profile 3	M_w7.3 May 12, 2015 aftershock	Hybrid with no weight factor	61.3	0.02	3
Soil Profile 2	M_w7.3 May 12, 2015 aftershock	Hybrid with weight factor	1.03	0.49	3
Soil Profile 3	M_w7.3 May 12, 2015 aftershock	Hybrid with weight factor	0.46	0.9	3

The predicted settlements for both approaches (i.e., assuming that settlements are due solely to seismic compression and due to both seismic compression and post-liquefaction consolidation) mostly under-predict the observed field values except the hybrid approach with no weight factor applied. Reasons for this general under-prediction are explored in the Discussion.

Chapter 4: Discussion

As noted previously, the predicted settlements for the Expanded Byrne Model and hybrid approach with weight factor included generally under-predict the observed field values. However, the hybrid approach without the weighting factor included significantly over-predicts the observed field settlements. Given the low computed FS_{liq} for the strata in the dam profile for both events analyzed, it is very likely that liquefaction was indeed triggered during these events. As a result, the settlements observed at the site were likely due to both seismic compression and post-liquefaction consolidation. One potential for the significantly over- and under-predicted settlements for the hybrid analyses with and without the depth weighting factor applied, respectively, is that the weighting factor used is not appropriate for the site being analyzed.

Cetin et al. (2009) state that the rationale for the need for the depth weighting factor is: *"(1) upward seepage, triggering void ratio redistribution, and resulting in unfavorably higher void ratios for the shallower sublayers of soil layers; (2) reduced induced shear stresses and number of shear stress cycles transmitted to deeper soil layers due to initial liquefaction of surficial layers; and (3) possible arching effects due to non-liquefied soil layers."* Cetin et al. (2009) used a similar form for their proposed depth weighting factor as the one proposed by Iwasaki et al. (1982) for predicting the severity of surficial liquefaction manifestations. While all of the factors listed by Cetin et al. (2009) likely played a role in the settlements that manifested at the ground surface at the dam site, the extreme mountainous terrain at the site somewhat implies that the surface topography at

the site is much more complex than the sites included in the Iwasaki et al. (1982) and Cetin et al. (2009) studies.

The complex subsurface topography, namely the narrow, deep V-shaped valley with very steep side walls, at the Tamakoshi Dam would likely influence factors (2) and (3) differently from the sites analyzed by Iwasaki et al. (1982) and Cetin et al. (2009). Specifically, lateral variation in the soil strata would lessen the effect of induced shear stresses and number of shear stress cycles transmitted to deeper soil layers being reduced due to initial liquefaction of surficial layers. This effect would be most pronounced in profiles where the soil strata were uniformly laterally and less pronounced in laterally varying profiles. On the contrary, lateral variation in soil strata might enhance arching effects due to non-liquefied soil layers. However, it is very unlikely that these two trends would perfectly offset each other such that the depth weighting factor proposed by Cetin et al. (2009) would be as applicable to the Tamakoshi Dam profile as the sites included in the Iwasaki et al. (1982) and Cetin et al. (2009) studies. In this regard, if the depth weighting factor extended to a deeper critical depth than assumed by Cetin et al. (2009) then the predicted settlements for the hybrid analyses would increase. However, more detailed analyses would be required to determine the critical depth for this site.

Another likely reason for the general under-predictions in settlement for the hybrid analyses with the depth weighting factor is due to the bias in the selected and scaled ground motions. As detailed previously, the NGA-West 2 GMPEs were used to predict the bedrock ground motions at the dam site for the two earthquakes. However, given that

there are no recorded motions in the proximity of the dam site, the reasonableness of the predicted motions is highly uncertain. There are two aspects of this, the first relates to the appropriateness of using the NGA-West 2 GMPEs for the tectonic setting and the second relates to the influence of topographic effects on the ground motions, which would be captured by the NGA- West 2 GMPEs. Regarding the tectonic setting, the NGA-West 2 GMPEs were developed for the Western United States which has a drastically different tectonic setting than experienced in Nepal. As stated previously, Nepal sits on both the Indian and Eurasian tectonic plates and the Indian plate is currently converging under the Eurasian plate. This is the dominating tectonic feature of this area and thus characterizes the seismicity in the area. In contrast, the Western United States tectonic setting is not dominated by convergence, but a combination of convergence, and mostly divergent tectonic activity. Thus, the use of the NGA-West 2 GMPEs most likely did not accurately capture the tectonic setting that is in Nepal and could be a reason why the predicted settlements did not reflect what was observed in the field. Additionally, due to the complex topography at the Tamakoshi Dam, it is unlikely that the NGA-West 2 GMPEs would be able to characterize the ground motions experienced there.

Finally, another potential reason for the under-prediction of settlement for the hybrid analysis with the depth weighting factor is the uncertainty in the soil profiles that were analyzed. Inherently, the development of the soil profiles entailed significant engineering judgment to assign unit weights and fines contents to all strata and to interpolate SPT N-values for layers that did not have field measurements. There is some uncertainty in selecting these values and therefore there could be potential bias in the developed soil

profiles that could lead to errors in the predicted settlements. However, this is not thought to be a major contributor to the under-predictions, or not as significant as a contributor as the issues discussed above.

Chapter 5: Summary and Conclusions

The settlements experienced by the Tamakoshi Dam were evaluated using two approaches: one assuming the settlements were solely due to seismic compression and the second assuming that the settlements were due to a combination of seismic compression and post-liquefaction consolidation (i.e., hybrid mechanisms). In both approaches, the non-simplified Expanded Byrne Model was used to predict settlement due to seismic compression, while the Ishihara and Yoshimine (1992) model, implemented per Zhang et al. (2002), was used to compute post-liquefaction consolidation for the hybrid analysis. The settlement analyses were performed on two soil profiles developed from boring logs performed at the Tamakoshi dam site.

The acceleration time histories used in the equivalent linear site response analyses to compute seismic compression were selected and scaled to bedrock target spectra for the events for V_{S30} = 1000 and 3000 m/s generated using the NGA West-2 ground motion prediction equations (GMPEs). In total 124 motions were compiled from the PEER NGA West-2 database based on their associated M_w and V_{S30}, relative to those of the events being evaluated. However, the software used to select and scale the motions., SigmaSpectra, only selected a small subset of these motions for use in the site response analyses, implying that most of the motions did not have spectral shapes in accord with

the target spectra. Also, the appropriateness of the selected motions is somewhat questionable because of the applicability of the NGA-West 2 GMPEs to the tectonic setting of Nepal.

Both 1D-to-2D scaling factors and vertical-motion scaling factors were used in computing seismic compression. For the post-liquefaction consolidation analyses, the factors of safety against liquefaction triggering (FS_{liq}) were assessed using the Boulanger and Idriss (2014) SPT-based simplified model. For the hybrid analyses, settlements due to seismic compression were computed for sandy layers having a $FS_{liq} > 1$ and settlements due to post-liquefaction consolidation were computed for sandy layers having $FS_{liq} \leq 1$. Soil Profile 2 generally had predicted settlements that were closer to the observed field settlements.

The settlements for both earthquakes were generally under-predicted for both approaches, indicating that the observed settlements in the field were likely due to both seismic compression and post-liquefaction consolidation. The likely reasons for the under-predictions are that the weighting factor by Cetin et al. (2009) did not account for the complex topography at the Tamakoshi Dam, and the NGA-West 2 GMPEs do not accurately account for the tectonic setting in Nepal. The accuracy of the NGA-West 2 GMPEs being most noticeable in the selected scaled ground motions used to compute shear strain time histories for use in the Expanded Byrne model.

One recommendation for future work would be to utilize different ground motion prediction equations that represent the tectonic setting of Nepal more accurately, and to research recorded strong ground motions from Nepal for utilization in the GMPEs. This could potentially include developing a source model for earthquakes in the area. Another recommendation would be to better characterize the topography of the Tamakoshi Dam including using two dimensional analysis versus a one dimensional analysis as conducted here. Since it is believed that the complex topography at the Tamakoshi Dam influenced the ground motions experienced during the Gorkha earthquake sequence, and the response of the compressible and liquefiable strata, this would be a key starting point.

5.1 Overview of Appendices

Multiple Appendices are included to show the information used and computed in the completion of this case study. Appendix A is the response spectra for each set of 15 scaled ground motions for each earthquake and bedrock shear wave velocity. Appendix B is the predicted settlement distribution plots. Appendix C has the plots of predicted settlement versus depth selected for one representative ground motion per soil profile and earthquake for both analysis methods. Appendix D is peak shear strain plots from STRATA that were used to help determine the peak shear strain experienced in each soil layer per ground motion and soil profile. Appendix E is the MATLAB code and input parameters used to compute seismic compression.

References

Abrahamson, N. A., W. J. Silva, and R. Kamai (2014). Summary of the ASK14 ground motion relation for active crustal regions, *Earthquake Spectra*, Vol 30, No. 3, pp 1025–1055, August 2014.

Bollinger, L., Henry, P., and Avouac, J. P. (2006). "Mountain building in the Nepal Himalaya: Thermal and kinematic model." *Earth and Planetary Science Letters*, 244, 58–71.

Boore, D. M., Stewart, J. P., Seyhan, E., and Atkinson G.M. (2014). "NGA-West2 Equations for Predicting PGA, PGV and 5% Damped PSA for Shallow Crustal Earthquakes." *Earthquake Spectra*, 30(3).

Boulanger, R. W., and Idriss, I. M. (2014). *CPT and SPT Based Liquefaction Triggering Procedures*. Report No. UCD/CGM-14/01, Center for Geotechnical Modeling, UC Davis, Davis, CA, 1–138.

Byrne, P. (1991). A cyclic shear-volume coupling and pore pressure model for sand, Proc.,*2nd Int. Conf. on Recent Advances in Geotechnical Earthquake Engineering and Soil Dynamics,* Missouri Univ. of Science and Technology, Rolla, MO, 47–55.

Campbell, K. W. and Y. Bozorgnia (2014). NGA-West2 ground motion model for the average horizontal components of PGA, PGV, and 5% damped linear acceleration response spectra, *Earthquake Spectra*, Vol 30, No. 3, pp 1087–1115.

Cetin, K. O., Bilge, T., Wu, J., Kammerer, A. M., and Seed, R. B. (2009). "Probabilistic Model for the Assessment of Cyclically Induced Reconsolidation (Volumetric) Settlements." *Journal of Geotechnical and Geoenvironmental Engineering*, 135(3), 387–398.

Chiou, B. S. J. and R. R. Youngs (2014). Update of the Chiou and Youngs NGA model for the average horizontal component of peak ground motion and response spectra, *Earthquake Spectra*, Vol 30, No. 3, pp 1117–1153.

Darendeli, M. B., and Stokoe, K. H. (2001). "Development of a New Family of Normalized Modulus Reduction and Material Damping Curves." PhD Thesis, The University of Texas at Austin, Austin, Texas.

DeCelles, P. G., Robinson, D. M., Quade, J., Ojha, T. P., Garzione, C. N., Copeland, P., and Upreti, B. N. (2001). "Stratigraphy, structure, and tectonic evolution of the Himalayan fold-thrust belt in western Nepal." *Tectonics*, 20(4), 487–509.

Dobry, R., Ladd, R. S., Yokel, F. Y., Chang, R. M., and Powell, D. (1982). *Prediction of Pore Water Pressure Buildup and Liquefaction of Sands During Earthquakes by the Cyclic Strain Method*. *Prediction of Pore Water Pressure Buildup and Liquefaction of Sands During Earthquakes by the Cyclic Strain Method*, U.S. Department of Commerce, Washington D.C., 1–180.

Duku, P. M., Stewart, J. P., Whang, D. H., and Yee, E. (2008). "Volumetric strains of clean sands subject to cyclic loads." *Journal of Geotechnical and Geoenvironmental Engineering*, 134(8), 1073–1085.

Green, R. A., and Terri, G. A. (2005). "Number of equivalent cycles concept for liquefaction evaluations - Revisited." *Journal of Geotechnical and Geoenvironmental Engineering*, 131(4), 477–488.

Hashash, Y.M.A., Tiwari, B., Moss, R.E.S., Asimaki, D., Clahan, K.B., Kieffer, D.S., Dreger, D.S., Macdonald, A., Madugo, C.M., Mason, H.B., Pehlivan, M., Rayamajhi, D., Acharya, I., Adhikari, B. (2015). "Geotechnical field reconnaissance: Gorkha (Nepal) earthquake of April 25, 2015, and related shaking sequence," *NSF Geotechnical Association Report*, GEER 0-40.

Idriss, I. M. (2014). "An NGA-West2 Empirical Model for Estimating the Horizontal Spectral Values Generated by Shallow Crustal Earthquakes." *Earthquake Spectra*, 30(3).

Idriss, I. M., and Boulanger, R. W. (2008). Soil liquefaction during earthquakes. Monograph MNO-12, Earthquake Engineering Research Institute, Oakland, CA.

Ishihara, K., and Yoshimine, M. (1992). "Evaluation of settlements in sand deposits following liquefaction during earthquakes." *Soils and Foundations*, 32(1), 173–188.

Iwasaki, T., Tatsuoka, F., Tokida, K., and Yasuda, S. (1978). "A Practical Method for Assessing Soil Liquefaction Potential Based on Case Studies at Various sites in Japan." 5th Japan Earthquake Engineering Symposium. Vol II: 641-648.

Iwasaki, T., Tokida, K., Tatusoka, F., Watanabe, S., Yasuda, S., and Sato, H. (1982). "Microzonation for soil liquefaction potential using simplified methods." Proceedings 3rd International Conference on Microzonation, Seattle, WA. 1319-1330.

Jiang, Y., Green, R. A., and Taylor, O.-D. (2020). "Expanded Byrne Model for Evaluating Seismic Compression." *Earthquake Spectra*, in review.

Karan, P. P. (2021). *Nepal*. *Britannica*, Encyclopedia Britannica Inc.

Lasley, S. and Green, R.A. (2012). *Evaluating seismic compression and post liquefaction settlement at level-ground sites.* CGPR Report #69. Blacksburg, VA: Center for Geotechnical Practice and Research (CGPR), The Charles E. Via, Jr., Department of Civil and Environmental Engineering, Virginia Tech.

Lasley, S., Green, R. A., and Rodriguez-Marek, A. (2017). "Number of Equivalent Stress Cycles for Liquefaction Evaluations in Active Tectonic and Stable Continental Regimes." *Journal of Geotechnical and Geoenvironmental Engineering*, 143(4).

Lo Presti, D., Pallara, O., and Mensi, E. (2006). "Soil Stress-Strain Behavior: Measurement, Modeling and Analysis Geotechnical Symposium." *Characterization of Soil Deposits for Seismic Response Analysis*, Rome, 1–49.

Martin, G. R., Finn, W. D. L., and Seed, H. B. (1975). "Fundamentals of liquefaction under cyclic loading." J. Geotech Eng. Div., 101(5), 423–438.

Moss, R. E. S., Thompson, E. M., Kieffer, D. S., Tiwari, B., Hashash, Y. M. A., Acharya, I., Adhikari, B. R., Asimaki, D., Clahan, K. B., Collins, B. D., Dahal, S., Jobson, R. W., Khadka, D., Macdonald, A., Madugo, C. L. M., Mason, B., Pehlivan, M., Rayamajhi, D., and Uprety, S. (2015). "Geotechnical Effects of the 2015 Magnitude 7.8 Gorkha, Nepal, Earthquake and Aftershocks." *Seismological Research Letters*, 86(6), 1514–1523.

Nie, C.-X., Chen, Q.-S., Gao, G.-Y., and Yang, J. (2017). "Determination of seismic compression of sand subjected to two horizontal components of earthquake ground motions." *Soil Dynamics and Earthquake Engineering*, 92, 330–333.

"NGA West 2." (2021). *NGA West 2 | Pacific Earthquake Engineering Research Center*, University of California - Berkeley, https://peer.berkeley.edu/research/nga-west-2 (Last accessed Jan. 23, 2021).

Pyke, R., Chan, C. K., and Seed, H. B. (1974). *Settlement and Liquefaction of Sands Under Multi Directional Shaking*, rep., University of California, Berkeley, California, 1–88.

Pyke, R. (2019). "Improved analyses of earthquake induced liquefaction and settlement." In: Proceedings of the 7th International Conference on Earthquake Geotechnical Engineering (7ICEGE), Rome, 17-20 June.

Rollins, K. M., Evans, M. D., Diehl, N. B., and Iii, W. D. D. (1998). "Shear Modulus and Damping Relationships for Gravels." *Journal of Geotechnical and Geoenvironmental Engineering*, 124(5), 396–405.

Seeber, L. (1981). "Great Detachment Earthquakes Along the Himalayan Arc and Long-Term Forecasting." *Earthquake Prediction: An International Review*, J. G. Armbruster, ed., essay, American Geophysical Union, 259–277.

Seed, H. B., and Silver, M. L. (1972). "Settlement of dry sands during earthquakes." *Journal of the Soil Mechanics and Foundation Division*, 98(4), 381–397.

Silver, M. L., and Seed, H. B. (1971). "Volume changes in sands during cyclic loading." *Journal of the Soil Mechanics and Foundations Division*, 97(9), 1171–1182.

Seed, H. B., Idriss, I. M., Makdisi, F., and Banerjee, N. (1975). *Representation of irregular stress time histories by equivalent uniform stress series in liquefaction analyses*, rep., EERC 75-29, Earthquake Engineering Center, University of California, Berkeley, CA.

Skempton, A. W. (1986). "Standard penetration test procedures and the effects in sands of overburden pressure, relative density, particle size, ageing and overconsolidation." *Géotechnique*, 36(3), 425–447.

Stafford, P. J., and Bommer, J. J. (2009). "Empirical equations for the prediction of the equivalent number of cycles of earthquake ground motion." *Soil Dynamics and Earthquake Engineering*, 29(11), 1425–1436.

Stewart, J. P., Smith, P. M., Whang, D. H., and Bray, J. D. (2004a). "Seismic compression of two compacted earth fills shaken by the 1994 Northridge earthquake." *Journal of Geotechnical and Geoenvironmental Engineering*, 130(5), 461–476.

Stewart, J. P., Whang, D. H., Moyneur, M., and Duku, P. (2004b). *Seismic Compression of as-Compacted Fill Soils with Variable Levels of Fines Content and Fines Plasticity*, rep., Consortium of Universities for Research in Earthquake Engineering, Richmond, CA.

Tiwari, B., Ajmera, B., and Timbadia, V. (2019). "Case Study-Settlement of a Hydropower Dam Structure during 2015 Gorkha Earthquake." Geo-Congress 2019. Philadelphia PA, 24-27 March.

Tokimatsu, K., and Seed, H. B. (1987). "Evaluation of Settlements in Sands Due to Earthquake Shaking." *Journal of Geotechnical Engineering*, 113(8), 861–878.

Ulmer, K., Green, R. A., and Rodriguez-Marek, A. (2020). "A Consistent Correlation between Vs, SPT, and CPT Metrics for Use in Liquefaction Evaluation Procedures," Geo-Congress 2020. Minneapolis MN, 25-28 February.

Upper Tamakoshi Hydropower Limited (2020). http://utkhpl.org.np/project-introduction/ (last accessed October 23, 2020).

U.S. Geological Survey (2015). Significant Event Webpage for the April 25, 2015 M7.8 – 36km E of Khudi, Nepal earthquake. https://earthquake.usgs.gov/earthquakes/eventpage/us20002926/executive

U.S. Geological Survey (2015). Significant Event Webpage for the May 12, 2015 M7.3 – 19km SE of Kodari, Nepal earthquake. https://earthquake.usgs.gov/earthquakes/eventpage/us20002ejl/executive

Vucetic, M., and Dobry, R. (1991). "Effect of Soil Plasticity on Cyclic Response." *Journal of Geotechnical Engineering*, 117(1), 89–107.

Whang, D. (2001). “Seismic Compression of compacted fills.” PhD Thesis, Civil and Environmental Engineering Department, University of California at Los Angeles, Los Angeles, CA.

Whang, D. H., Stewart, J. P., and Bray, J. D. (2004). “Effect of compaction conditions on the seismic compression of compacted fill soils.” *Geotechnical Testing Journal*, 27(4), 371–379.

Yee, E. (2011). “Investigation of nonlinear site response and seismic compression from case history analysis and laboratory testing.” PhD Thesis, Civil and Environmental Engineering Department, University of California at Los Angeles, Los Angeles, CA.

Yee, E., Stewart, J. P., and Tokimatsu, K. (2011). *Nonlinear site response and seismic compression at vertical array strongly shaken by 2007 Nigata-ken Chuetsu-oki earthquake*, Report No. 2011/107. Berkeley, CA: Pacific Earthquake Engineering Research Center, University of California.

Yee, E., Duku, P. M., and Stewart, J. P. (2014). “Cyclic volumetric strain behavior of sands with fines of low plasticity.” *Journal of Geotechnical and Geoenvironmental Engineering*, 140(4).

Yenier, E., and G. M. Atkinson (2015a). Regionally-adjustable generic ground-motion prediction equation based on equivalent point-source simulations: Application to central and eastern North America, chapter 4, in *NGA-East: Median Ground- Motion Models for the Central and Eastern North America Region, PEER Report Number 2015/04*, University of California, Berkeley, California, 85–118.

Zhang, G., Robertson, P. K., and Brachman, R. W. I. (2002). “Estimating liquefaction-induced ground settlements from CPT for level ground.” *Canadian Geotechnical Journal*, 39(5), 1168–1180.

APPENDIX A: Response Spectra

The scaled response spectra for the M_w7.8 April 25, 2015 main shock with V_{S30} = 1000 and 3000 m/s and M_w7.3 May 12, 2015 aftershock with V_{S30} = 1000 and 3000 m/s are presented in Appendix A.

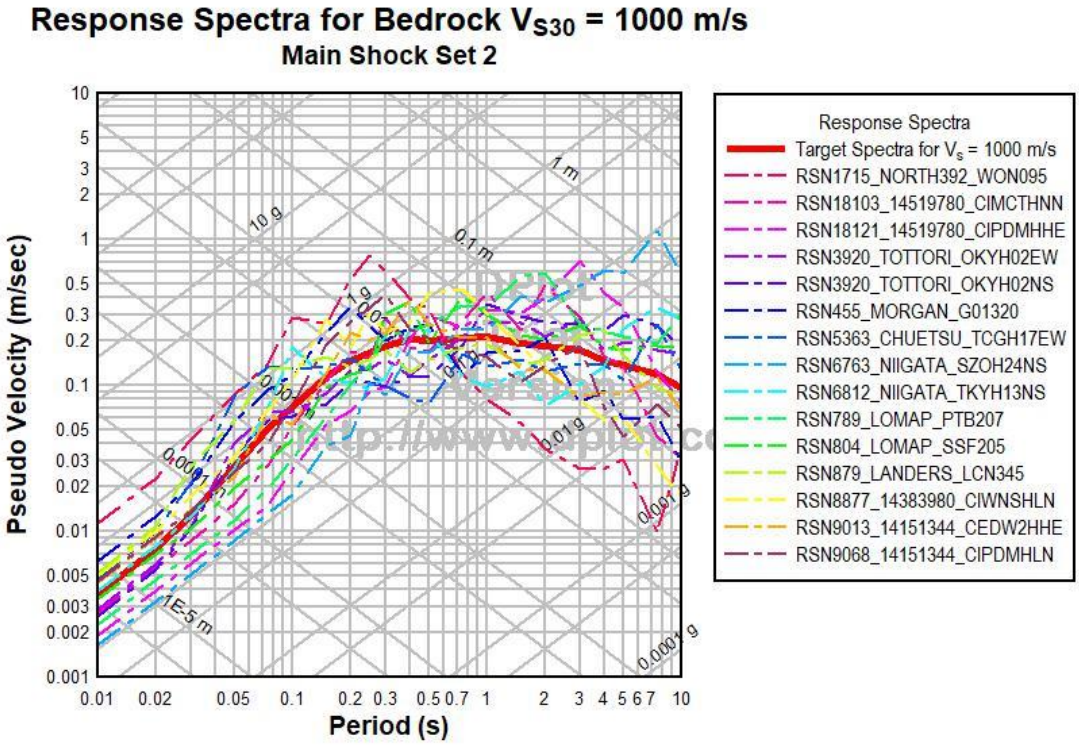

Figure A.1 Scaled response spectra for selected ground motions for the M_w7.8 April 25, 2015 main shock with target spectra for a V_{S30} = 1000 m/s bedrock, Set 2.

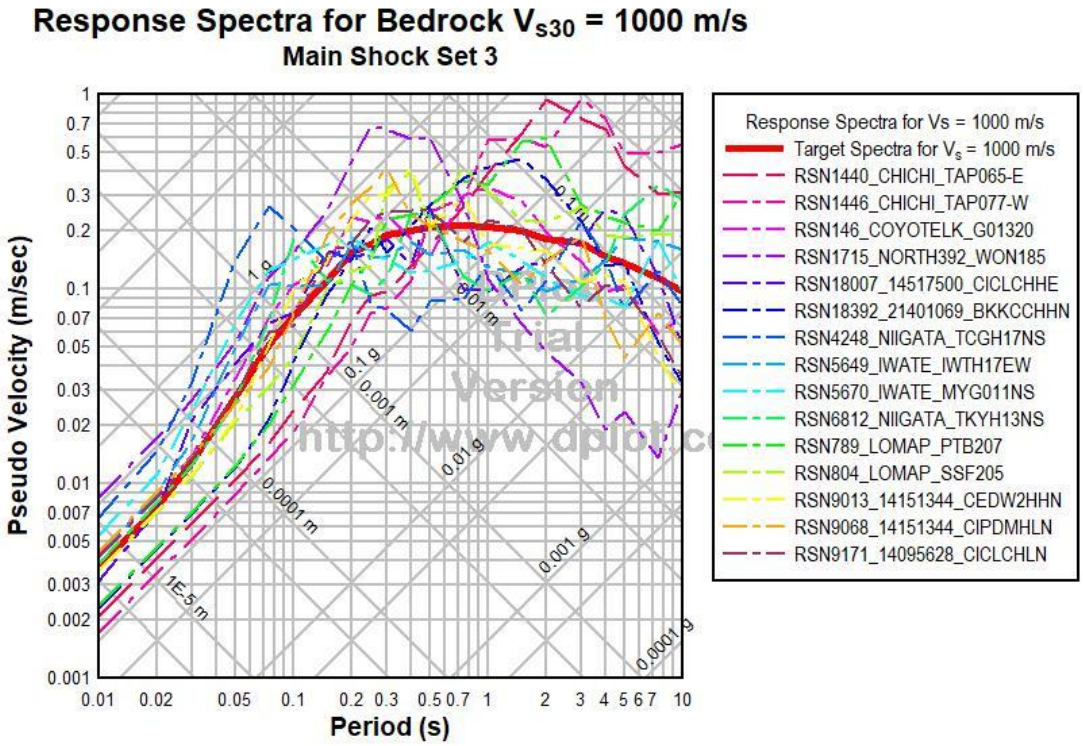

Figure A.2 Scaled response spectra for selected ground motions for the M_w7.8 April 25, 2015 main shock with target spectra for a V_{S30} = 1000 m/s bedrock, Set 3.

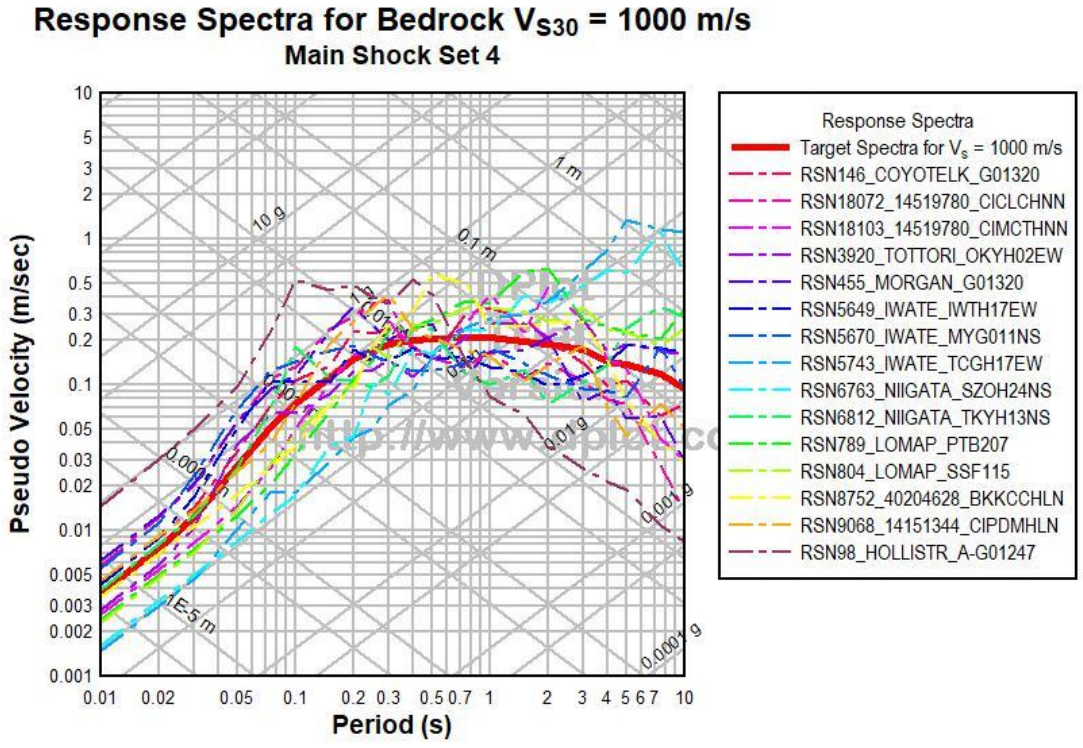

Figure A.3 Scaled response spectra for selected ground motions for the M_w7.8 April 25, 2015 main shock with target spectra for a V_{S30} = 1000 m/s bedrock, Set 4.

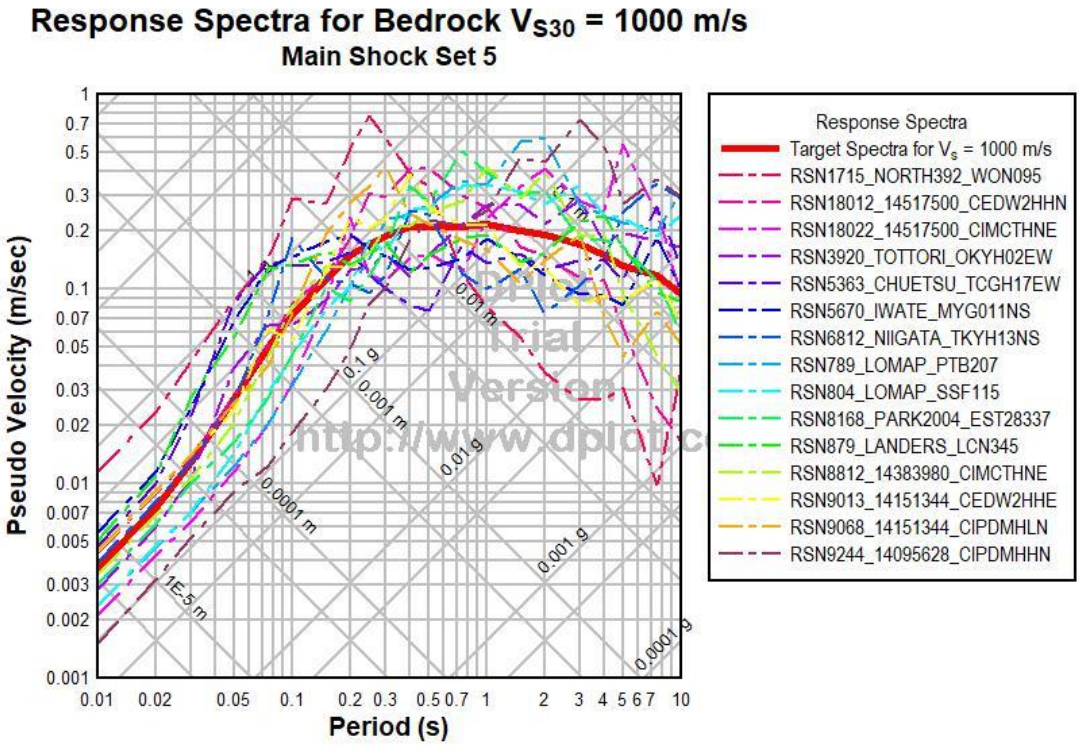

Figure A.4 Scaled response spectra for selected ground motions for the M_w7.8 April 25, 2015 main shock with target spectra for a V_{S30} = 1000 m/s bedrock, Set 5.

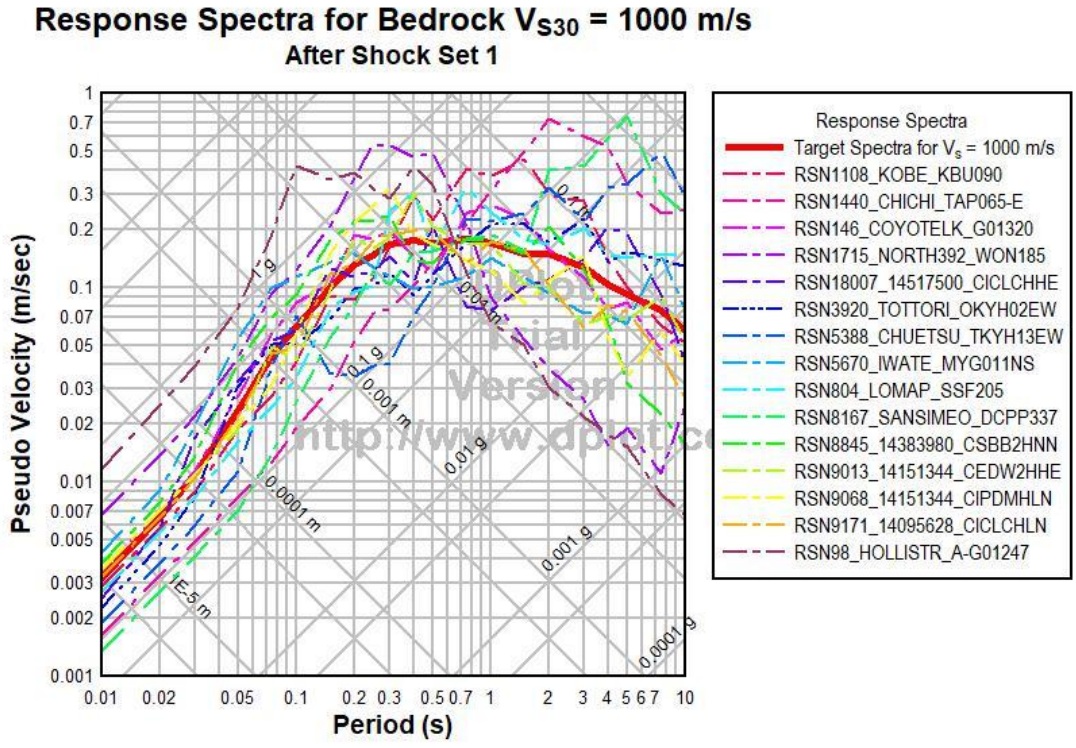

Figure A.5 Scaled response spectra for selected ground motions for the M_w7.3 May 12, 2015 aftershock with target spectra for a V_{S30} = 1000 m/s bedrock, Set 1.

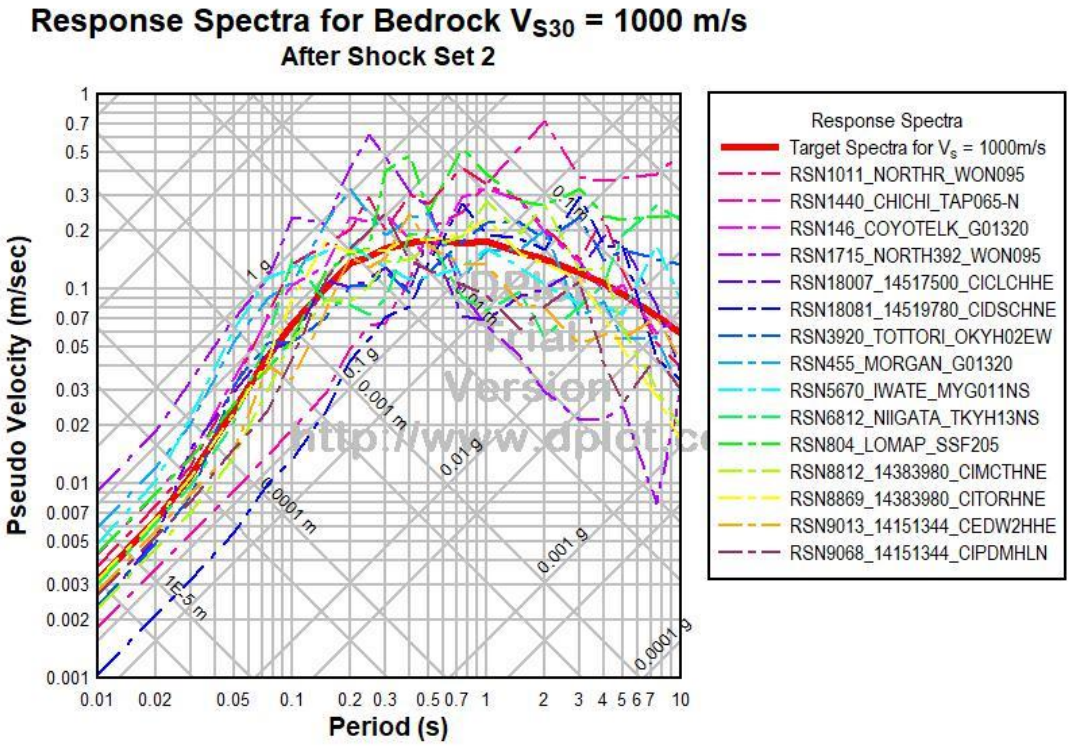

Figure A.6 Scaled response spectra for selected ground motions for the M_w7.3 May 12, 2015 aftershock with target spectra for a V_{S30} = 1000 m/s bedrock, Set 2.

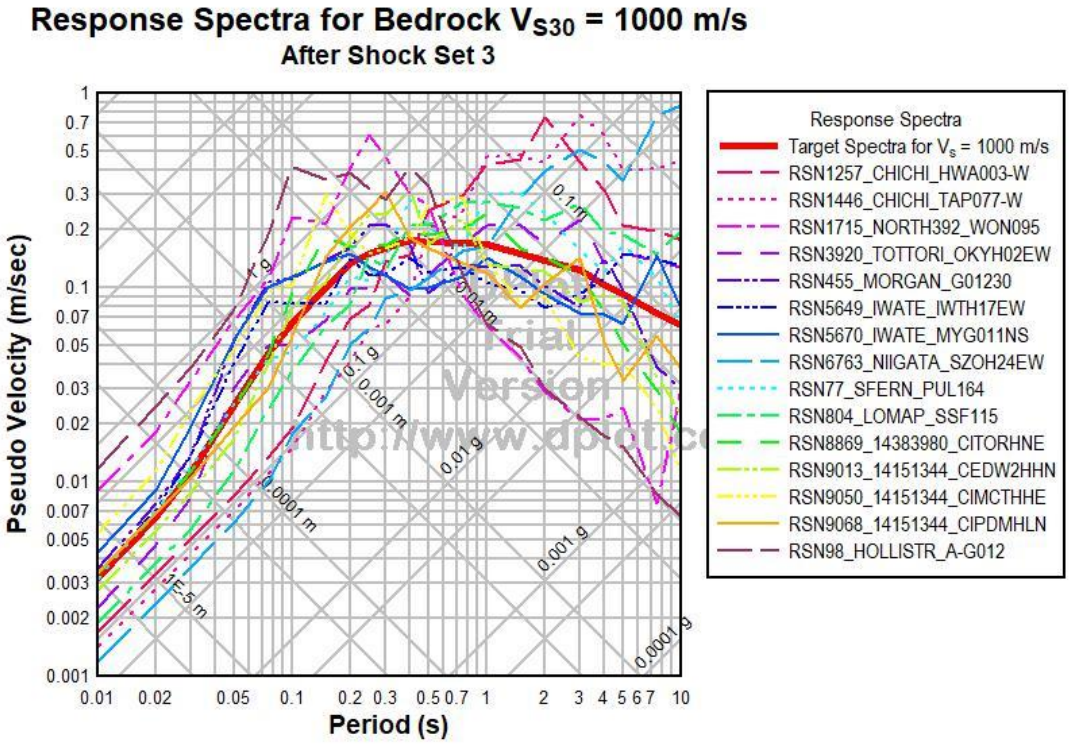

Figure A.7 Scaled response spectra for selected ground motions for the M_w7.3 May 12, 2015 aftershock with target spectra for a V_{S30} = 1000 m/s bedrock, Set 3.

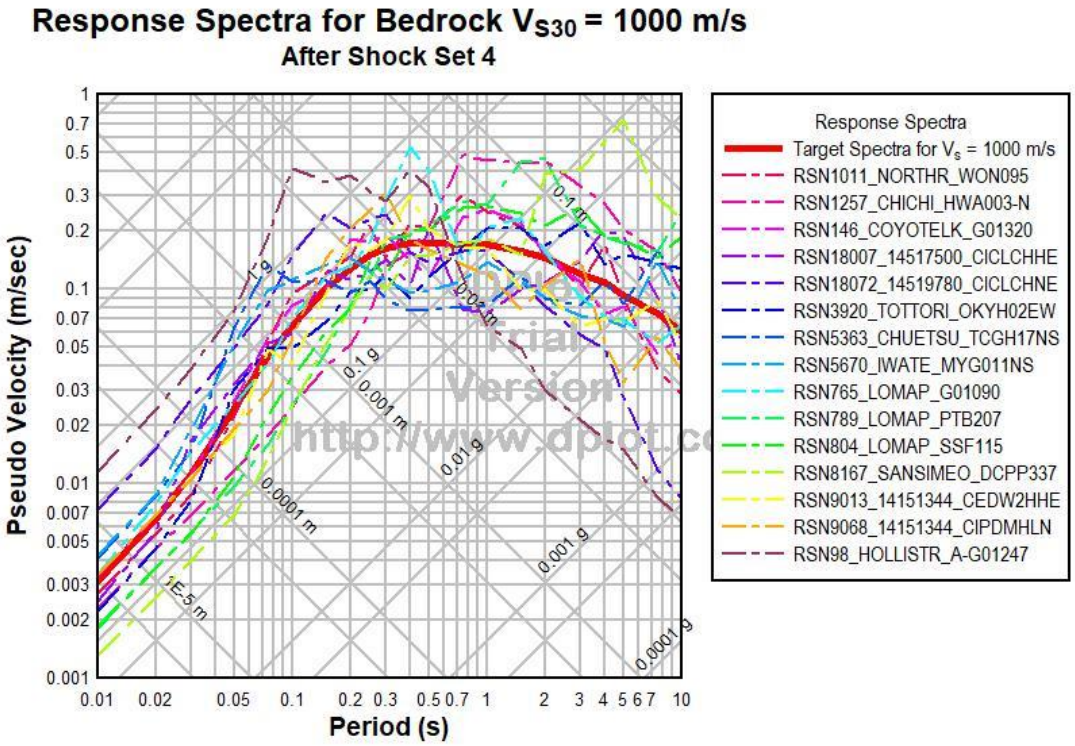

Figure A.8 Scaled response spectra for selected ground motions for the M_w7.3 May 12, 2015 aftershock with target spectra for a V_{S30} = 1000 m/s bedrock, Set 4.

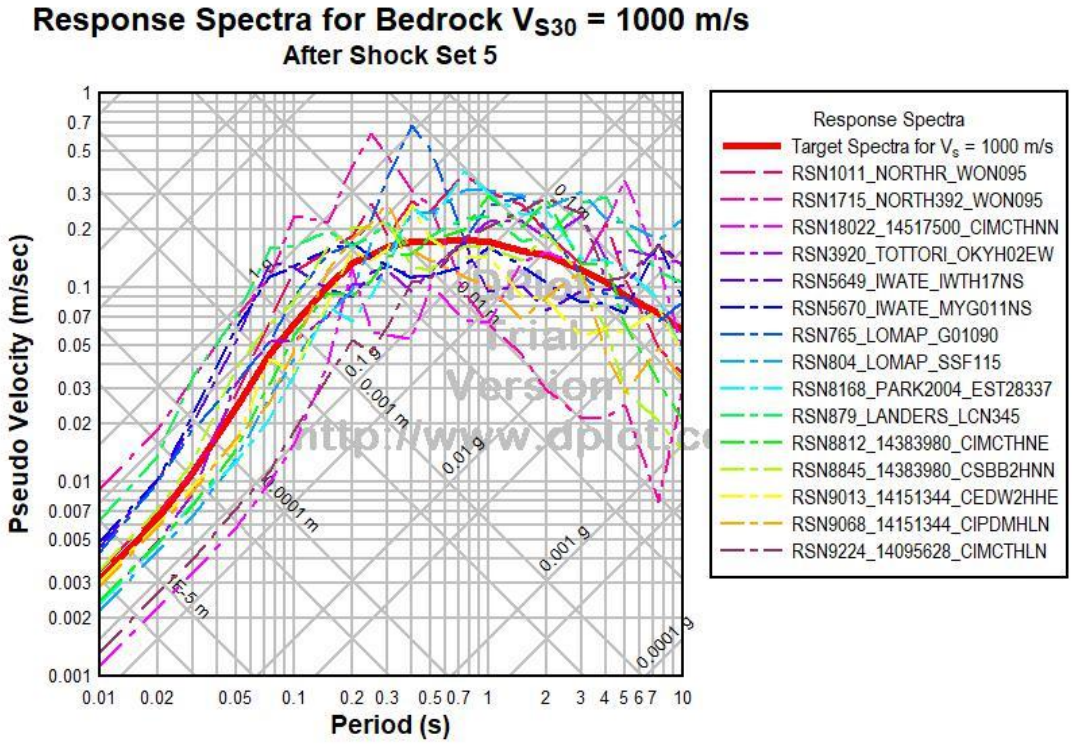

Figure A.9 Scaled response spectra for selected ground motions for the M_w7.3 May 12, 2015 aftershock with target spectra for a V_{S30} = 1000 m/s bedrock, Set 5.

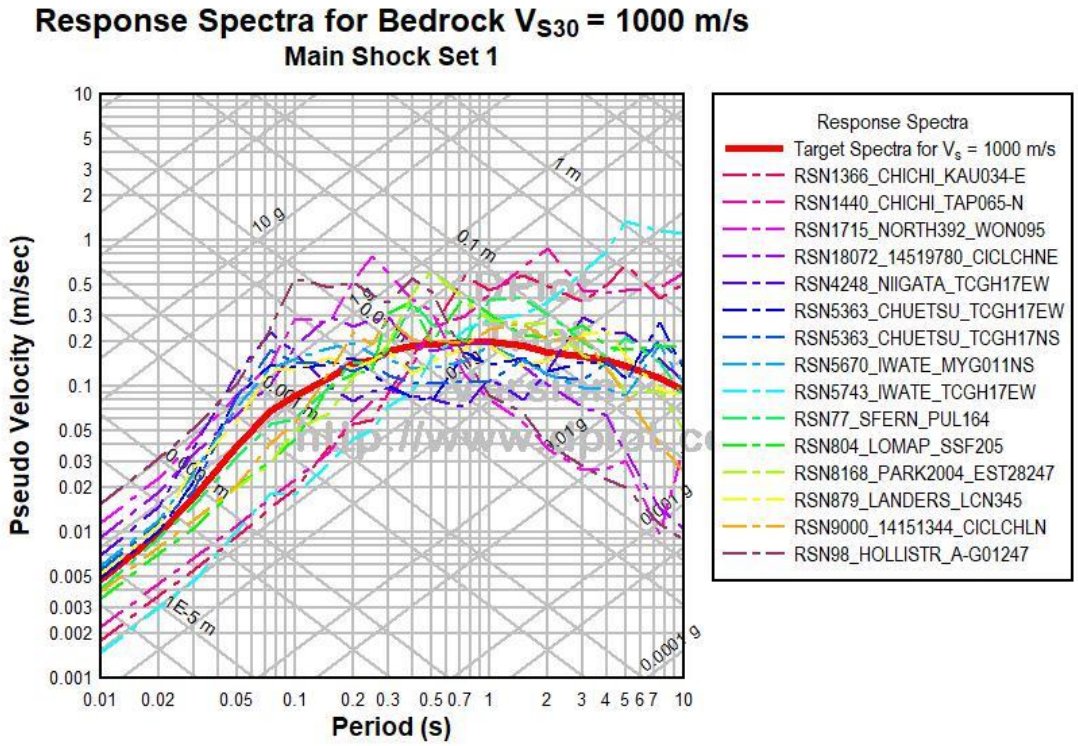

Figure A.10 Scaled response spectra for selected ground motions for the M_w7.8 April 25, 2015 main shock with target spectra for a V_{S30} = 3000 m/s bedrock, Set 1.

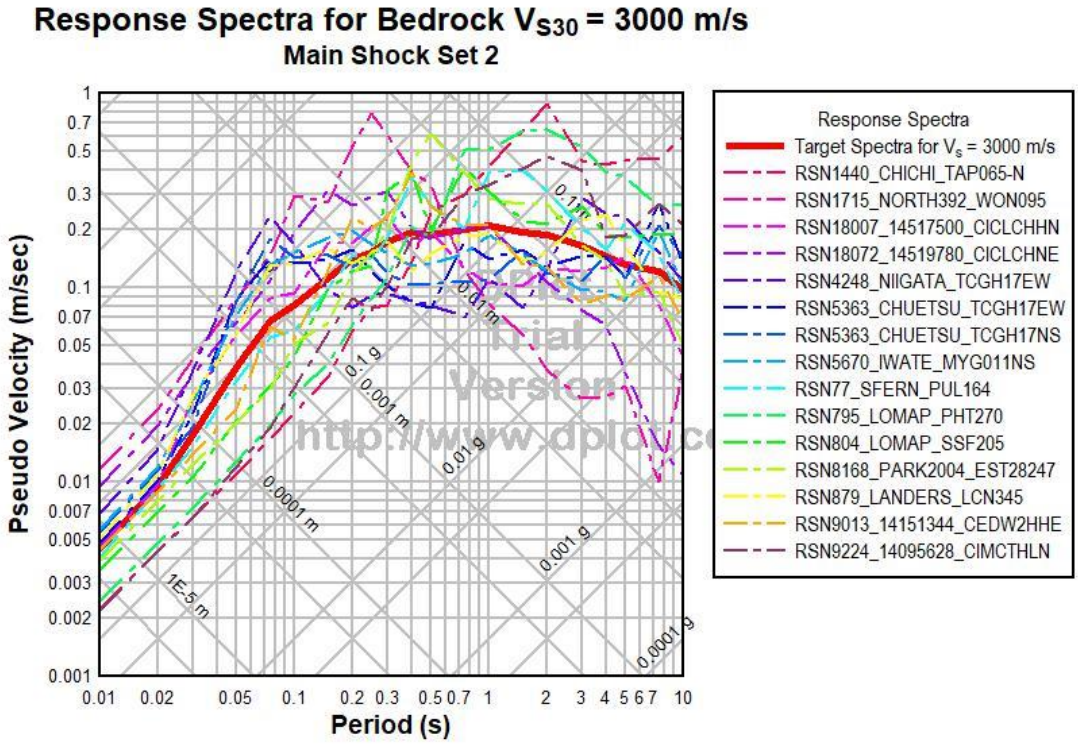

Figure A.11 Scaled response spectra for selected ground motions for the M_w7.8 April 25, 2015 main shock with target spectra for a V_{S30} = 3000 m/s bedrock, Set 2.

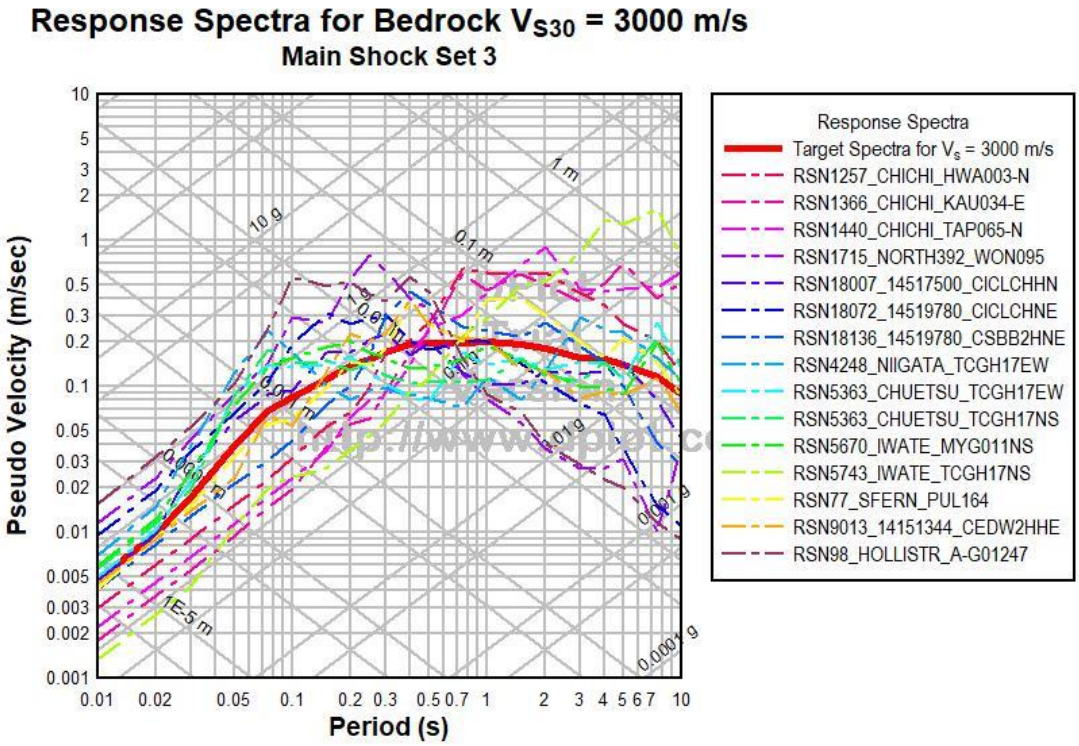

Figure A.12 Scaled response spectra for selected ground motions for the M_w7.8 April 25, 2015 main shock with target spectra for a V_{S30} = 3000 m/s bedrock, Set 3.

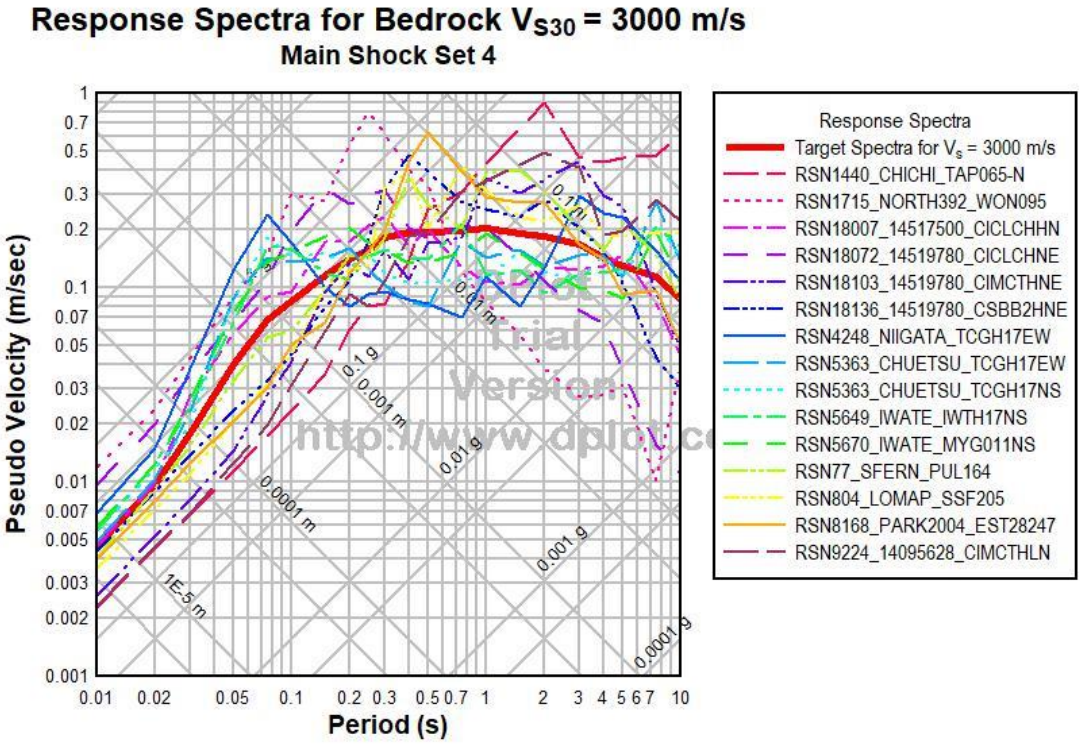

Figure A.13 Scaled response spectra for selected ground motions for the M_w7.8 April 25, 2015 main shock with target spectra for a V_{S30} = 3000 m/s bedrock, Set 4.

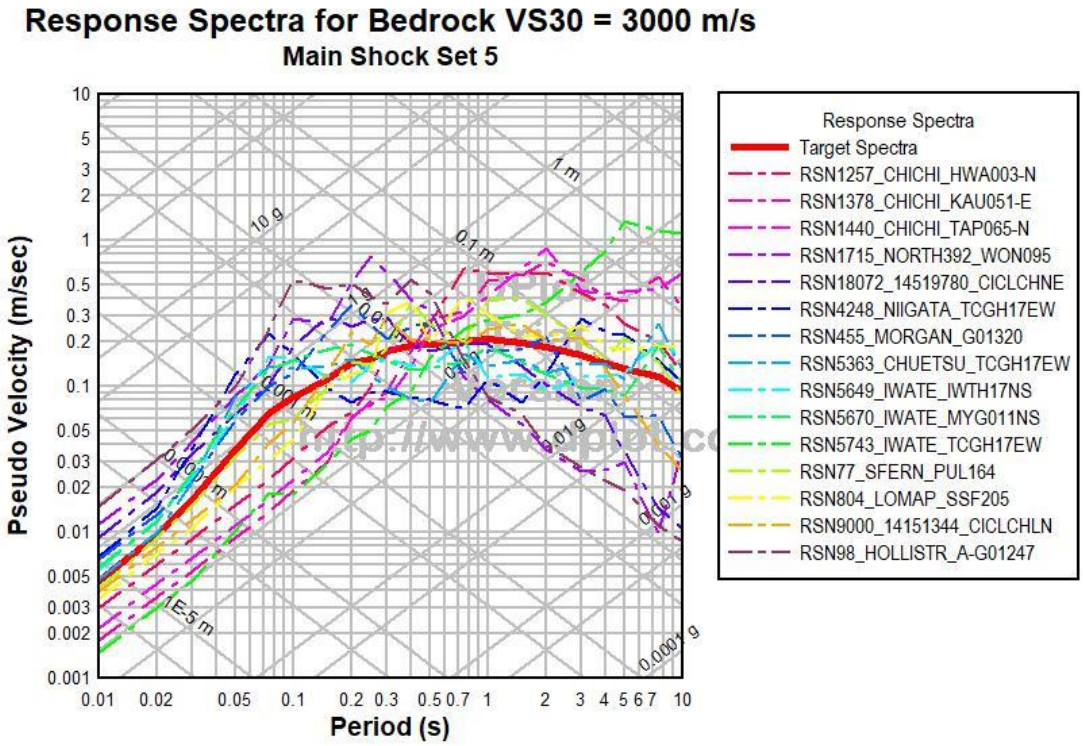

Figure A.14 Scaled response spectra for selected ground motions for the M_w7.8 April 25, 2015 main shock with target spectra for a V_{S30} = 3000 m/s bedrock, Set 5.

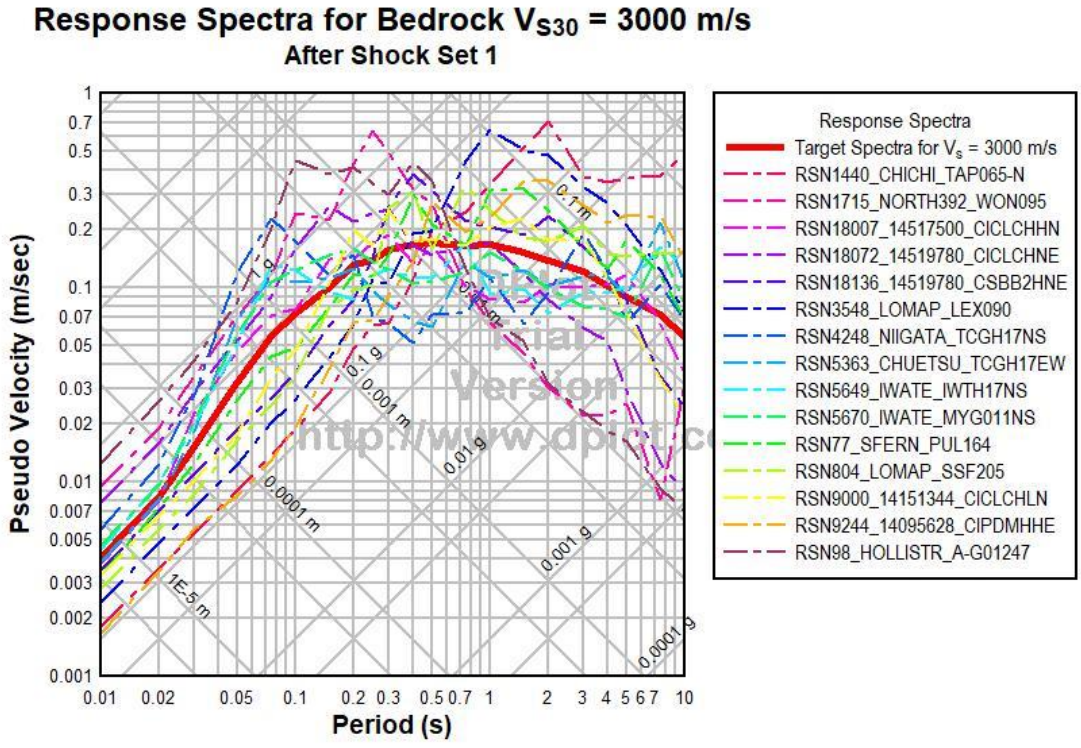

Figure A.15 Scaled response spectra for selected ground motions for the M_w7.8 April 25, 2015 main shock with target spectra for a V_{S30} = 3000 m/s bedrock, Set 1.

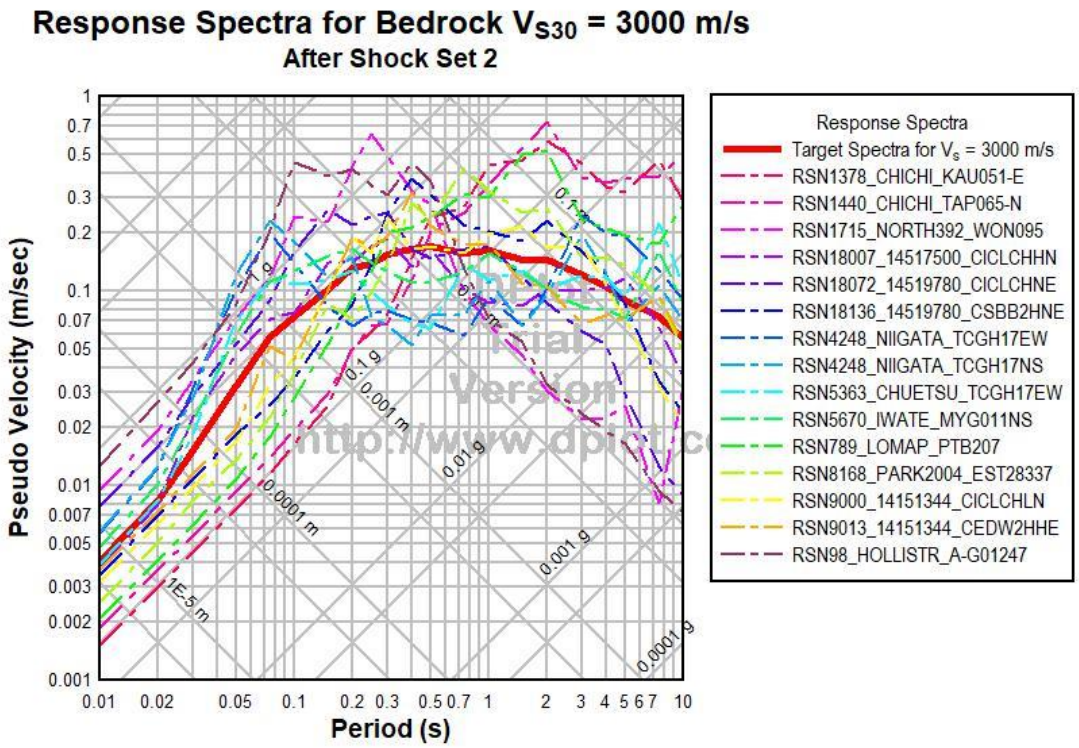

Figure A.16 Scaled response spectra for selected ground motions for the M_w7.8 April 25, 2015 main shock with target spectra for a V_{S30} = 3000 m/s bedrock, Set 2.

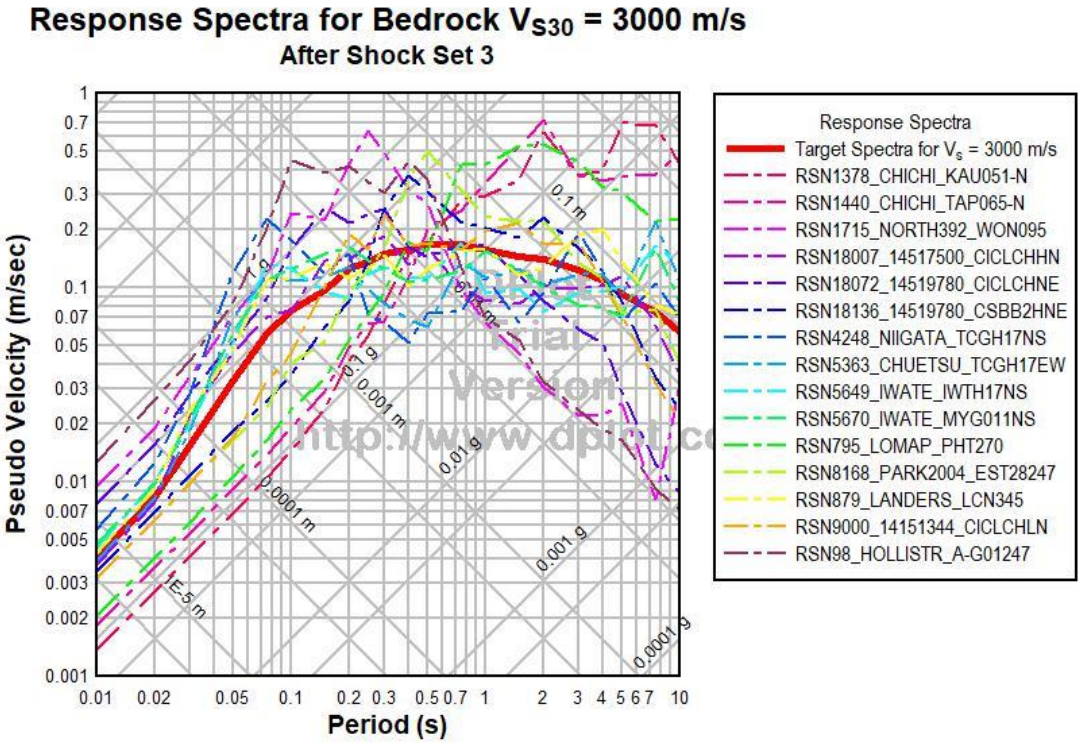

Figure A.17 Scaled response spectra for selected ground motions for the M_w7.8 April 25, 2015 main shock with target spectra for a V_{S30} = 3000 m/s bedrock, Set 3.

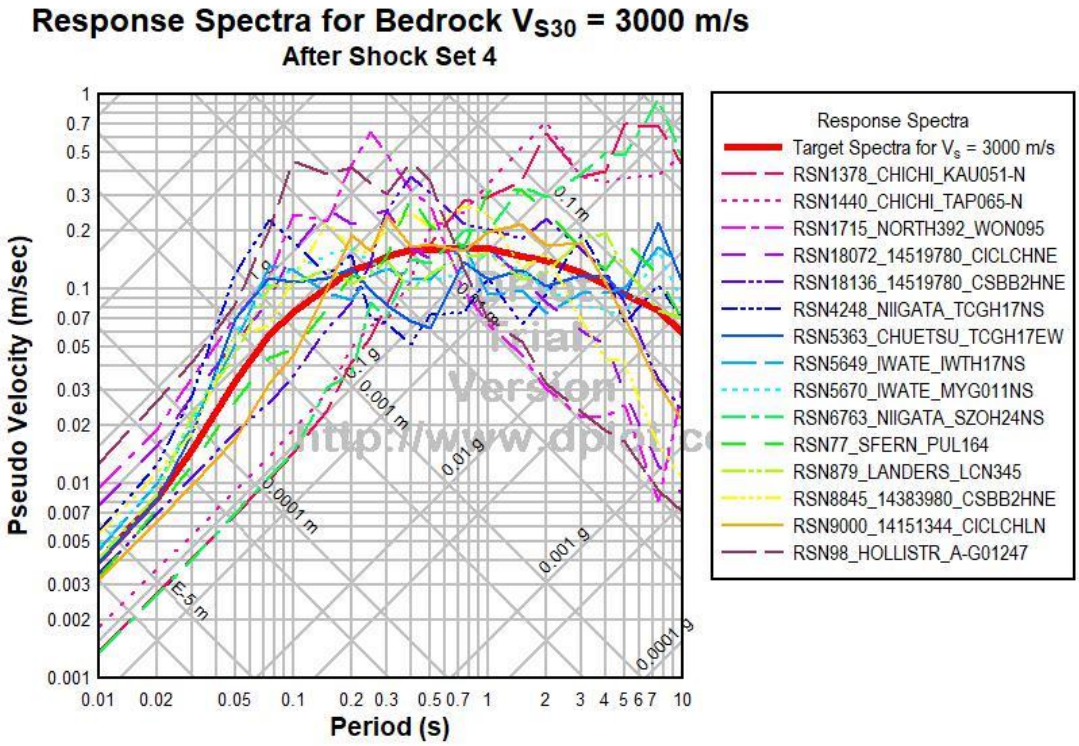

Figure A.18 Scaled response spectra for selected ground motions for the M_w7.8 April 25, 2015 main shock with target spectra for a V_{S30} = 3000 m/s bedrock, Set 4.

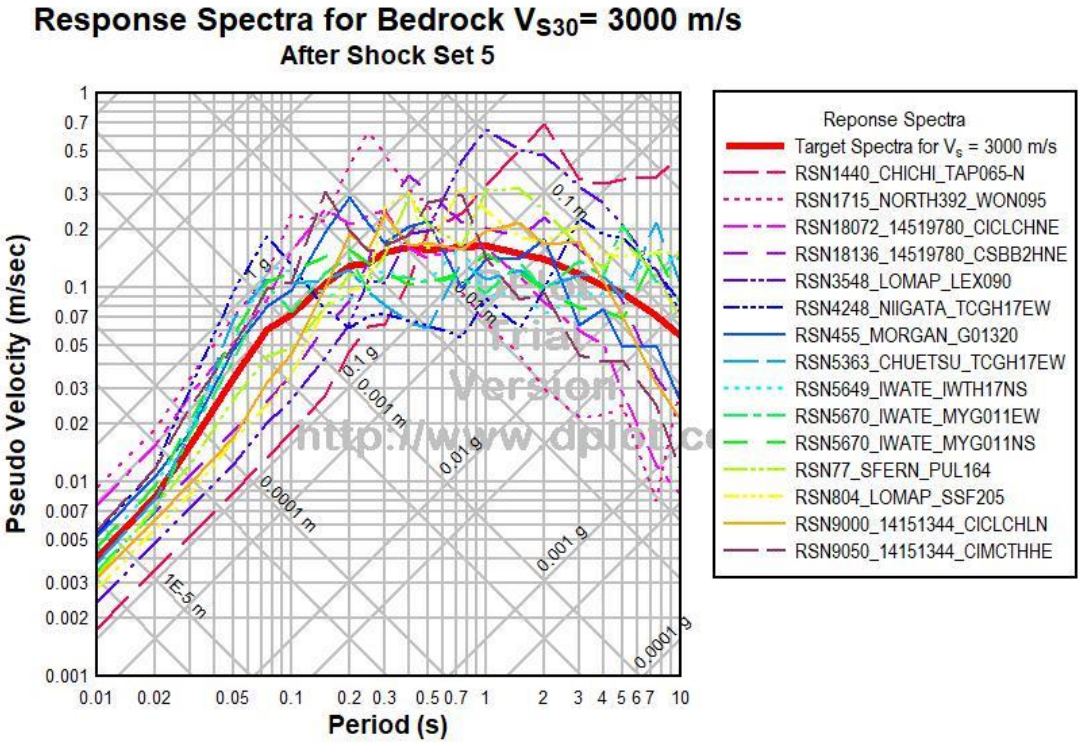

Figure A.19 Scaled response spectra for selected ground motions for the M_w7.8 April 25, 2015 main shock with target spectra for a V_{S30} = 3000 m/s bedrock, Set 5.

APPENDIX B: Predicted Settlement Distributions

The distributions of predicted settlements for both analysis approaches for Soil Profile 2 with bedrock V_{S30} = 3000 m/s, Soil Profile 3 with bedrock V_S30 = 1000 m/s and Soil Profile 3 with V_{S30} = 3000 m/s are presented in Appendix B.

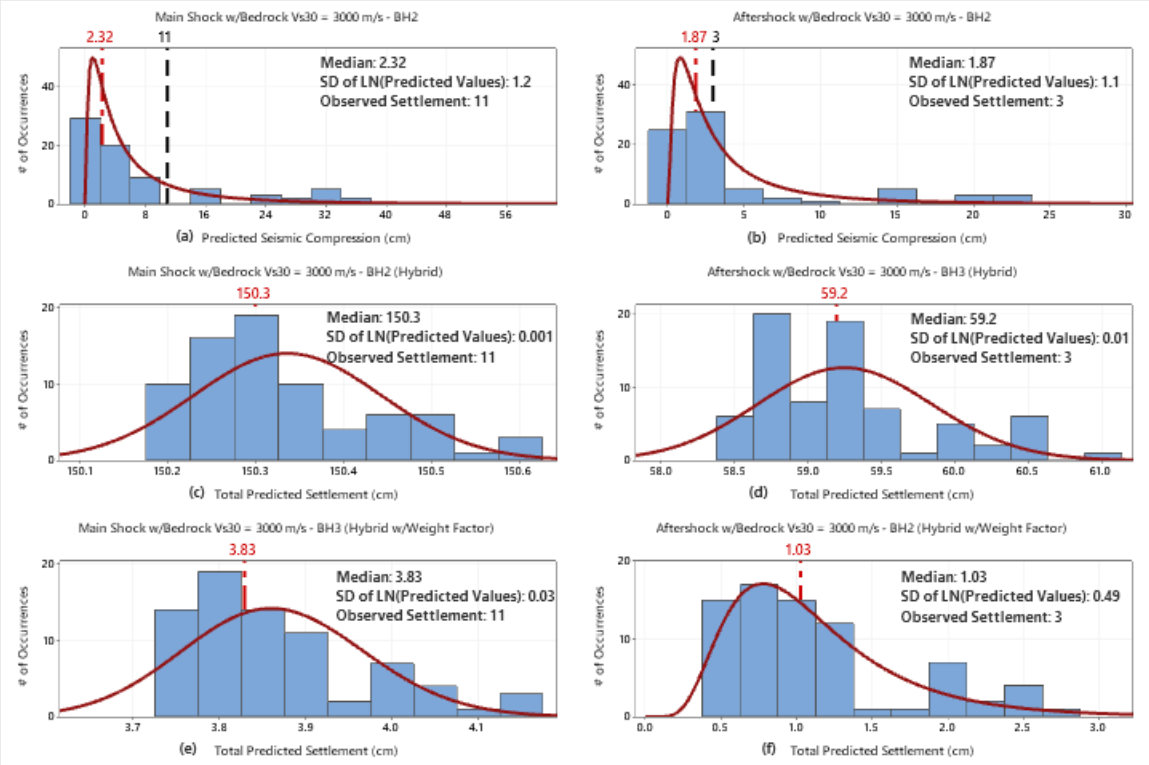

Figure B.1 Results from Soil Profile 2 for bedrock V_{S30} = 3000 m/s: (a) settlements assuming strata only underwent seismic compression for the M_w7.8, April 25, 2015 main shock; (b) settlements assuming strata only underwent seismic compression for M_w7.3, May 12, 2015 aftershock; (c) settlements assuming strata underwent seismic compression and post-liquefaction consolidation for M_w7.8, April 25, 2015 main shock with no weight factor; (d) settlements assuming strata underwent seismic compression and post-liquefaction consolidation for M_w7.3, May 12, 2015 aftershock with no weight factor; (e) settlements assuming strata underwent seismic compression and post-liquefaction consolidation for M_w7.8, April 25, 2015 main shock with weight factor; and (f) settlements assuming strata underwent seismic compression and post-liquefaction consolidation for M_w7.3, May 12, 2015 aftershock with weight factor.

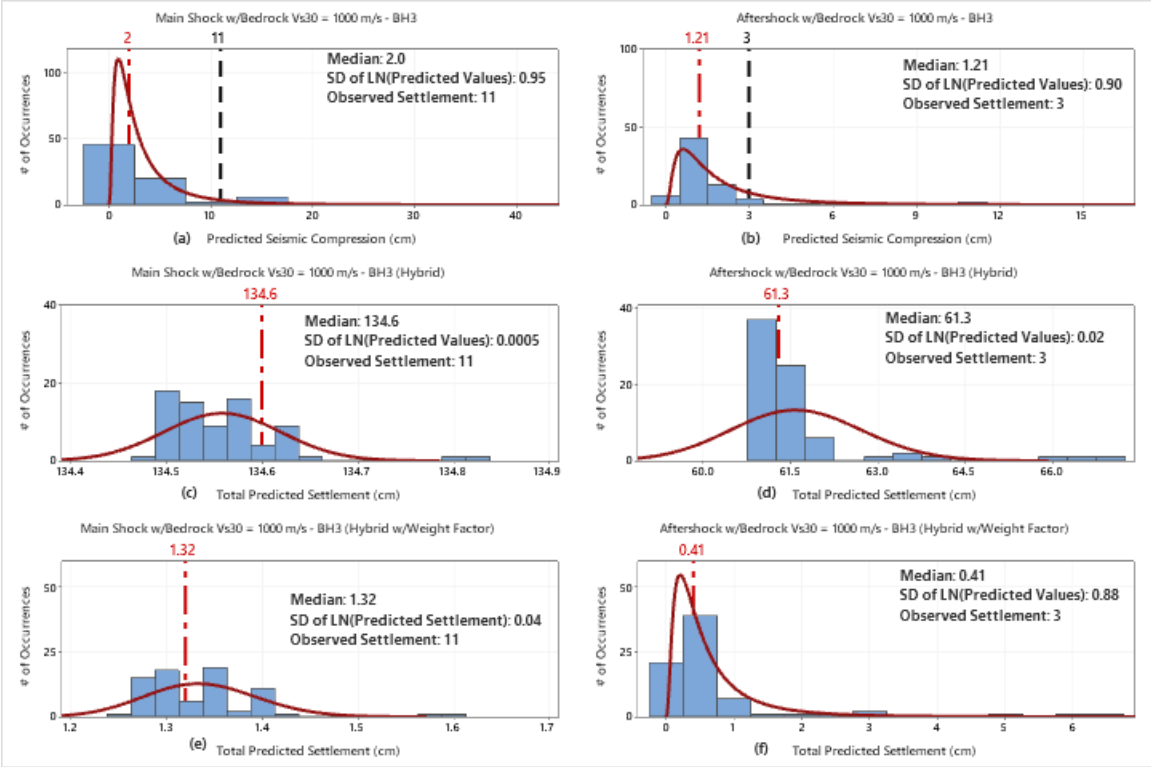

Figure B.2 Results from Soil Profile 3 for bedrock V_{S30} = 1000 m/s: (a) settlements assuming strata only underwent seismic compression for the M_w7.8, April 25, 2015 main shock; (b) settlements assuming strata only underwent seismic compression for M_w7.3, May 12, 2015 aftershock; (c) settlements assuming strata underwent seismic compression and post-liquefaction consolidation for M_w7.8, April 25, 2015 main shock with no weight factor; (d) settlements assuming strata underwent seismic compression and post-liquefaction consolidation for M_w7.3, May 12, 2015 aftershock with no weight factor; (e) settlements assuming strata underwent seismic compression and post-liquefaction consolidation for M_w7.8, April 25, 2015 main shock with weight factor; and (f) settlements assuming strata underwent seismic compression and post-liquefaction consolidation for M_w7.3, May 12, 2015 aftershock with weight factor.

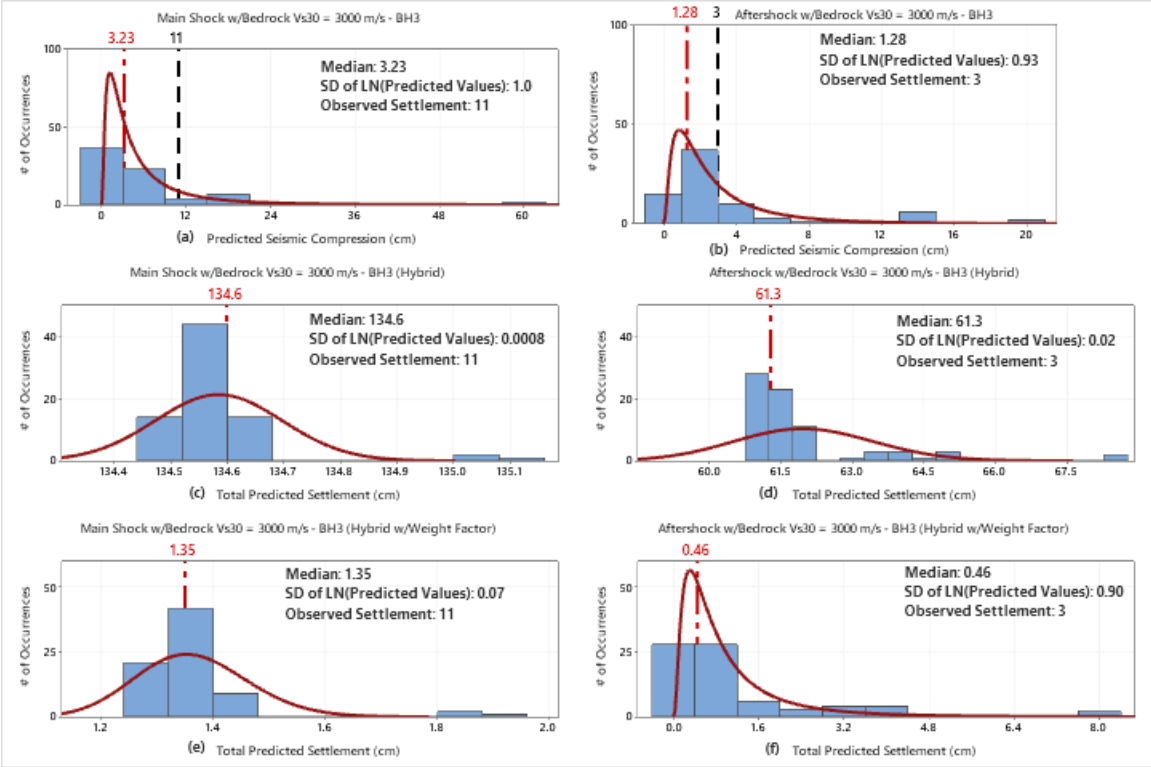

Figure B.3 Results from Soil Profile 3 for bedrock V_{S30} = 3000 m/s: (a) settlements assuming strata only underwent seismic compression for the M_w7.8, April 25, 2015 main shock; (b) settlements assuming strata only underwent seismic compression for M_w7.3, May 12, 2015 aftershock; (c) settlements assuming strata underwent seismic compression and post-liquefaction consolidation for M_w7.8, April 25, 2015 main shock with no weight factor; (d) settlements assuming strata underwent seismic compression and post-liquefaction consolidation for M_w7.3, May 12, 2015 aftershock with no weight factor; (e) settlements assuming strata underwent seismic compression and post-liquefaction consolidation for M_w7.8, April 25, 2015 main shock with weight factor; and (f) settlements assuming strata underwent seismic compression and post-liquefaction consolidation for M_w7.3, May 12, 2015 aftershock with weight factor.

APPENDIX C: Predicted Settlement with Depth

The amount of predicted settlement experienced in each soil layer for both analysis approaches for Soil Profile 2 with bedrock V_{S30} = 3000 m/s for the M_w7.8 April 25, 2015 main shock, Soil Profile 2 with bedrock V_{S30} = 1000 and 3000 m/s for the M_w7.3 May 12, 2015 aftershock, and Soil Profile 3 with bedrock V_{S30} = 1000 m/s and 3000 m/s for both earthquakes are shown in Appendix C. One ground motion that predicted the median settlement value from each of the eight scenarios was utilized in the creation of these plots.

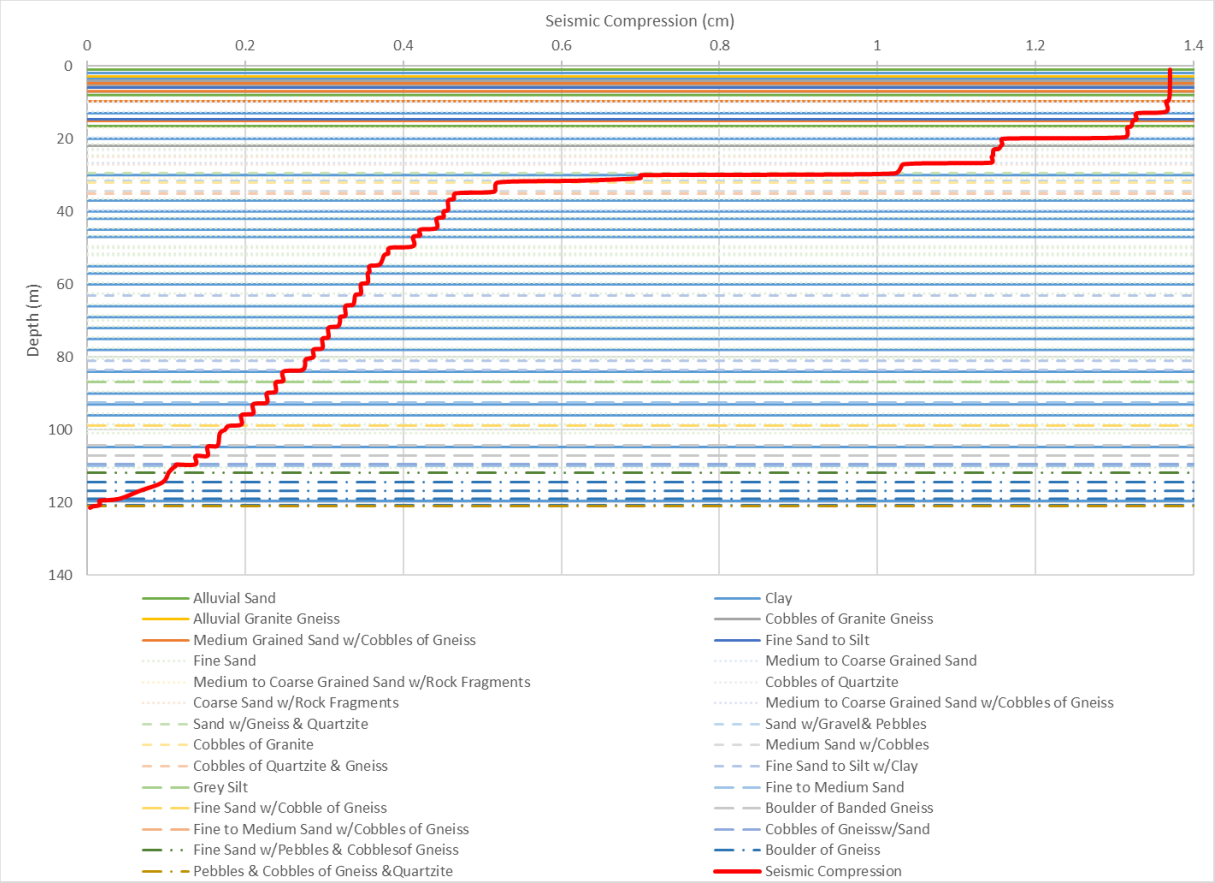

Figure C.1 Predicted settlement for each layer in Soil Profile 2 for one representative ground motion scaled for the M_w7.3 May 12, 2015 aftershock with V_{S30} = 1000 m/s assuming strata only underwent seismic compression.

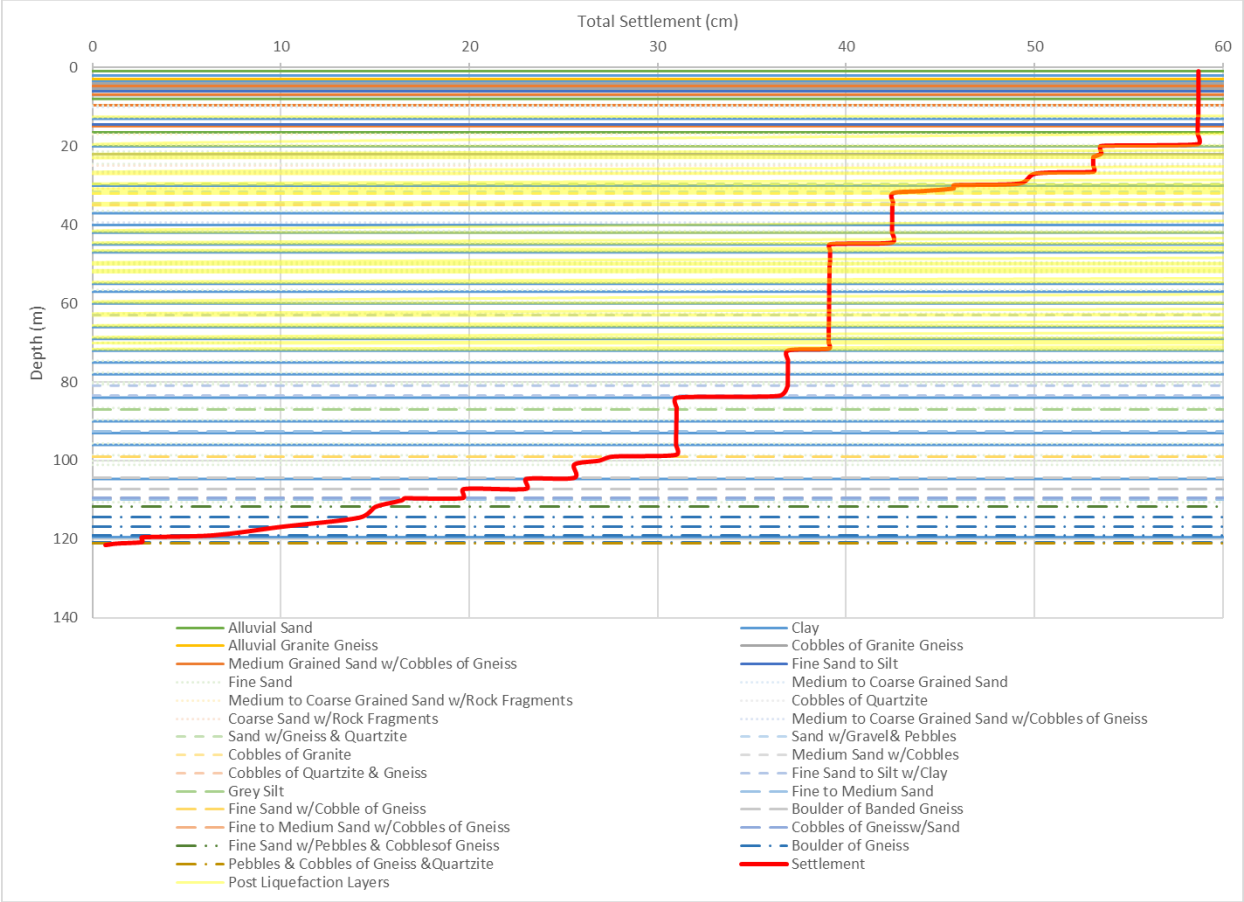

Figure C.2 Predicted settlement for each layer in Soil Profile 2 for one representative ground motion scaled for the M_w7.3 May 12, 2015 aftershock with V_{S30} = 1000 m/s assuming strata underwent seismic compression and post-liquefaction consolidation with no weight factor.

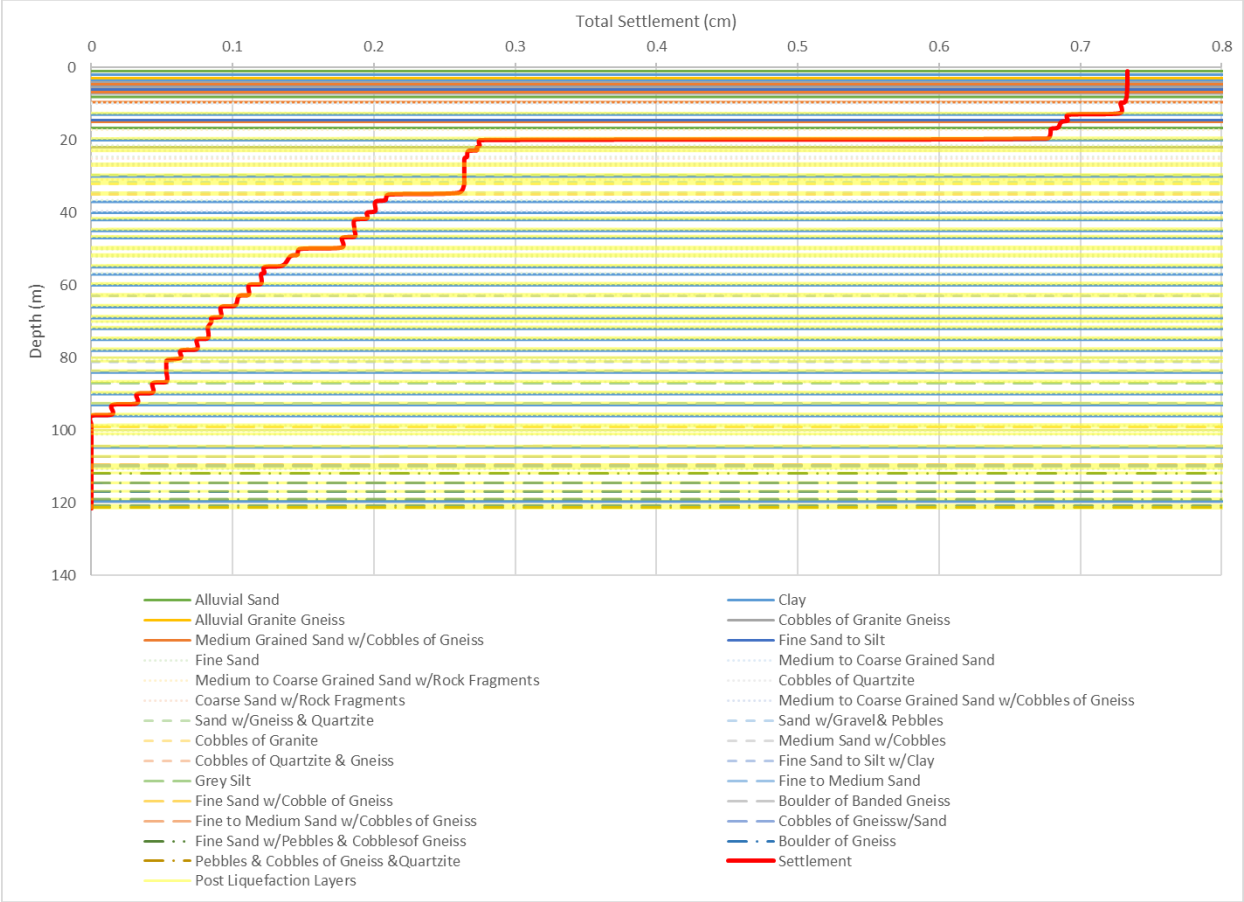

Figure C.3 Predicted settlement for each layer in Soil Profile 2 for one representative ground motion scaled for the M_w7.3 May 12, 2015 aftershock with V_{S30} = 1000 m/s assuming strata underwent seismic compression and post-liquefaction consolidation with weight factor.

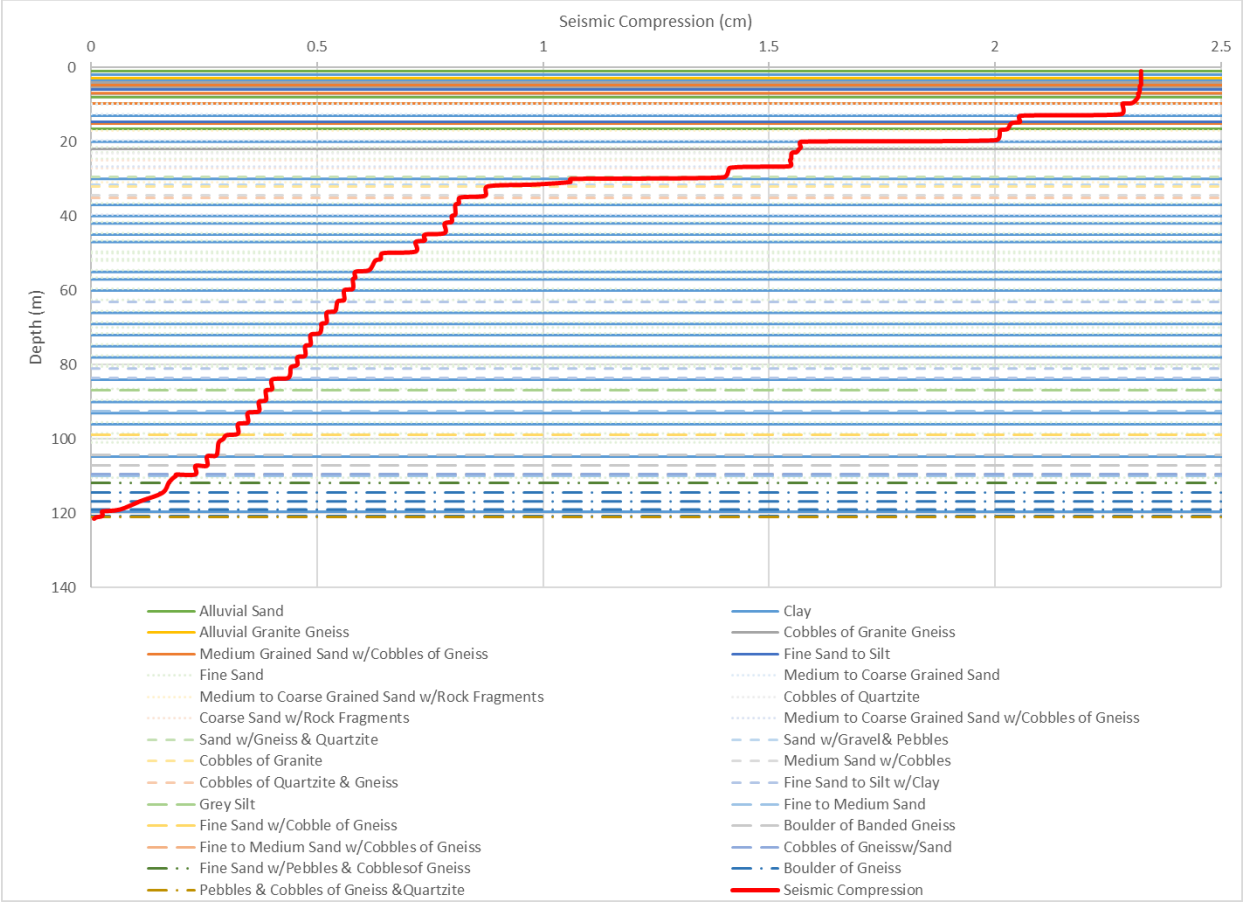

Figure C.4 Predicted settlement for each layer in Soil Profile 2 for one representative ground motion scaled for the M_w7.8 April 25, 2015 main shock with V_{S30} = 3000 m/s assuming strata only underwent seismic compression.

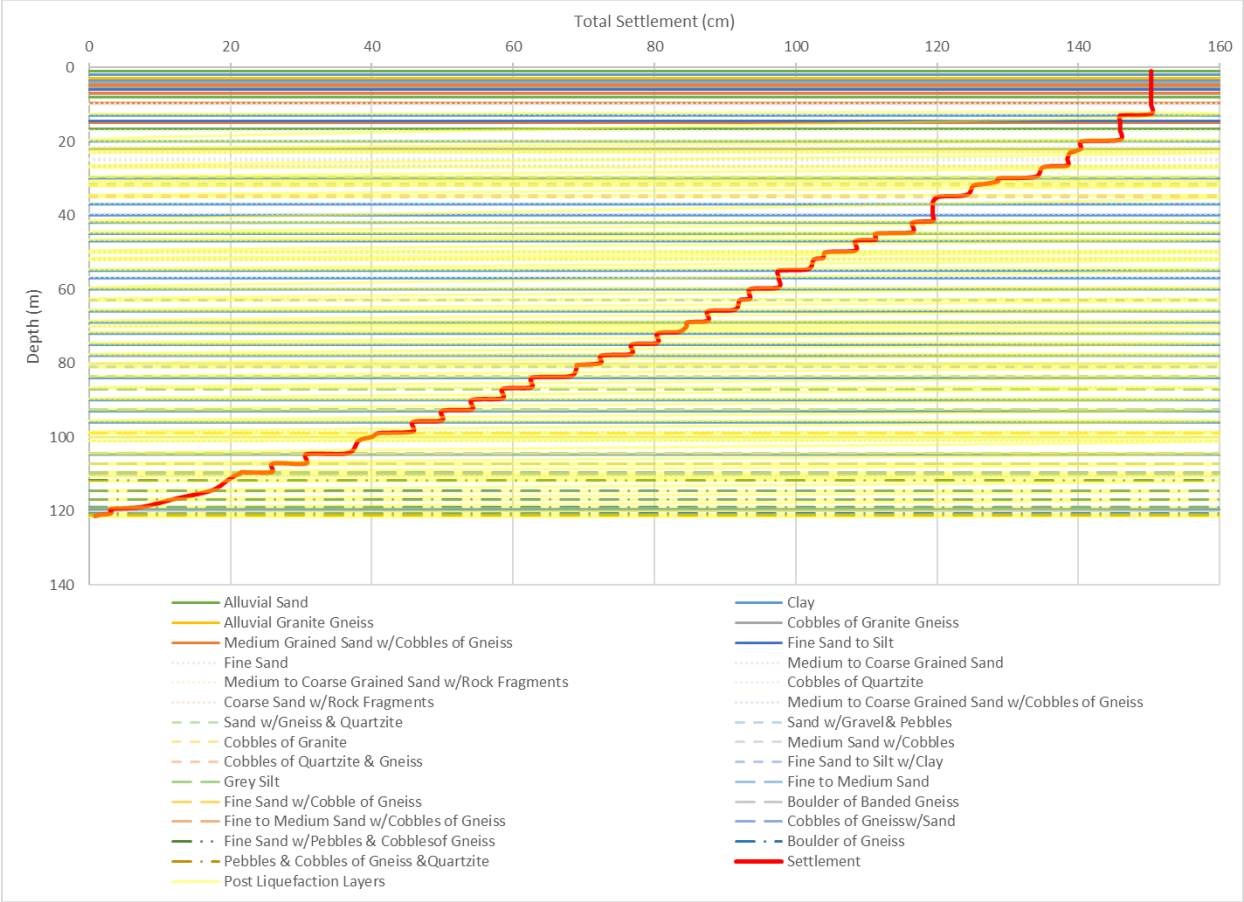

Figure C.5 Predicted settlement for each layer in Soil Profile 2 for one representative ground motion scaled for the M_w7.8 April 25, 2015 main shock with V_{S30} = 3000 m/s assuming strata underwent seismic compression and post-liquefaction consolidation with no weight factor.

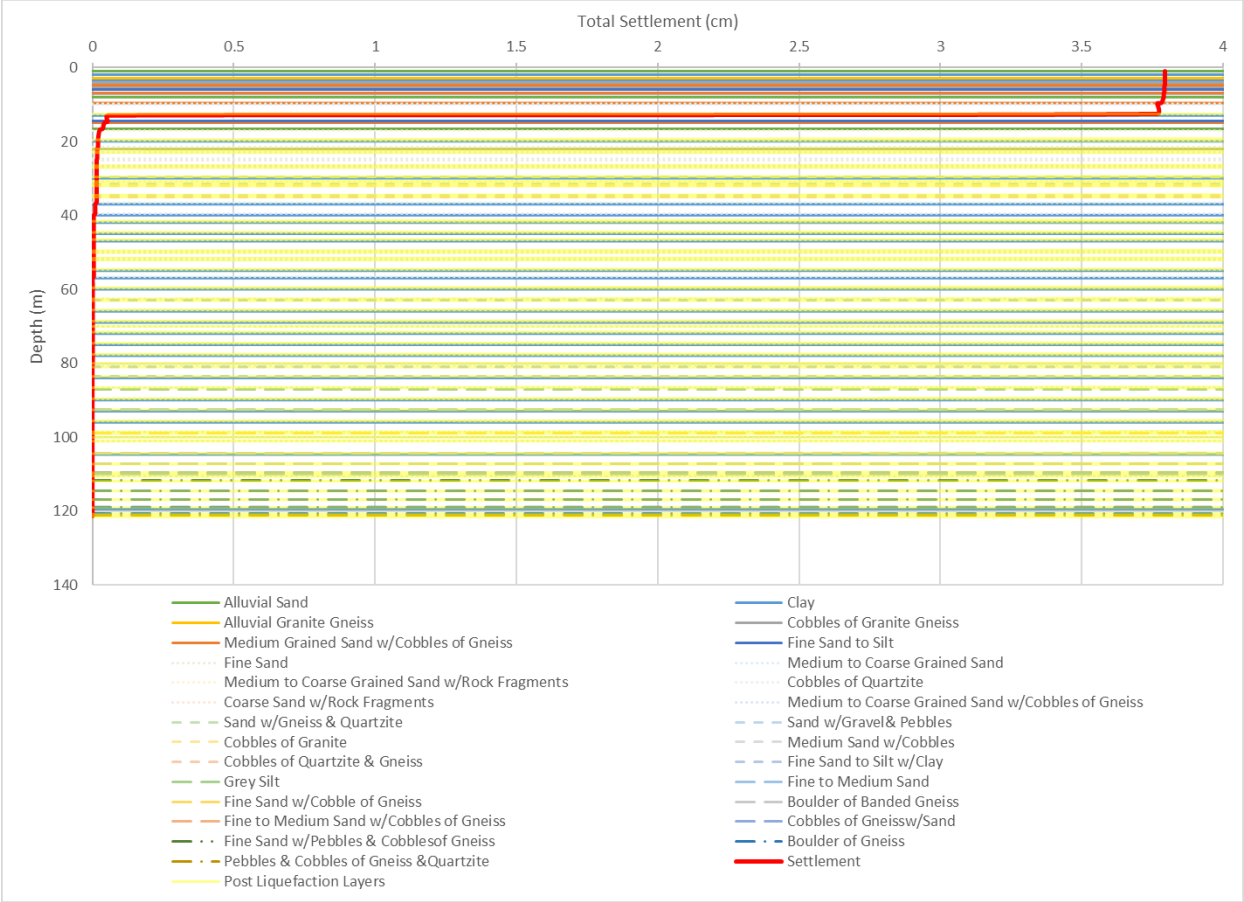

Figure C.6 Predicted settlement for each layer in Soil Profile 2 for one representative ground motion scaled for the M_w7.8 April 25, 2015 main shock with V_{S30} = 3000 m/s assuming strata underwent seismic compression and post-liquefaction consolidation with weight factor.

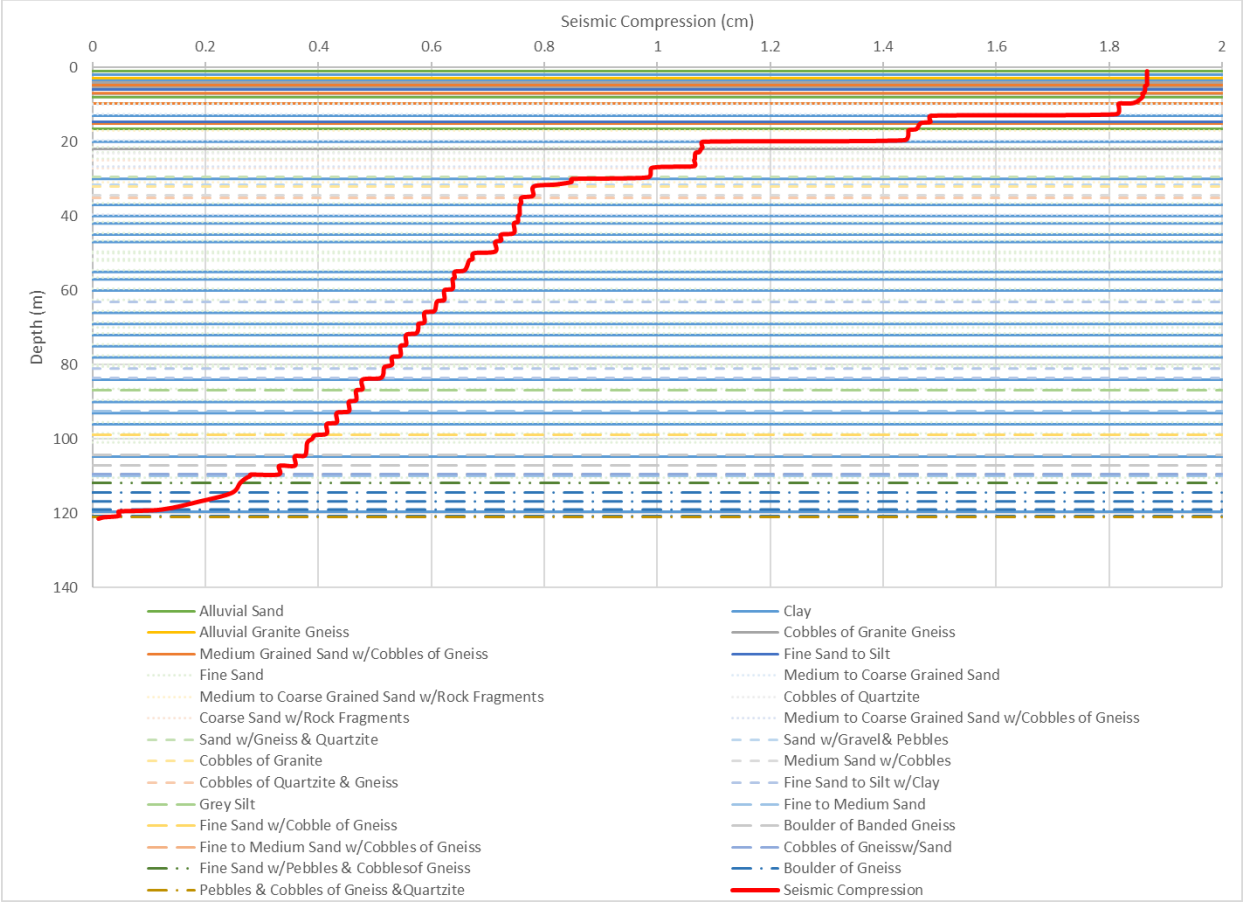

Figure C.7 Predicted settlement for each layer in Soil Profile 2 for one representative ground motion scaled for the M_w7.3 May 12, 2015 aftershock with V_{S30} = 3000 m/s assuming strata only underwent seismic compression.

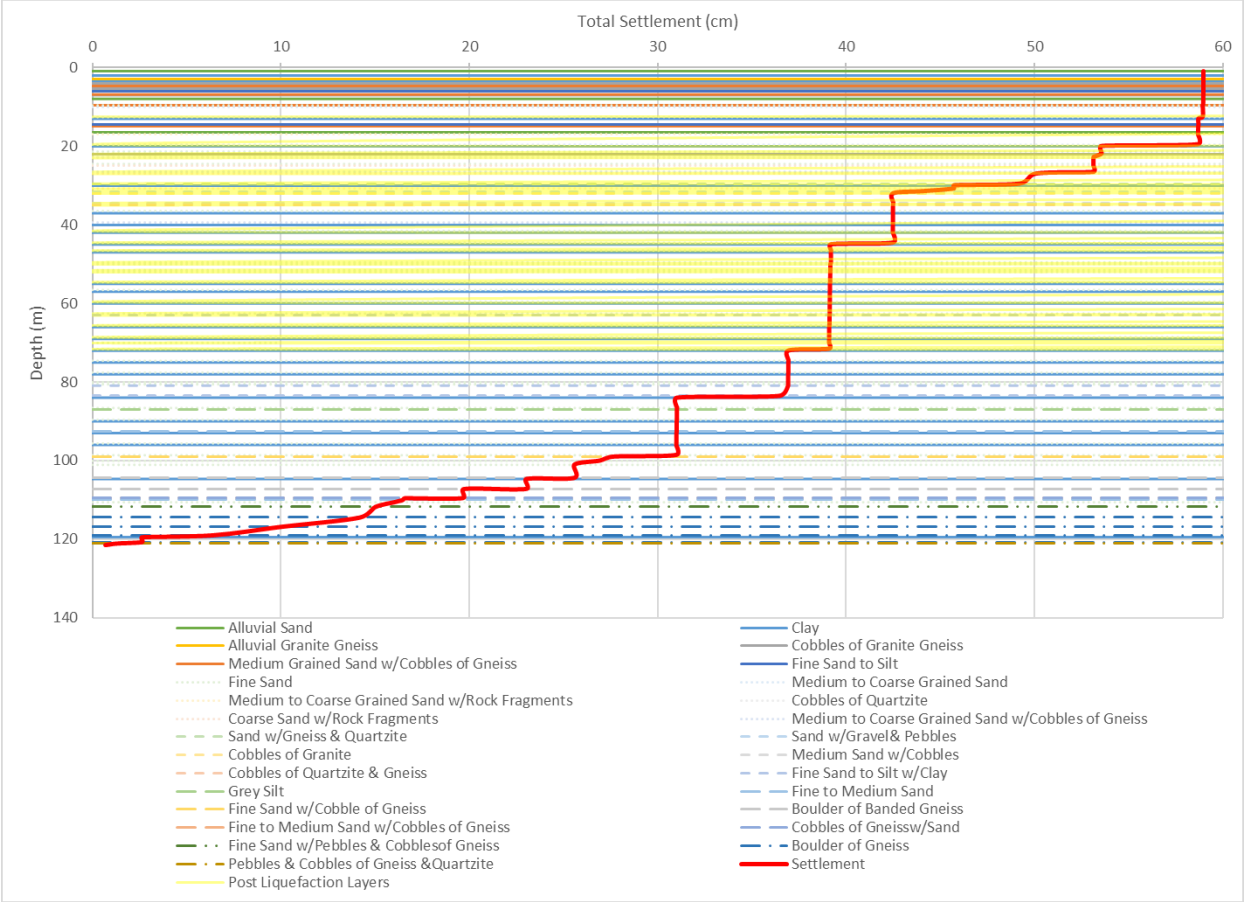

Figure C.8 Predicted settlement for each layer in Soil Profile 2 for one representative ground motion scaled for the M_w7.3 May 12, 2015 aftershock with V_{S30} = 3000 m/s assuming strata underwent seismic compression and post-liquefaction consolidation with no weight factor.

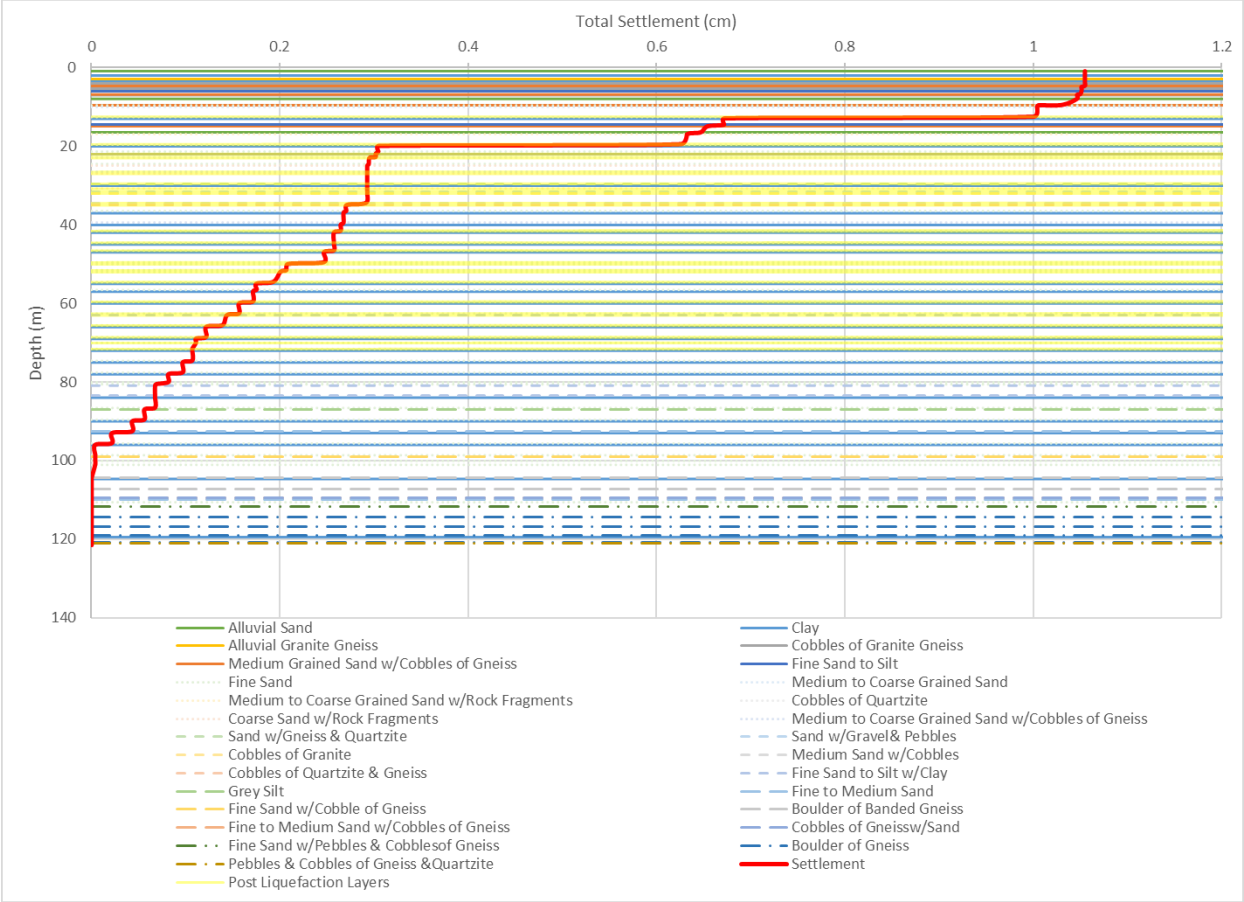

Figure C.9 Predicted settlement for each layer in Soil Profile 2 for one representative ground motion scaled for the M_w7.3 May 12, 2015 aftershock with V_{S30} = 3000 m/s assuming strata underwent seismic compression and post-liquefaction consolidation with weight factor.

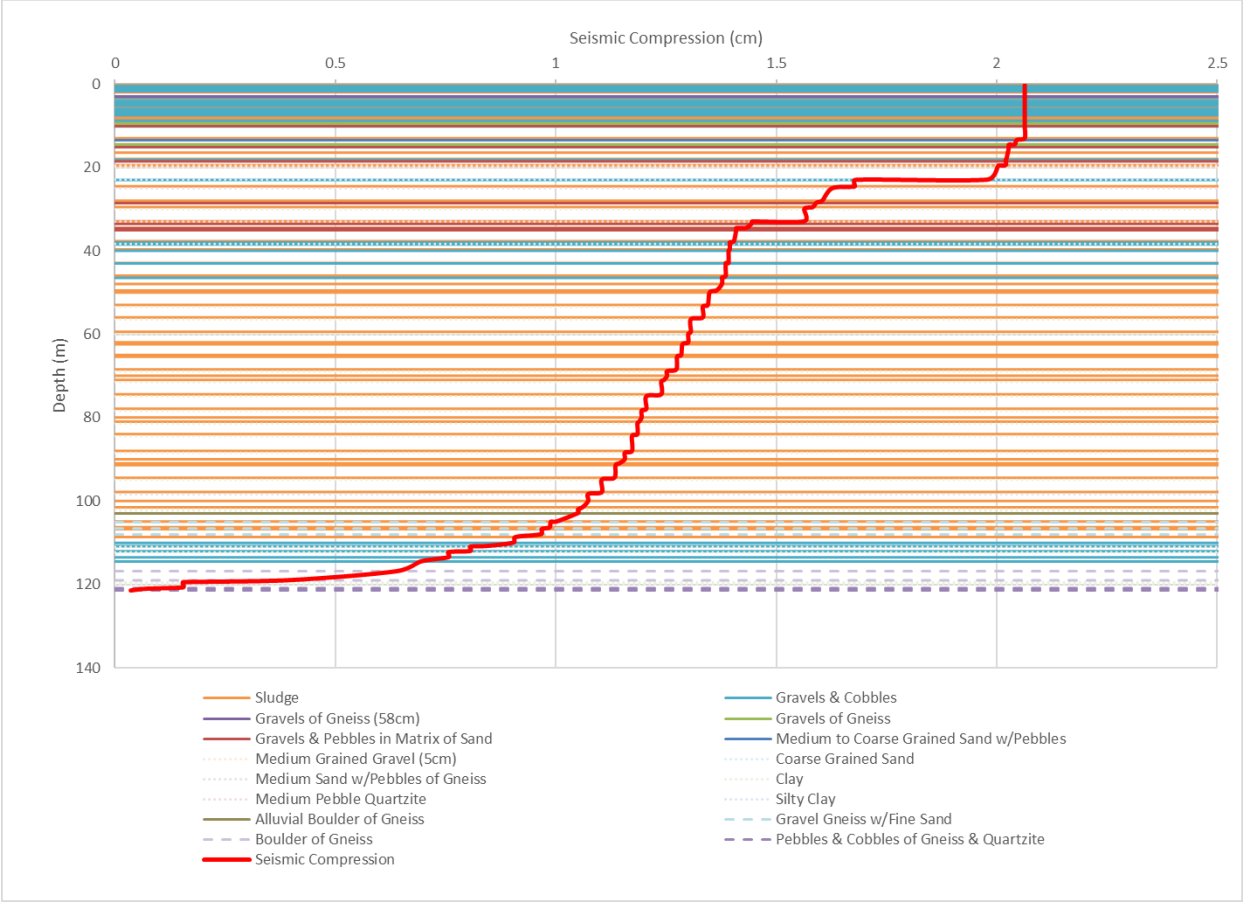

Figure C.10 Predicted settlement for each layer in Soil Profile 3 for one representative ground motion scaled for the M_w7.8 April 25, 2015 main shock with V_{S30} = 1000 m/s assuming strata only underwent seismic compression.

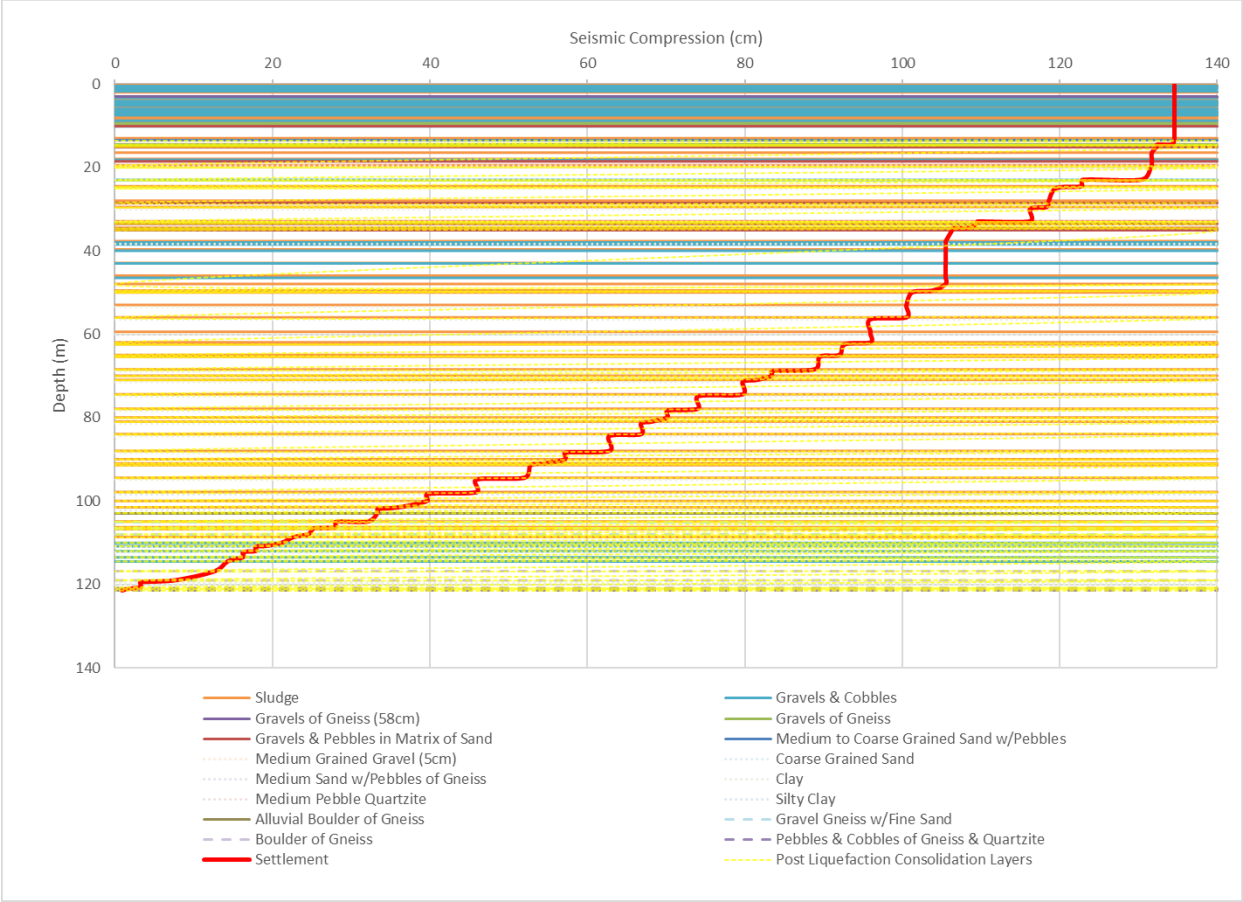

Figure C.11 Predicted settlement for each layer in Soil Profile 3 for one representative ground motion scaled for the M_w7.8 April 25, 2015 main shock with V_{S30} = 1000 m/s assuming strata underwent seismic compression and post-liquefaction consolidation with no weight factor.

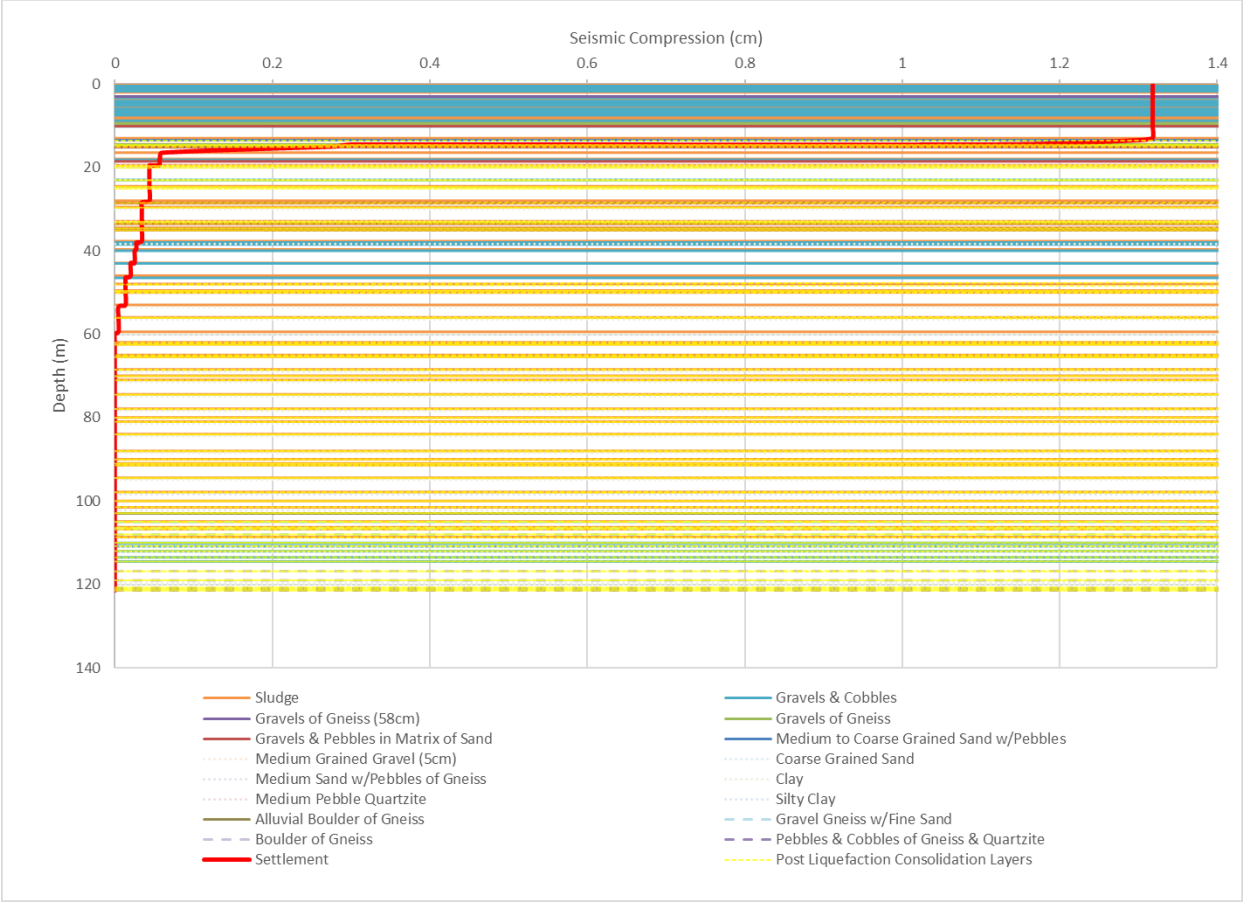

Figure C.12 Predicted settlement for each layer in Soil Profile 3 for one representative ground motion scaled for the M_w7.8 April 25, 2015 main shock with V_{S30} = 1000 m/s assuming strata underwent seismic compression and post-liquefaction consolidation with weight factor.

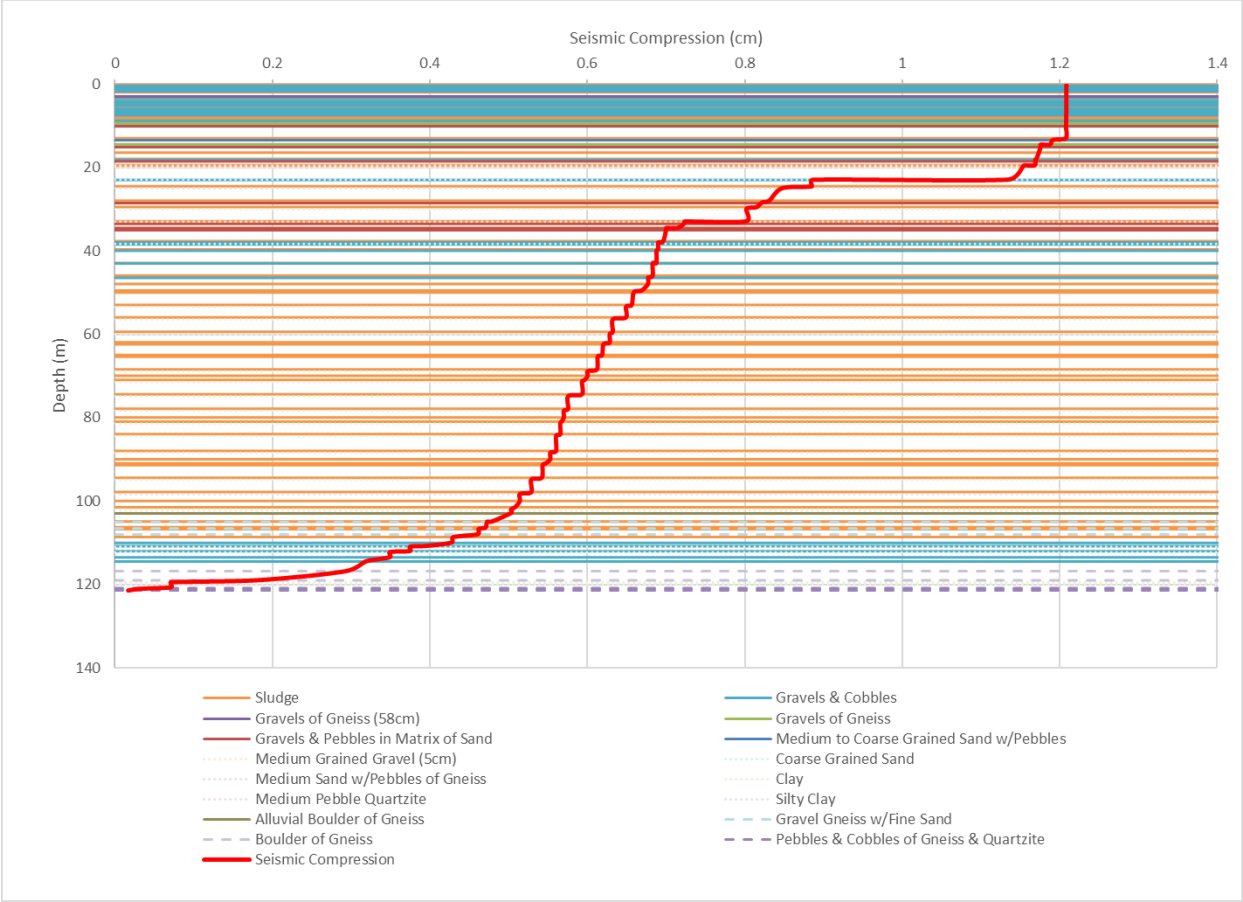

Figure C.13 Predicted settlement for each layer in Soil Profile 3 for one representative ground motion scaled for the M_w7.3 May 12, 2015 aftershock with V_{S30} = 1000 m/s assuming strata only underwent seismic compression.

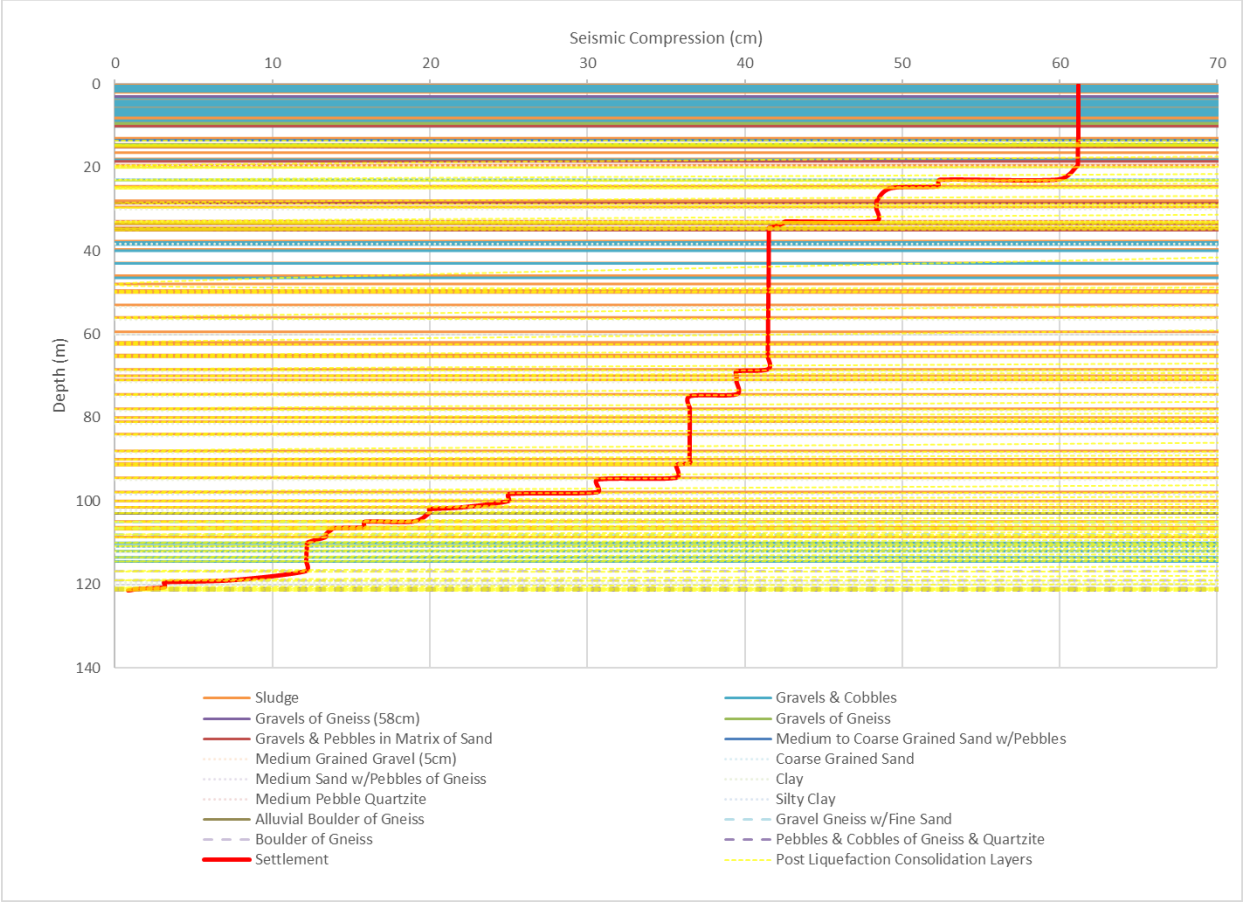

Figure C.14 Predicted settlement for each layer in Soil Profile 3 for one representative ground motion scaled for the M_w7.3 May 12, 2015 aftershock with V_{S30} = 1000 m/s assuming strata underwent seismic compression and post-liquefaction consolidation with no weight factor.

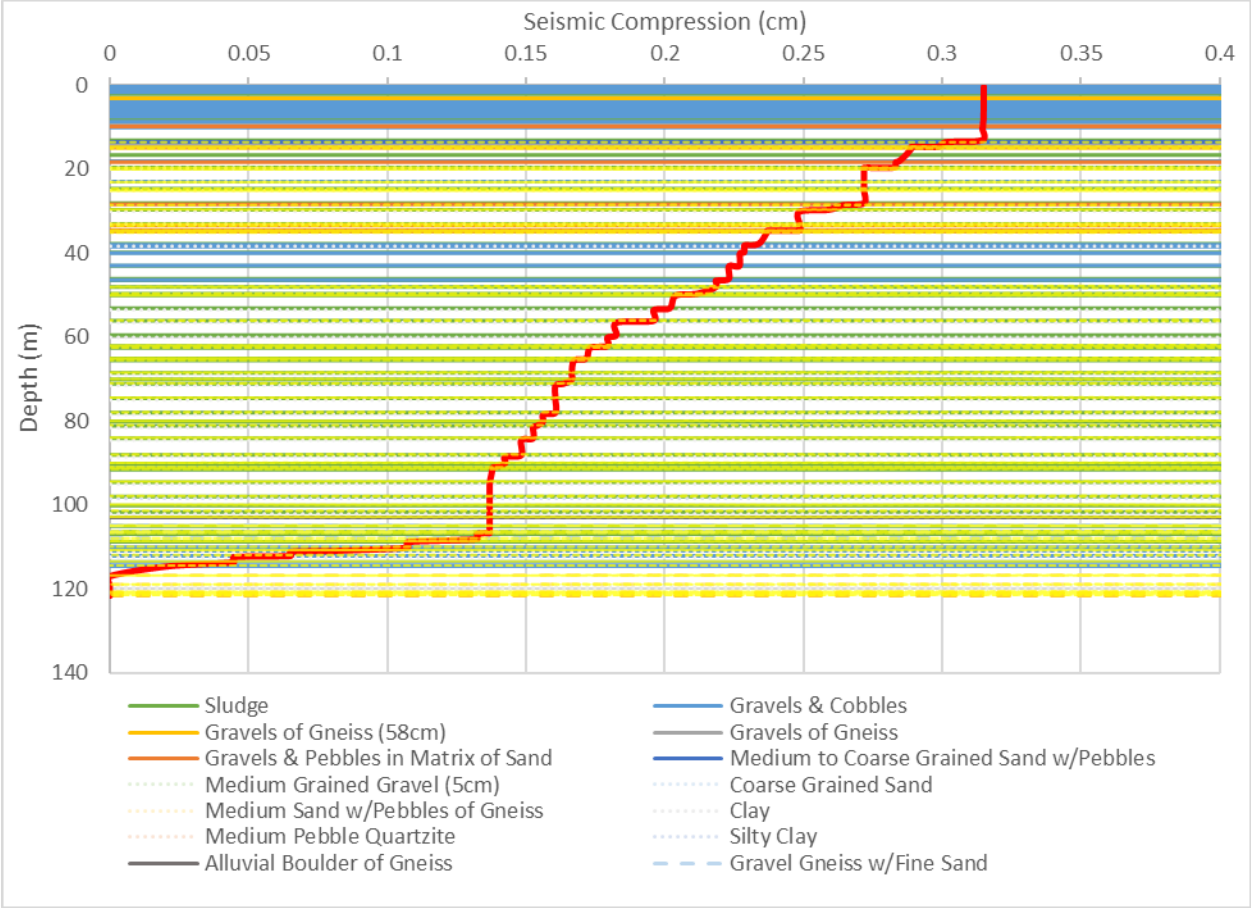

Figure C.15 Predicted settlement for each layer in Soil Profile 3 for one representative ground motion scaled for the M_w7.3 May 12, 2015 aftershock with V_{S30} = 1000 m/s assuming strata underwent seismic compression and post-liquefaction consolidation with weight factor.

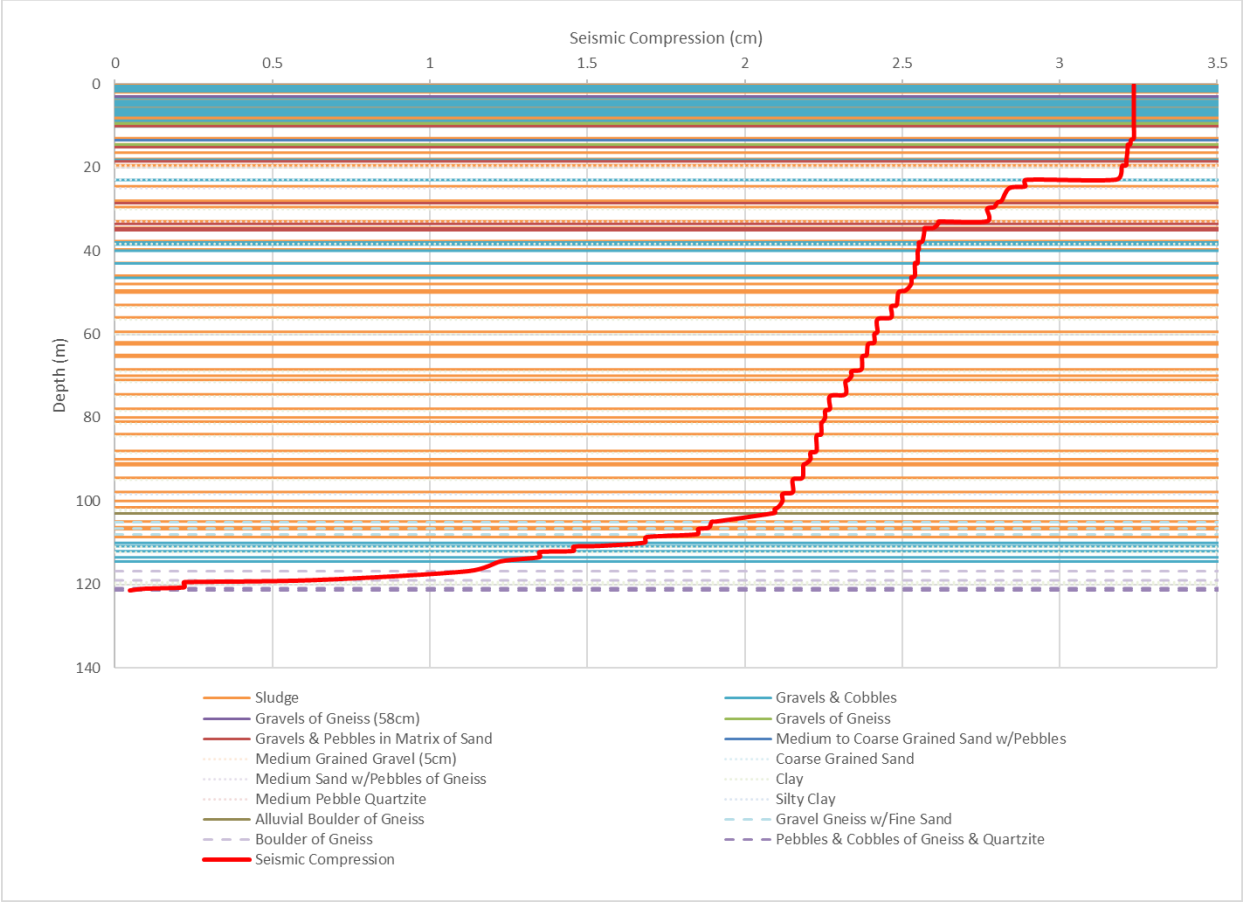

Figure C.16 Predicted settlement for each layer in Soil Profile 3 for one representative ground motion scaled for the M_w7.8 April 25, 2015 main shock with V_{S30} = 3000 m/s assuming strata only underwent seismic compression.

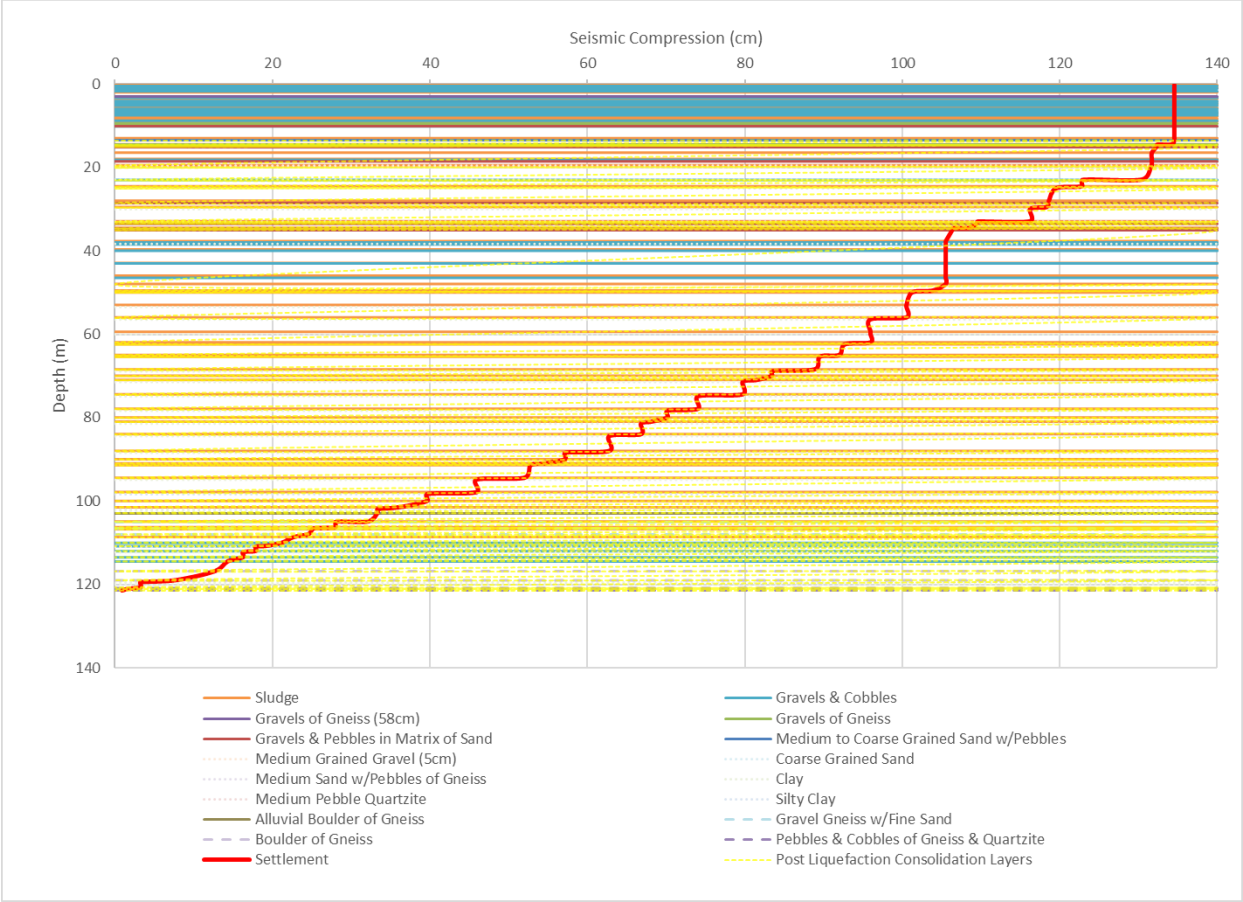

Figure C.17 Predicted settlement for each layer in Soil Profile 3 for one representative ground motion scaled for the M_w7.8 April 25, 2015 main shock with V_{S30} = 3000 m/s assuming strata underwent seismic compression and post-liquefaction consolidation with no weight factor.

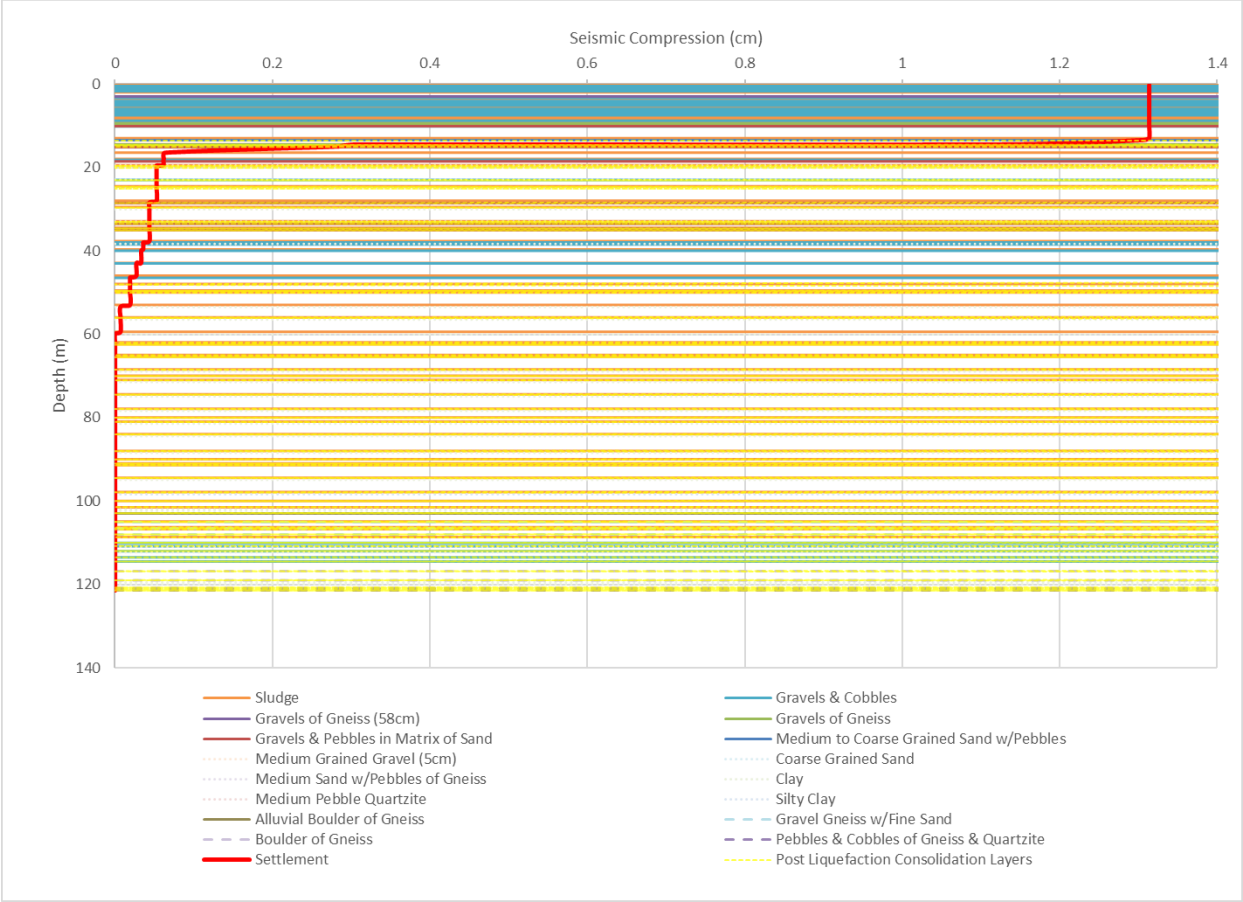

Figure C.18 Predicted settlement for each layer in Soil Profile 3 for one representative ground motion scaled for the M_w7.8 April 25, 2015 main shock with V_{S30} = 3000 m/s assuming strata underwent seismic compression and post-liquefaction consolidation with weight factor.

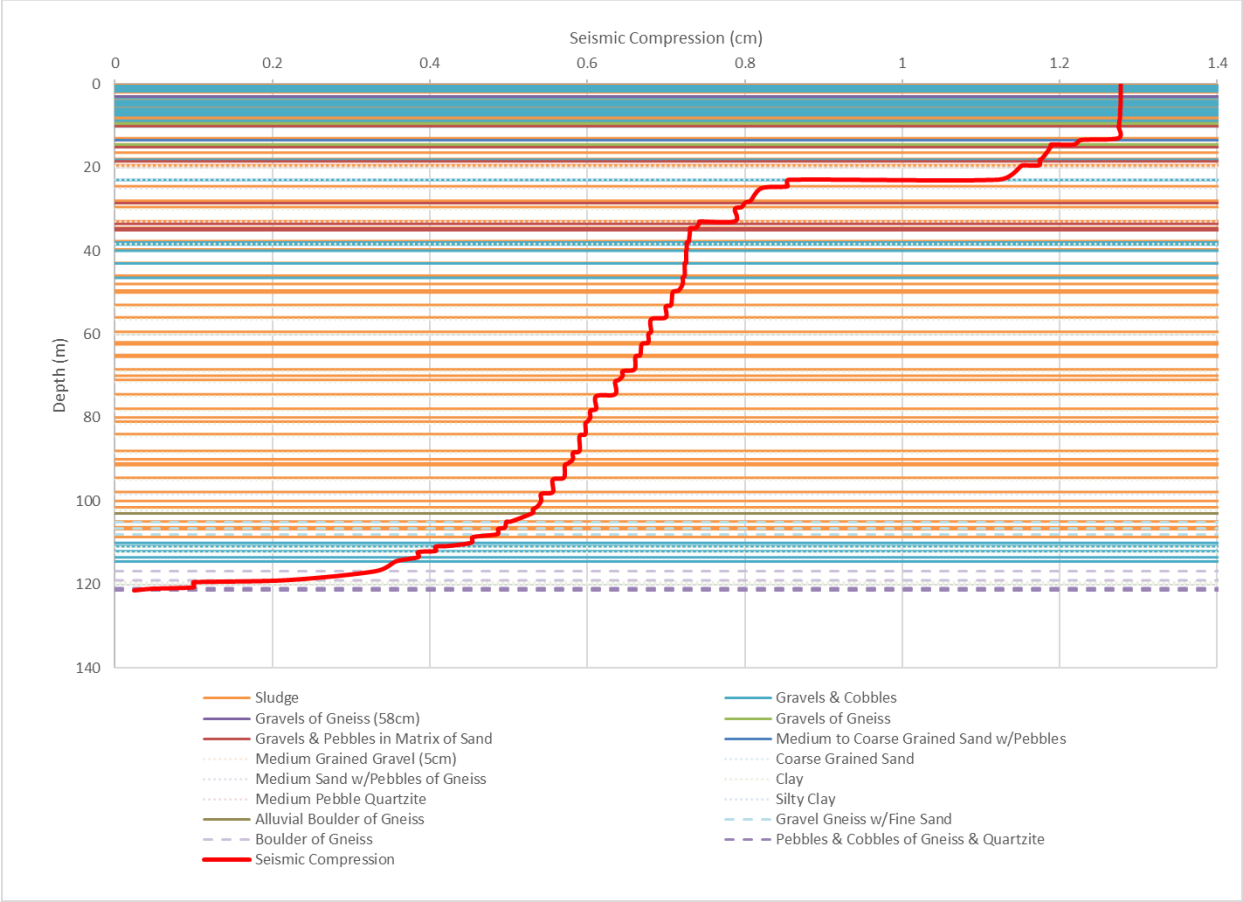

Figure C.19 Predicted settlement for each layer in Soil Profile 3 for one representative ground motion scaled for the M_w7.3 May 12, 2015 aftershock with V_{S30} = 3000 m/s assuming strata only underwent seismic compression.

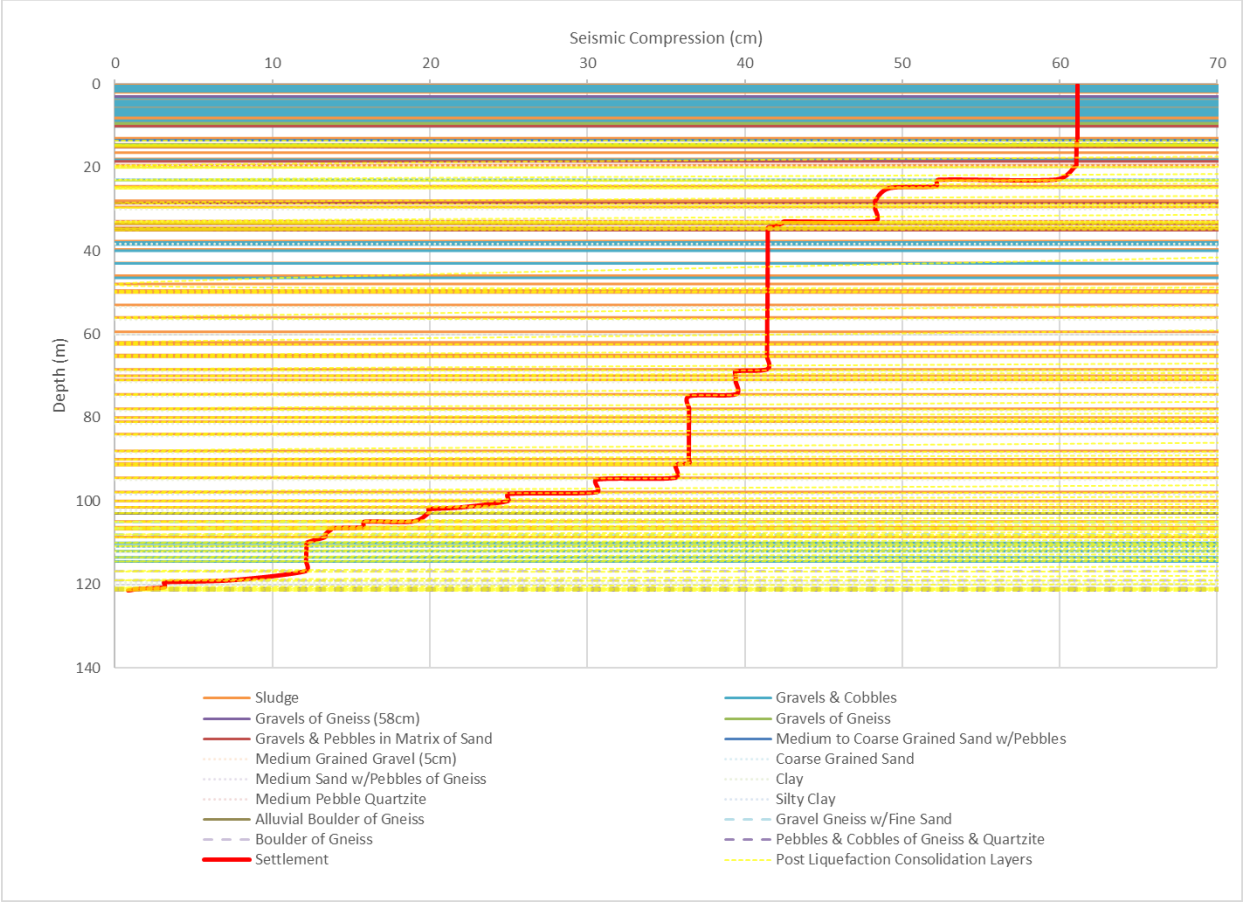

Figure C.20 Predicted settlement for each layer in Soil Profile 3 for one representative ground motion scaled for the M_w7.3 May 12, 2015 aftershock with V_{S30} = 3000 m/s assuming strata underwent seismic compression and post-liquefaction consolidation with no weight factor.

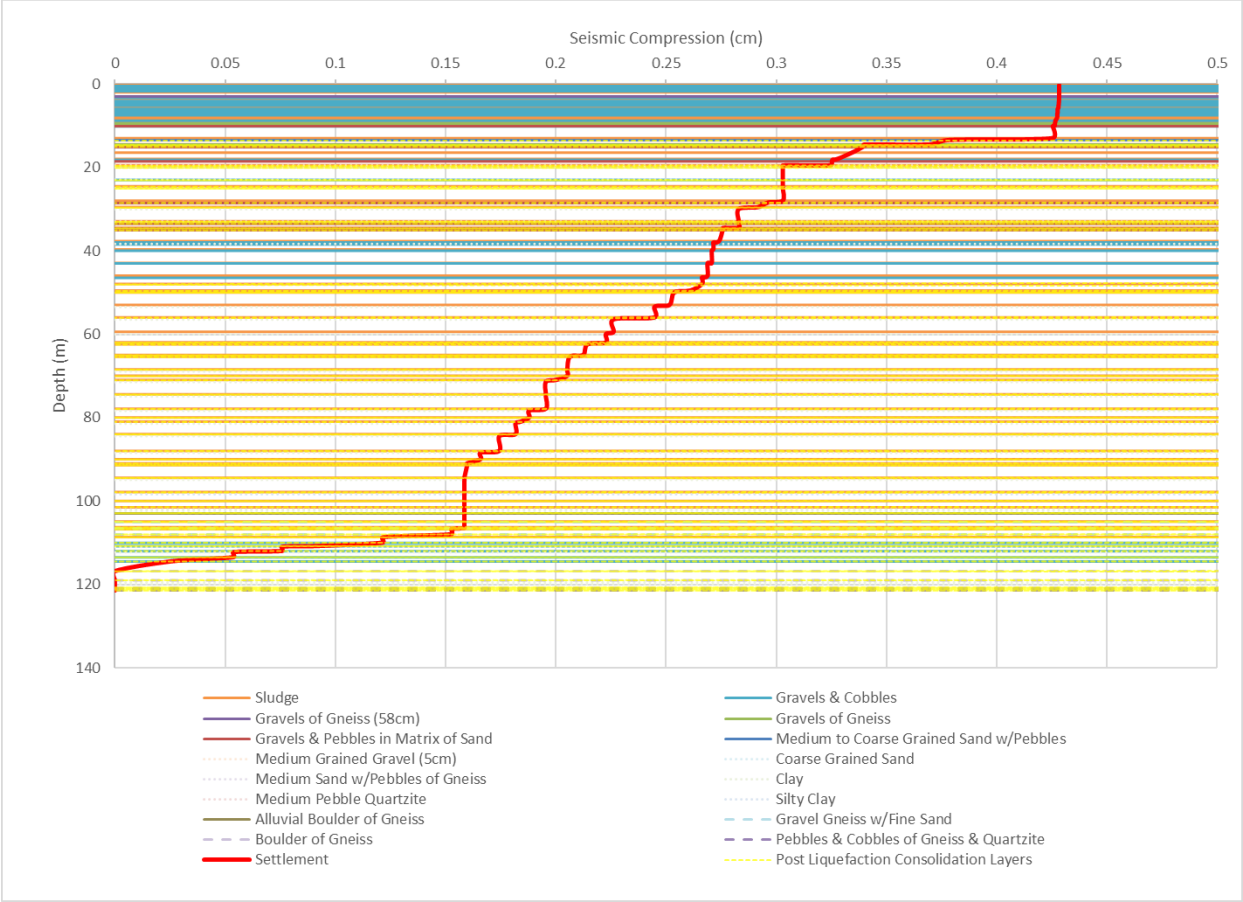

Figure C.21 Predicted settlement for each layer in Soil Profile 3 for one representative ground motion scaled for the M_w7.3 May 12, 2015 aftershock with V_{S30} = 3000 m/s assuming strata underwent seismic compression and post-liquefaction consolidation with weight factor.

APPENDIX D: Peak Shear Strain Profiles

The profiles of the peak shear strain experienced in each soil strata versus depth are presented in Appendix D. Each graph represents one set of 15 scaled ground motions based on the earthquake.

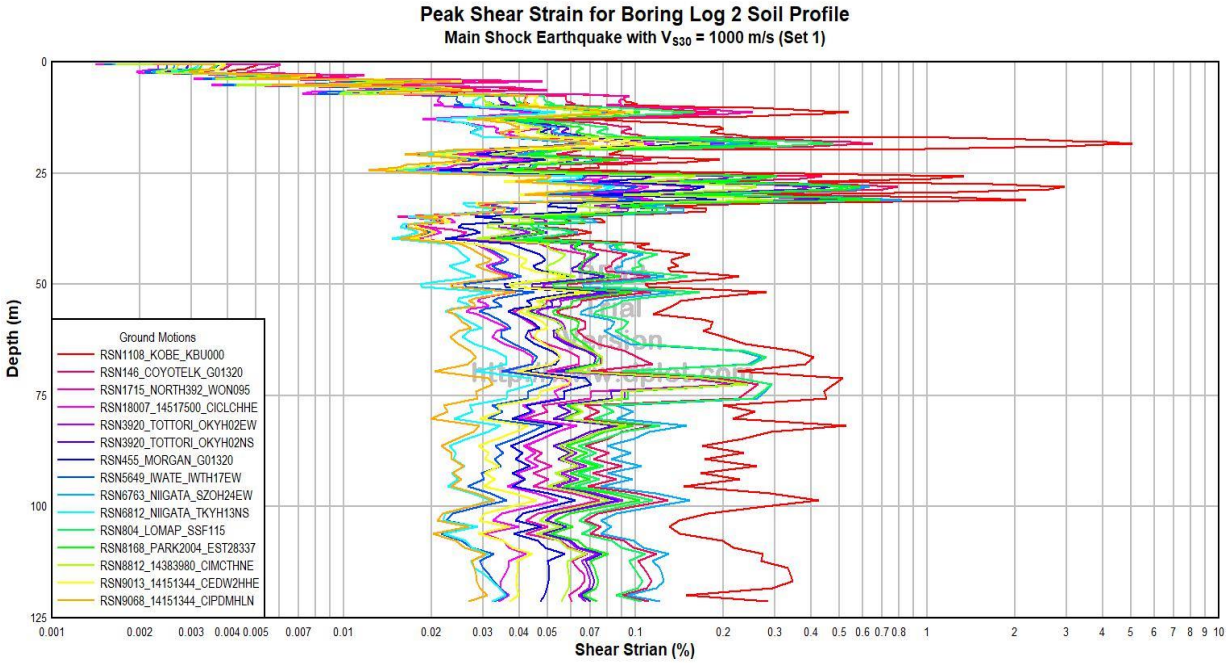

Figure D.1 Peak shear strain versus depth for Soil Profile 2, M_w7.8 April 25, 2015 main shock, V_{S30} = 1000 m/s, Set 1.

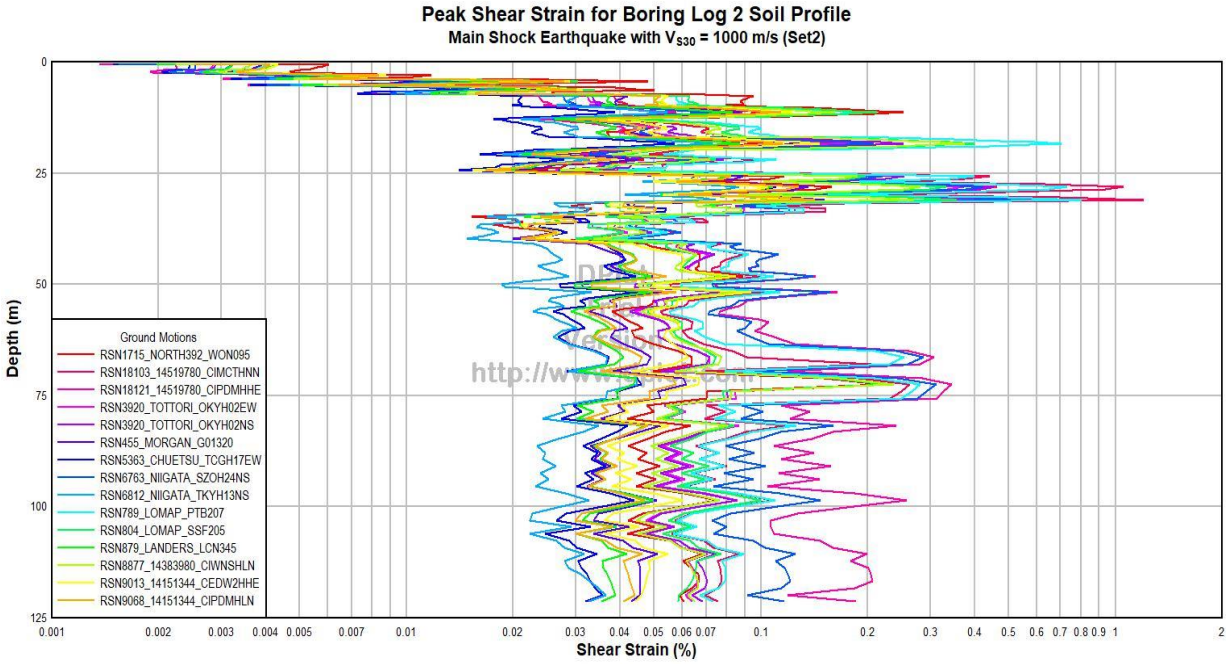

Figure D.2 Peak shear strain versus depth for Soil Profile 2, M_w7.8 April 25, 2015 main shock, V_{S30} = 1000 m/s, Set 2.

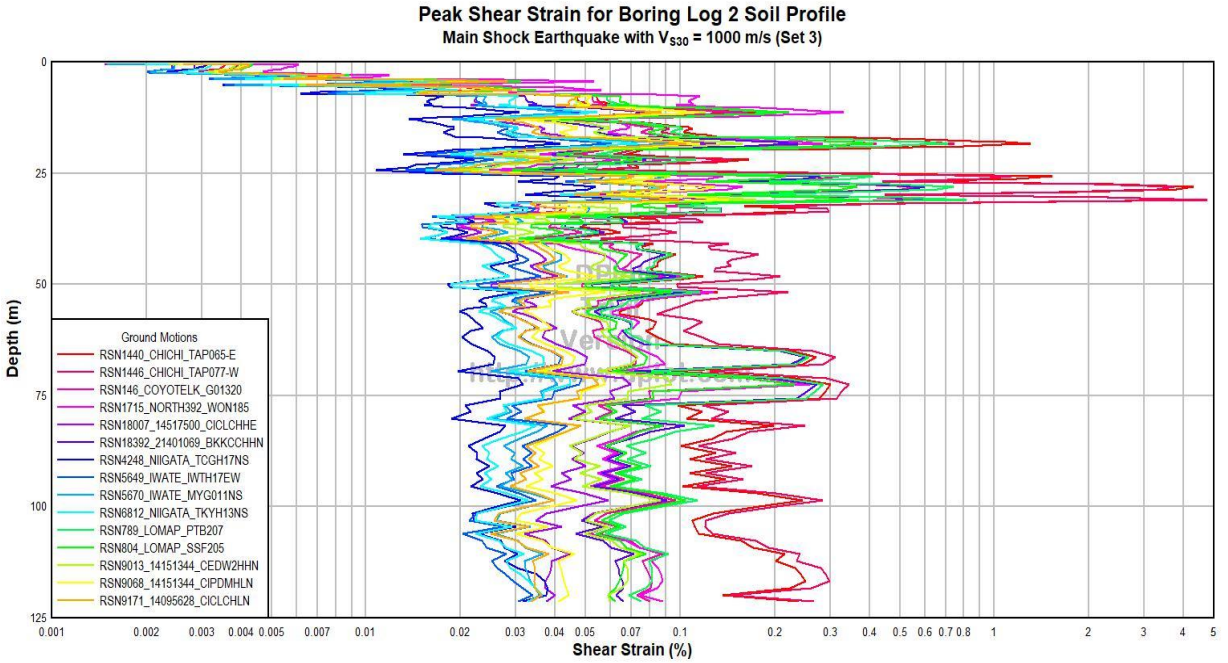

Figure D.3 Peak shear strain versus depth for Soil Profile 2, M_w7.8 April 25, 2015 main shock, V_{S30} = 1000 m/s, Set 3.

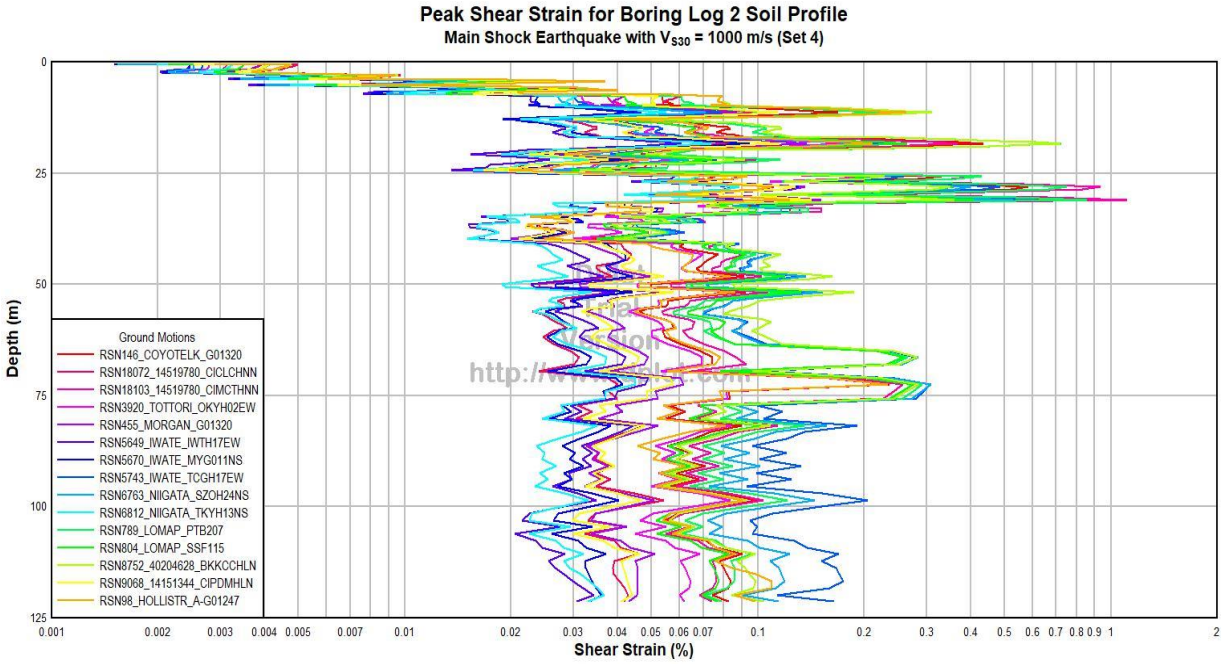

Figure D.4 Peak shear strain versus depth for Soil Profile 2, M_w7.8 April 25, 2015 main shock, V_{S30} = 1000 m/s, Set 4.

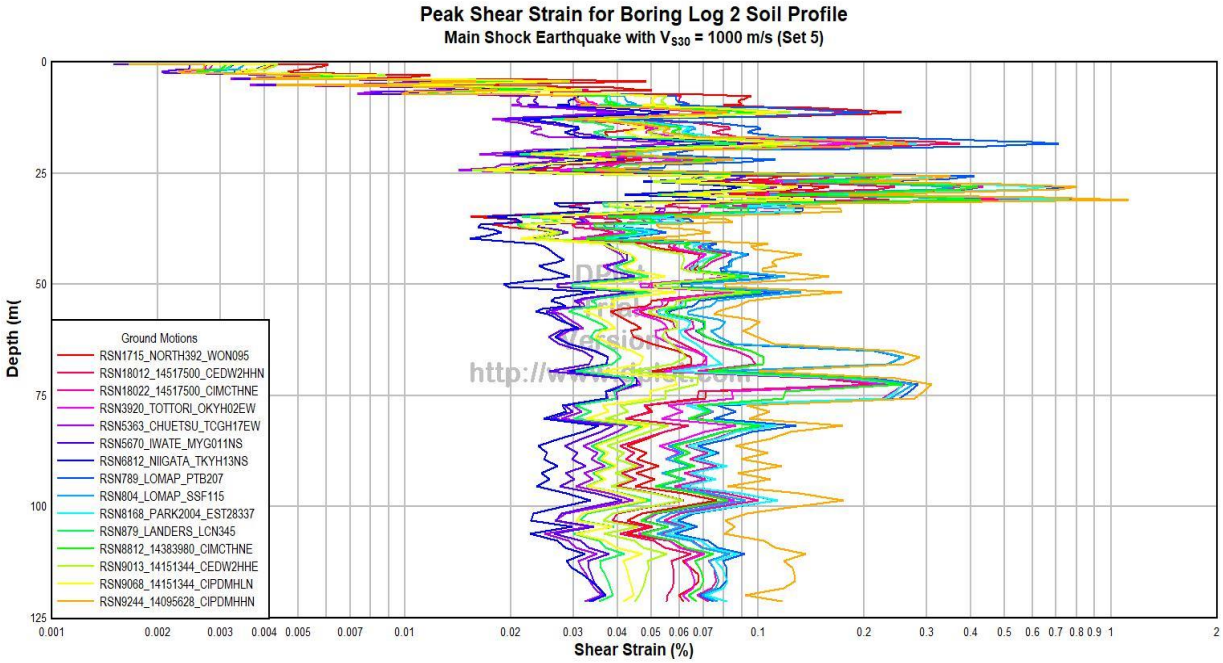

Figure D.5 Peak shear strain versus depth for Soil Profile 2, M_w7.8 April 25, 2015 main shock, V_{S30} = 1000 m/s, Set 5.

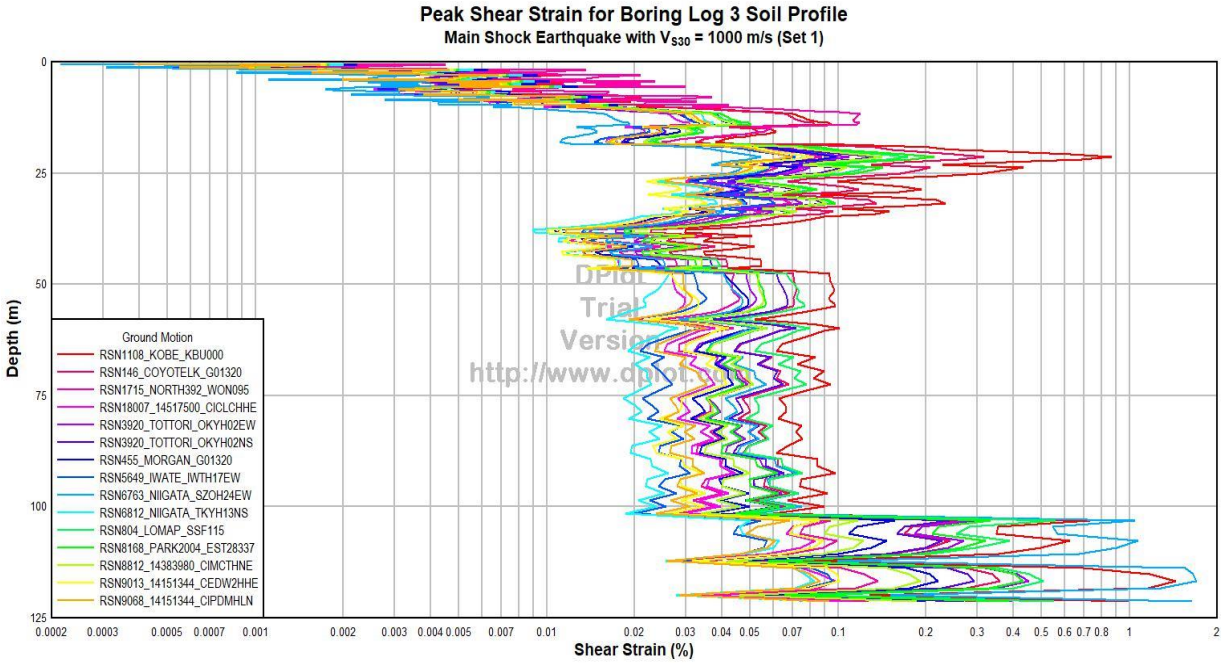

Figure D.6 Peak shear strain versus depth for Soil Profile 3, M_w7.8 April 25, 2015 main shock, V_{S30} = 1000 m/s, Set 1.

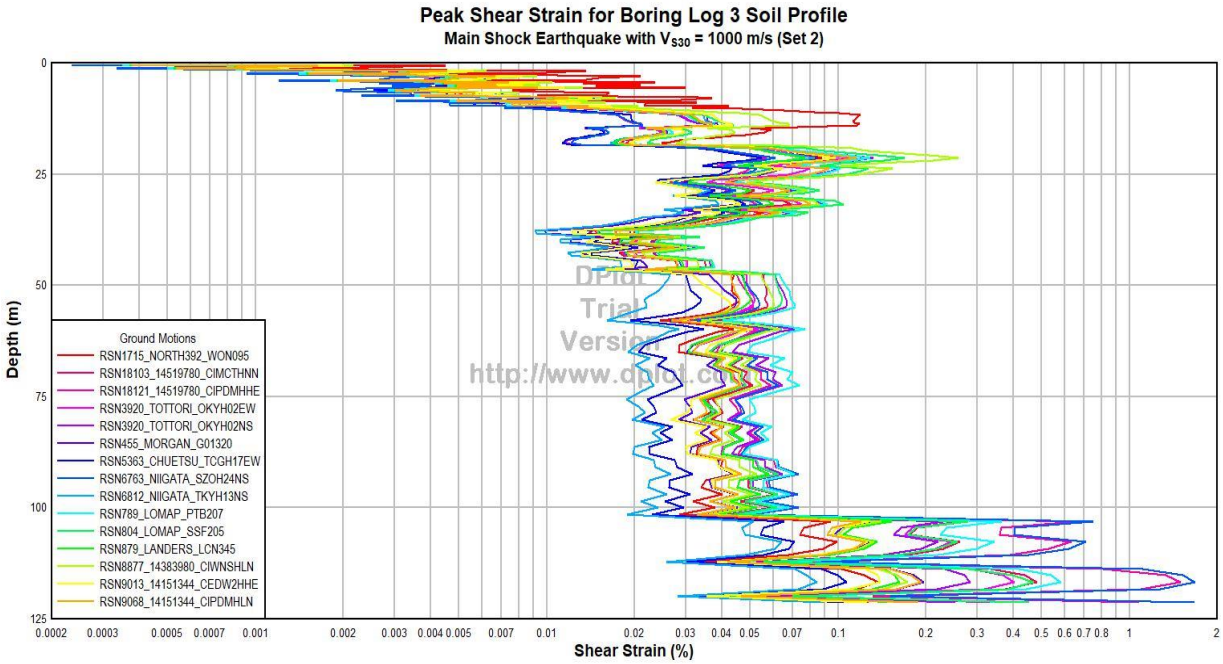

Figure D.7 Peak shear strain versus depth for Soil Profile 3, M_w7.8 April 25, 2015 main shock, V_{S30} = 1000 m/s, Set 2.

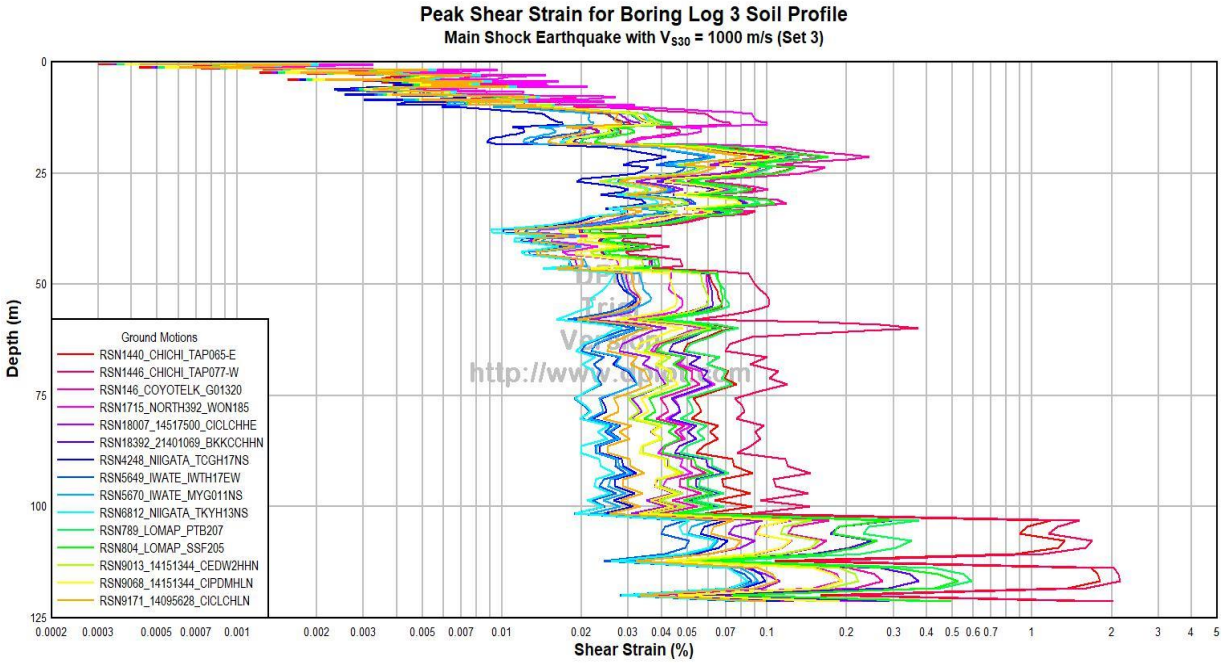

Figure D.8 Peak shear strain versus depth for Soil Profile 3, M_w7.8 April 25, 2015 main shock, V_{S30} = 1000 m/s, Set 3.

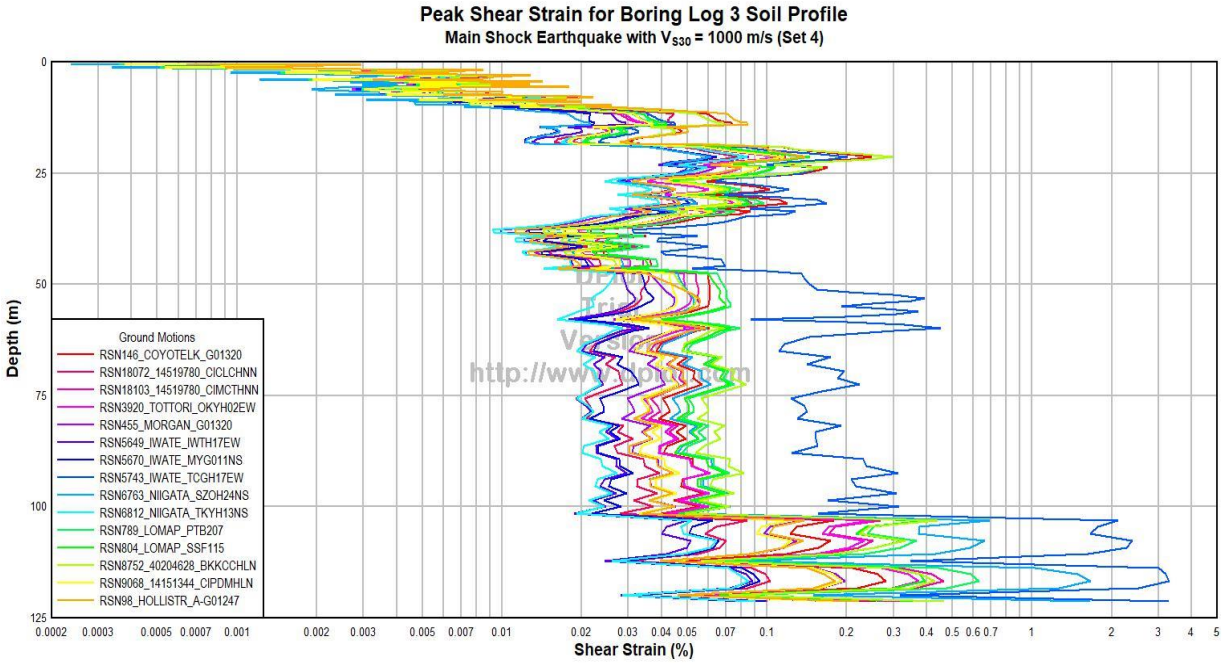

Figure D.9 Peak shear strain versus depth for Soil Profile 3, M_w7.8 April 25, 2015 main shock, V_{S30} = 1000 m/s, Set 4.

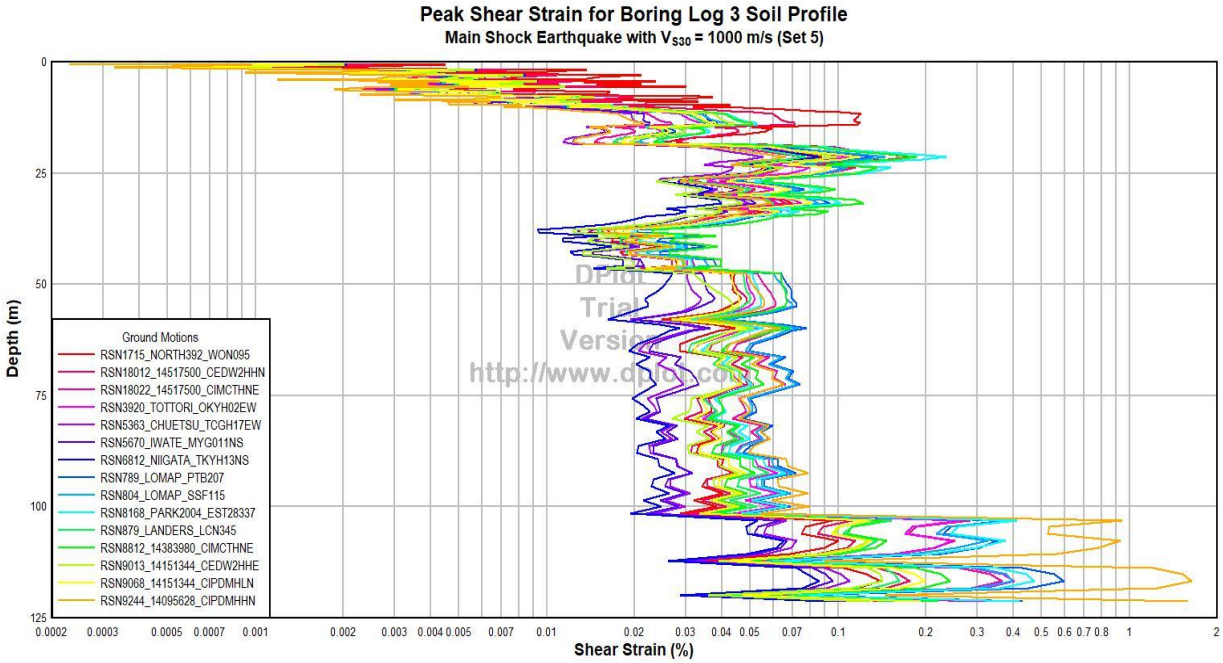

Figure D.10 Peak shear strain versus depth for Soil Profile 3, M_w7.8 April 25, 2015 main shock, V_{S30} = 1000 m/s, Set 5.

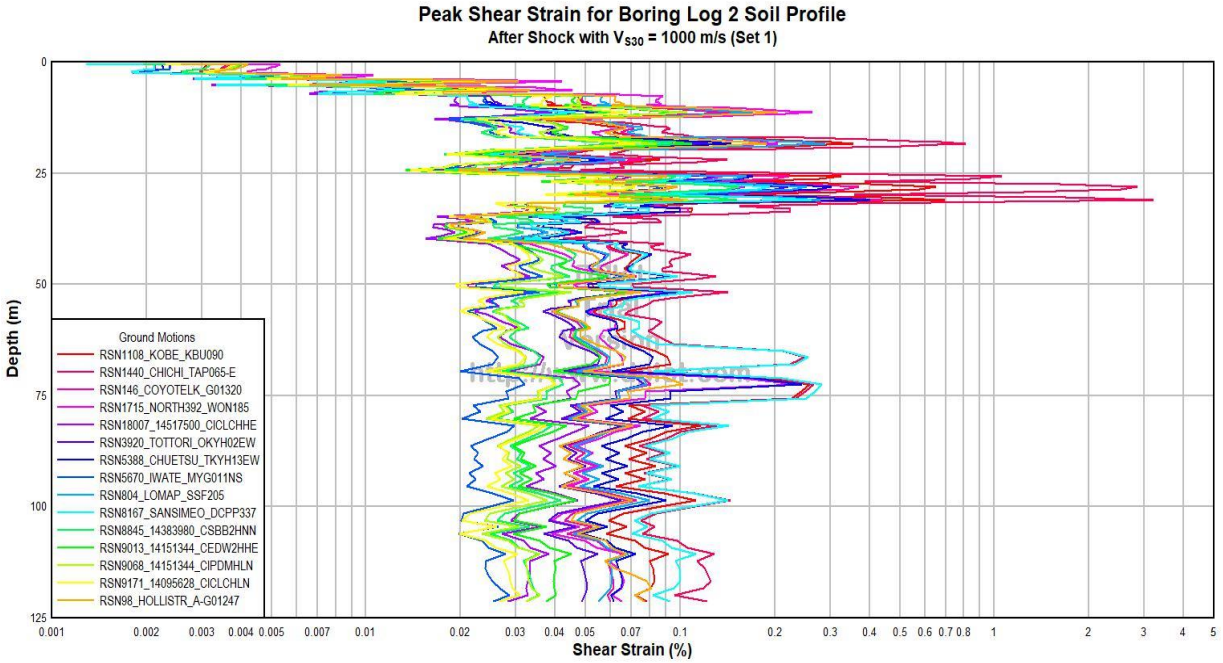

Figure D.11 Peak shear strain versus depth for Soil Profile 2, M_w7.3 May 12, 2015 aftershock, V_{S30} = 1000 m/s, Set 1.

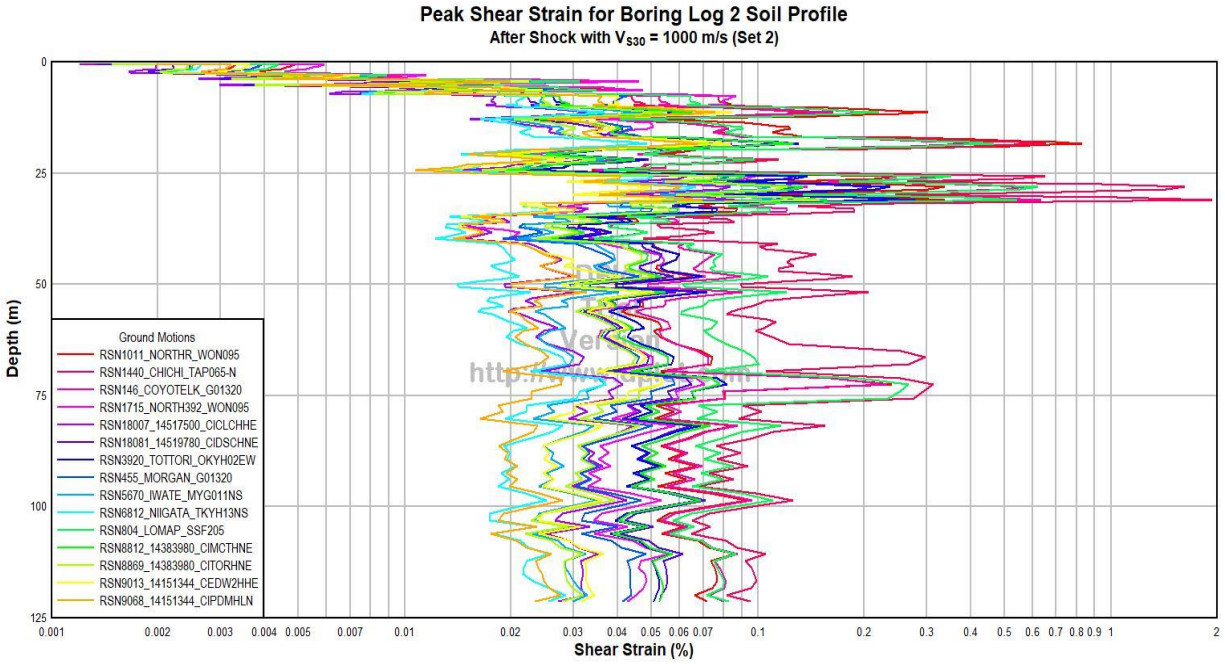

Figure D.12 Peak shear strain versus depth for Soil Profile 2, M_w7.3 May 12, 2015 aftershock, V_{S30} = 1000 m/s, Set 2.

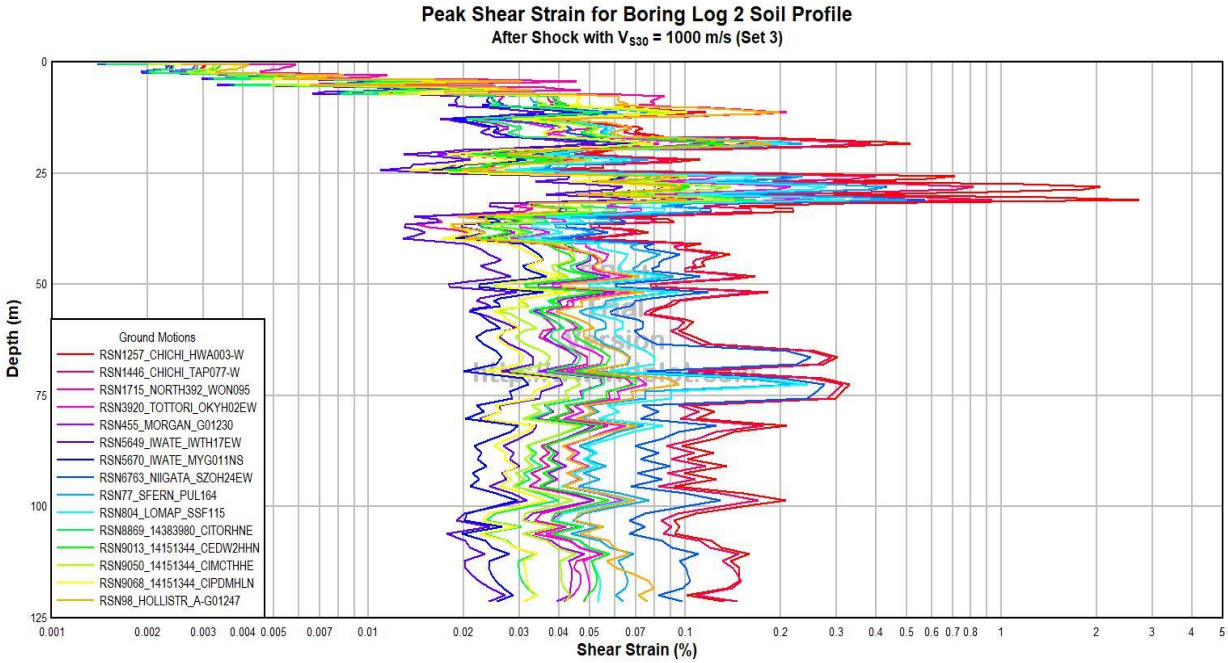

Figure D.13 Peak shear strain versus depth for Soil Profile 2, M_w7.3 May 12, 2015 aftershock, V_{S30} = 1000 m/s, Set 3.

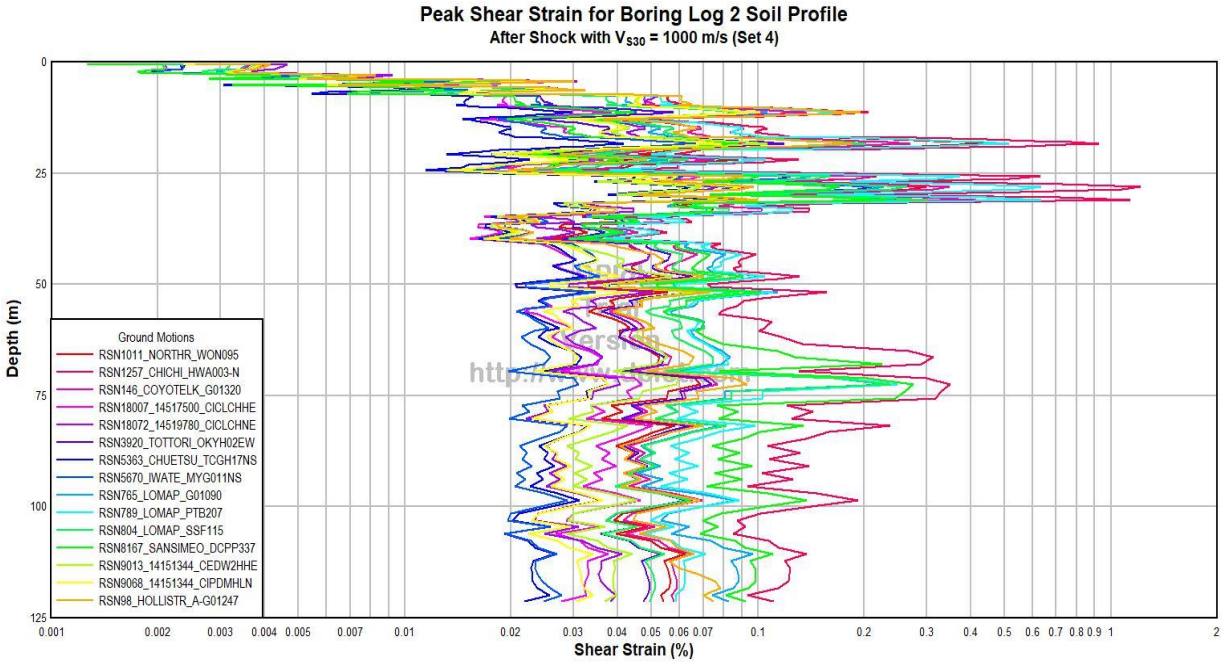

Figure D.14 Peak shear strain versus depth for Soil Profile 2, M_w7.3 May 12, 2015 aftershock, V_{S30} = 1000 m/s, Set 4.

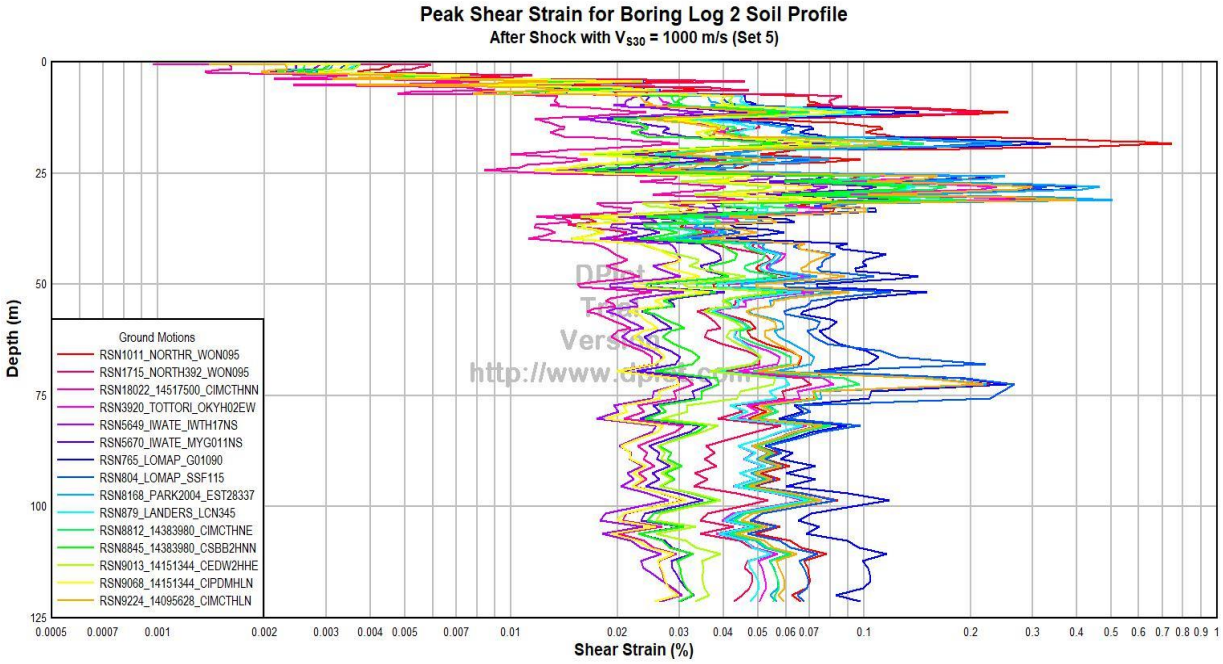

Figure D.15 Peak shear strain versus depth for Soil Profile 2, M_w7.3 May 12, 2015 aftershock, V_{S30} = 1000 m/s, Set 5.

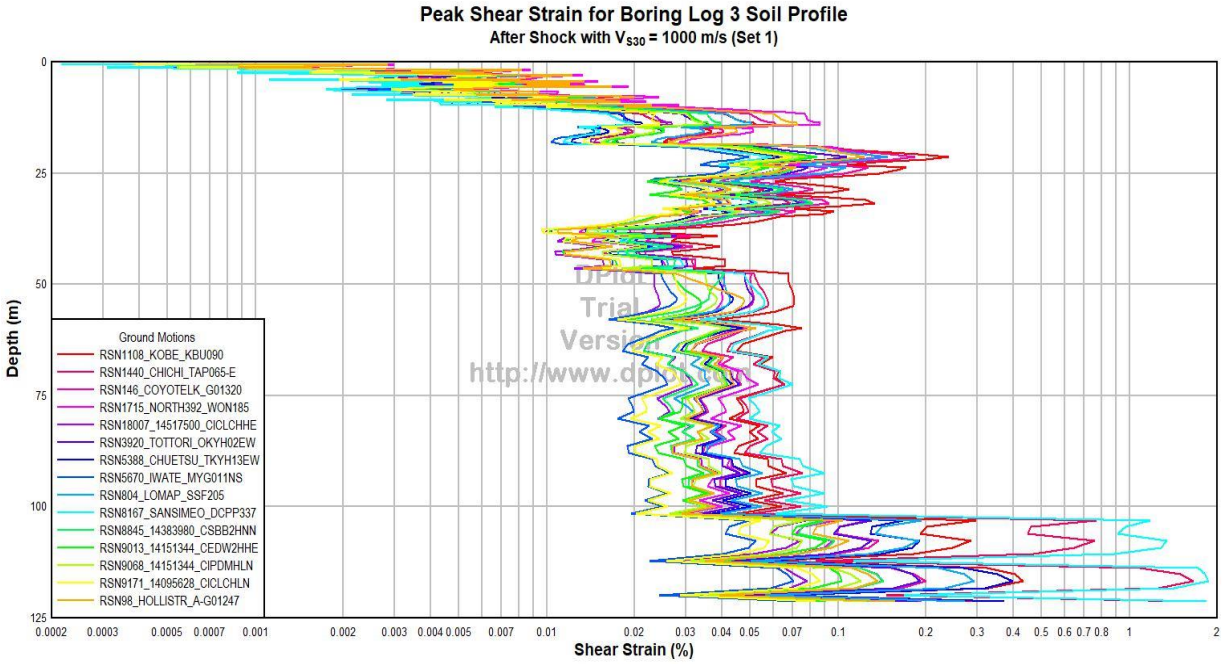

Figure D.16 Peak shear strain versus depth for Soil Profile 3, M_w7.3 May 12, 2015 aftershock, V_{S30} = 1000 m/s, Set 1.

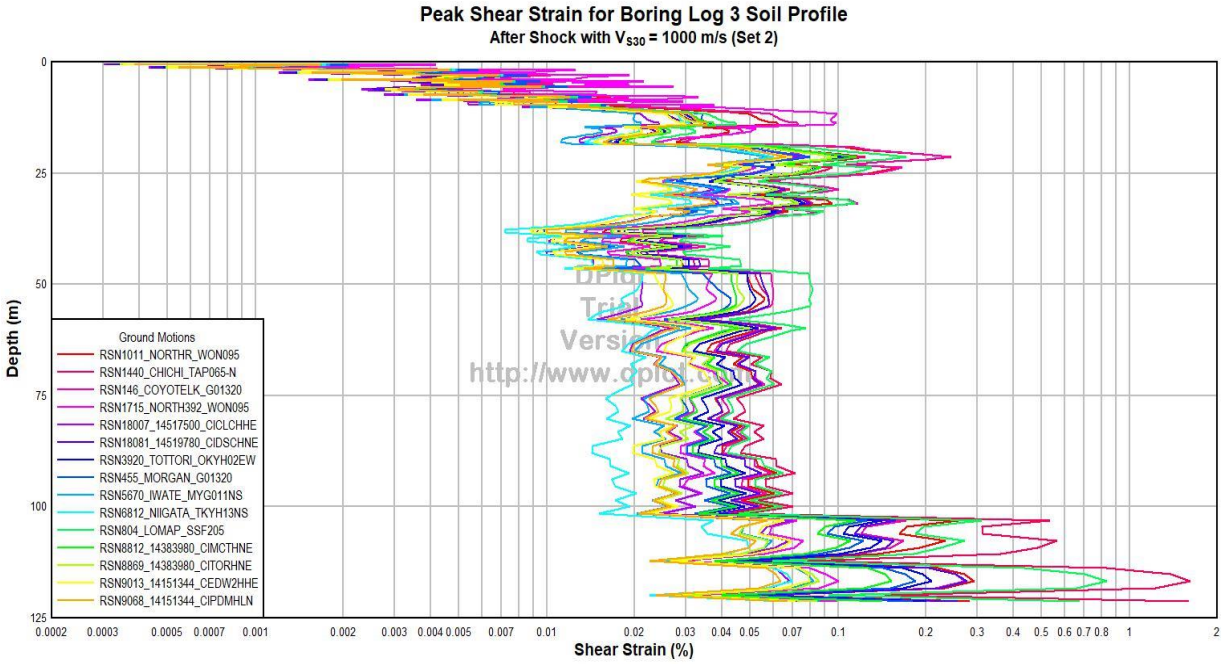

Figure D.17 Peak shear strain versus depth for Soil Profile 3, M_w7.3 May 12, 2015 aftershock, V_{S30} = 1000 m/s, Set 2.

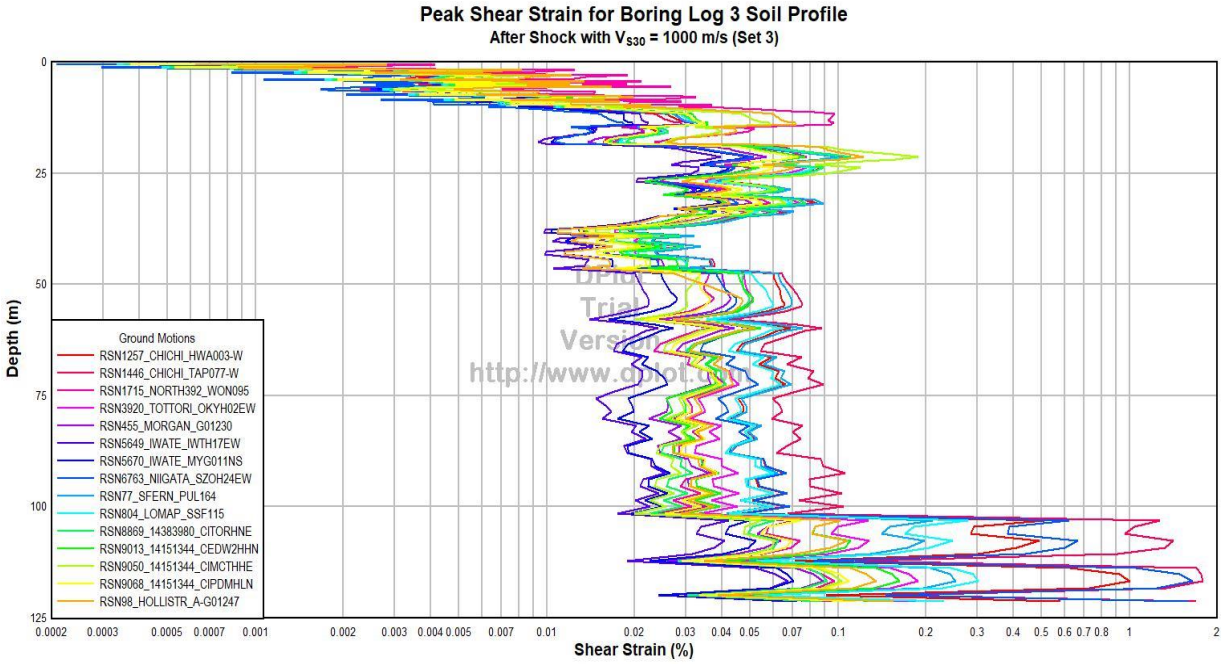

Figure D.18 Peak shear strain versus depth for Soil Profile 3, M_w7.3 May 12, 2015 aftershock, V_{S30} = 1000 m/s, Set 3.

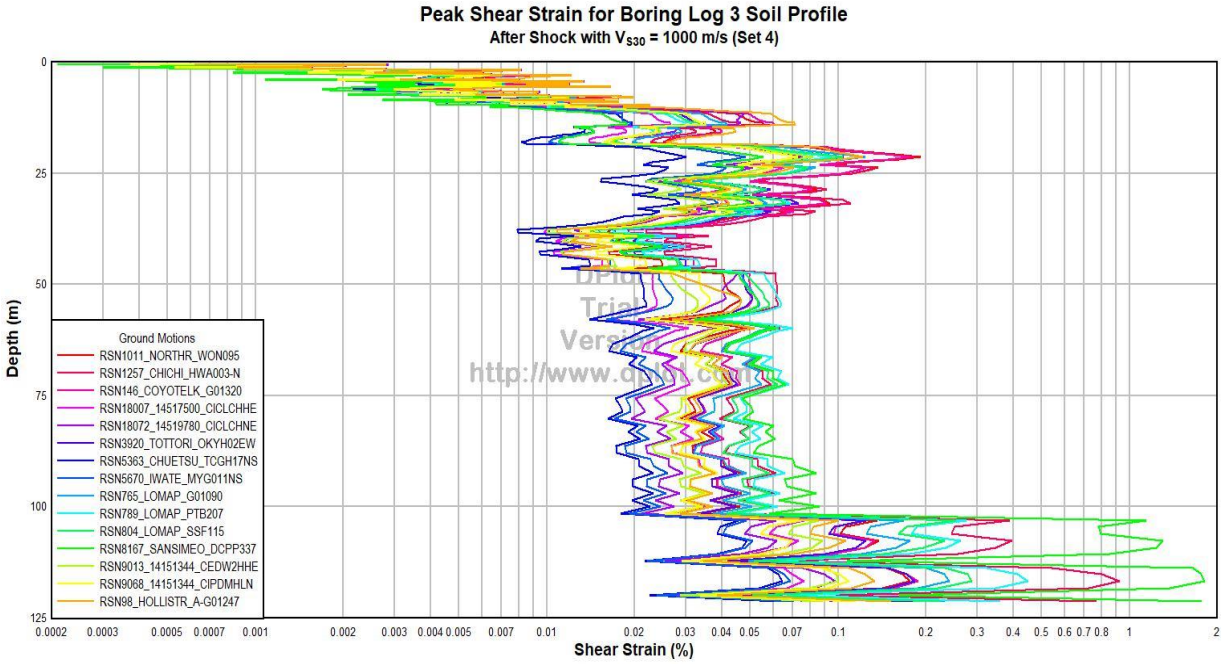

Figure D.19 Peak shear strain versus depth for Soil Profile 3, M_w7.3 May 12, 2015 aftershock, V_{S30} = 1000 m/s, Set 4.

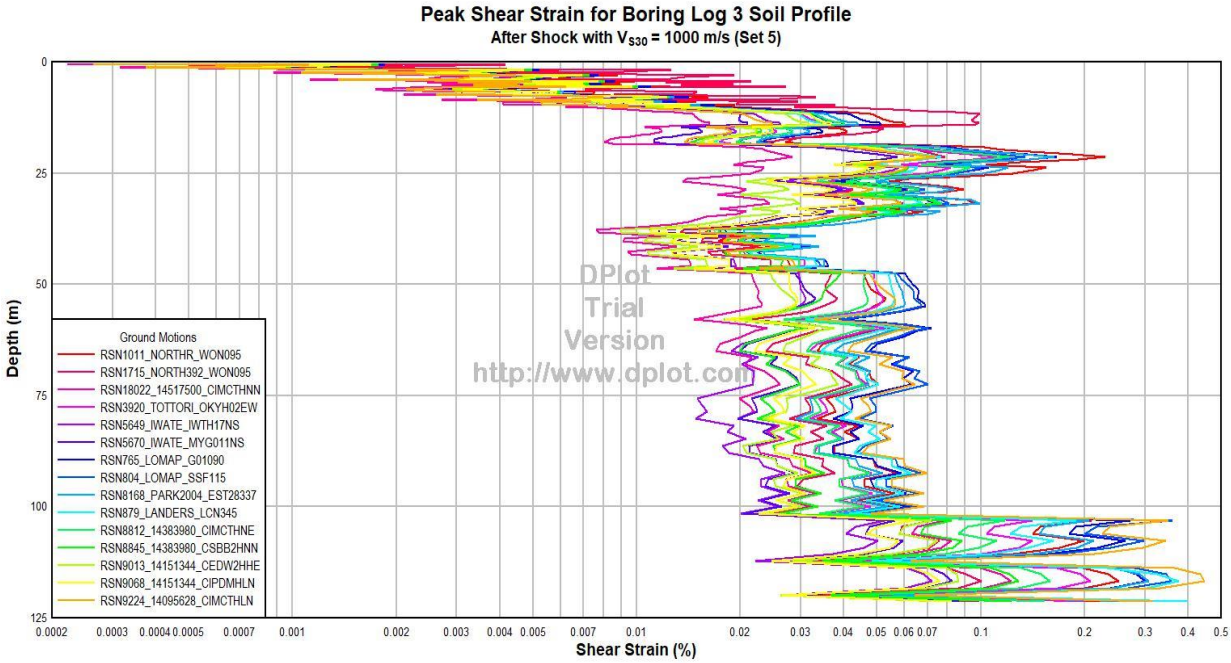

Figure D.20 Peak shear strain versus depth for Soil Profile 3, M_w7.3 May 12, 2015 aftershock, V_{S30} = 1000 m/s, Set 5.

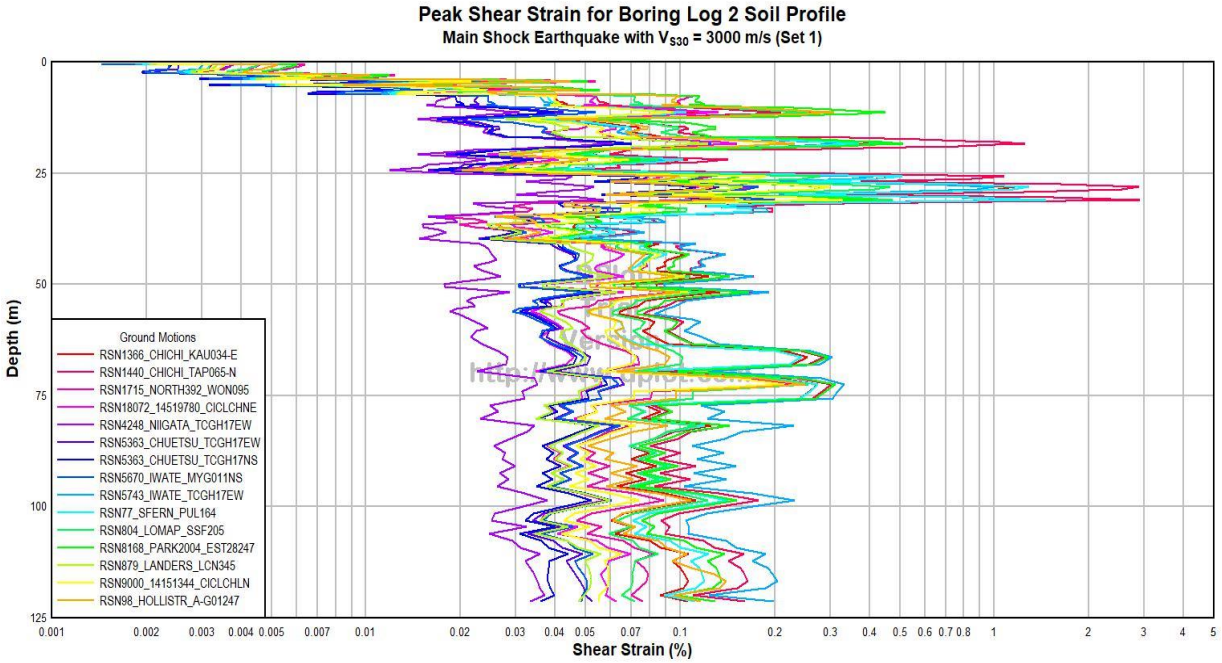

Figure D.21 Peak shear strain versus depth for Soil Profile 2, M_w7.8 April 25, 2015 main shock, V_{S30} = 3000 m/s, Set 1.

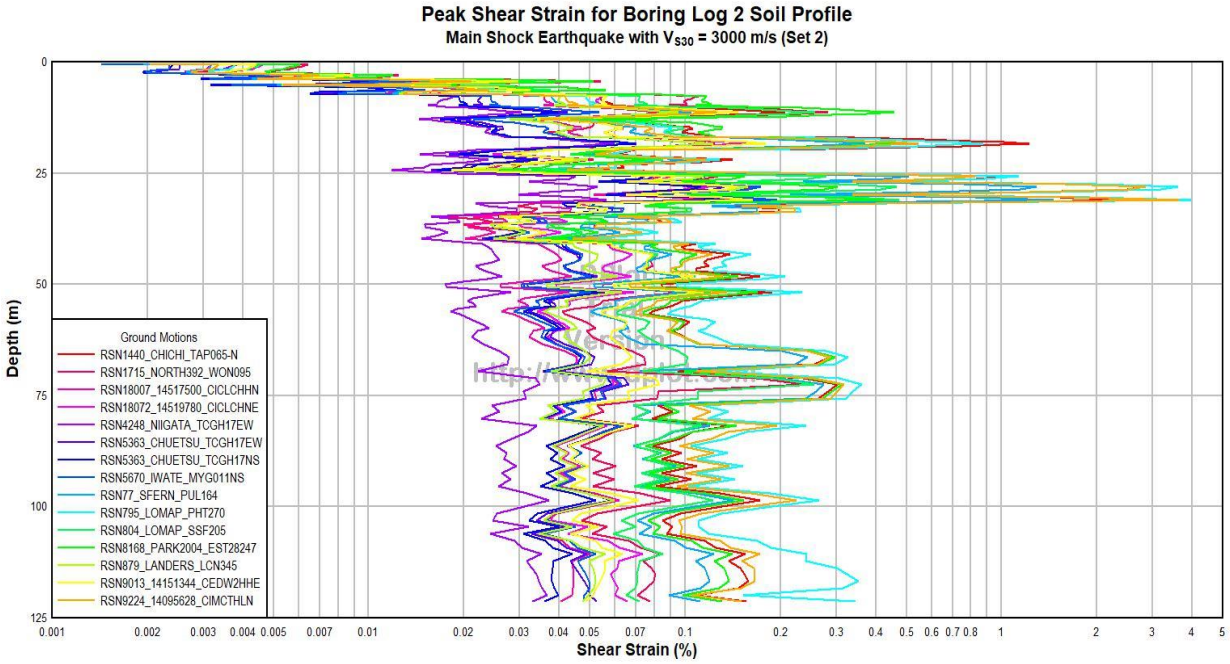

Figure D.22 Peak shear strain versus depth for Soil Profile 2, M_w7.8 April 25, 2015 main shock, V_{S30} = 3000 m/s, Set 2.

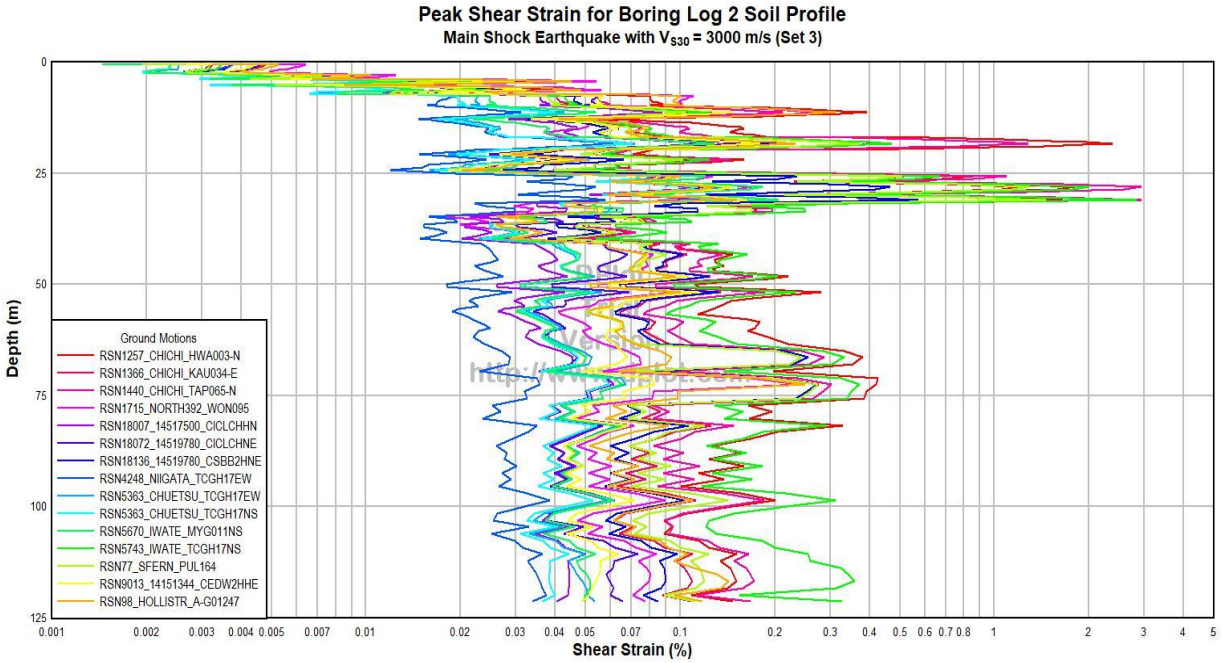

Figure D.23 Peak shear strain versus depth for Soil Profile 2, M_w7.8 April 25, 2015 main shock, V_{S30} = 3000 m/s, Set 3.

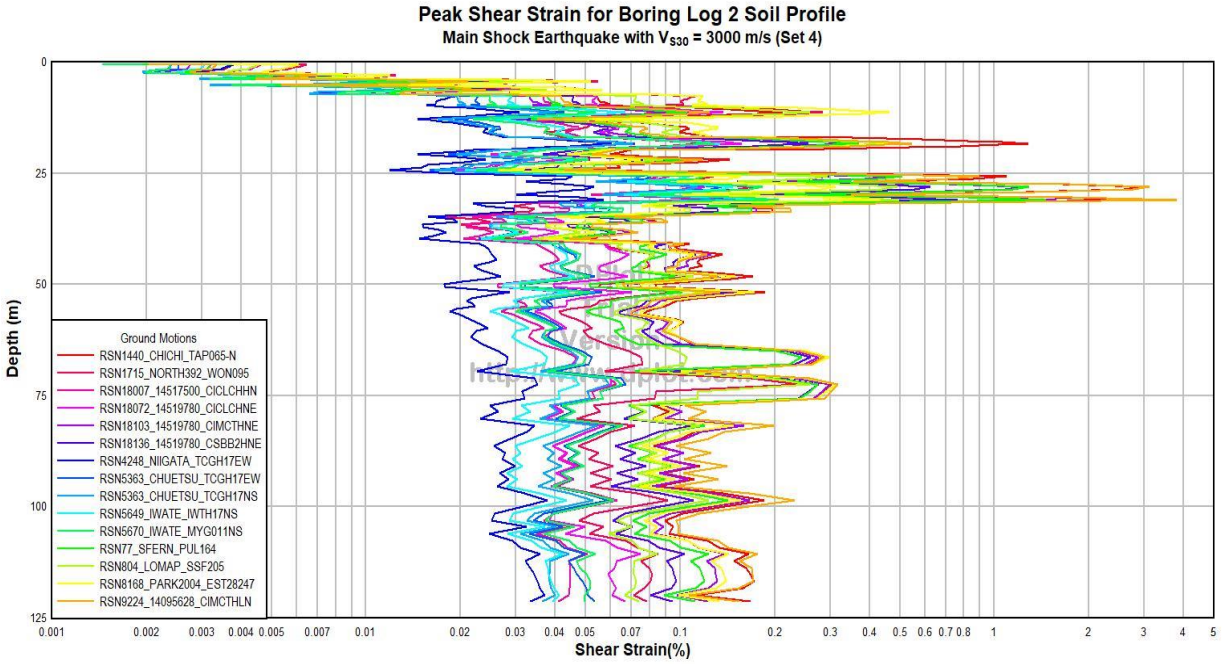

Figure D.24 Peak shear strain versus depth for Soil Profile 2, M_w7.8 April 25, 2015 main shock, V_{S30} = 3000 m/s, Set 4.

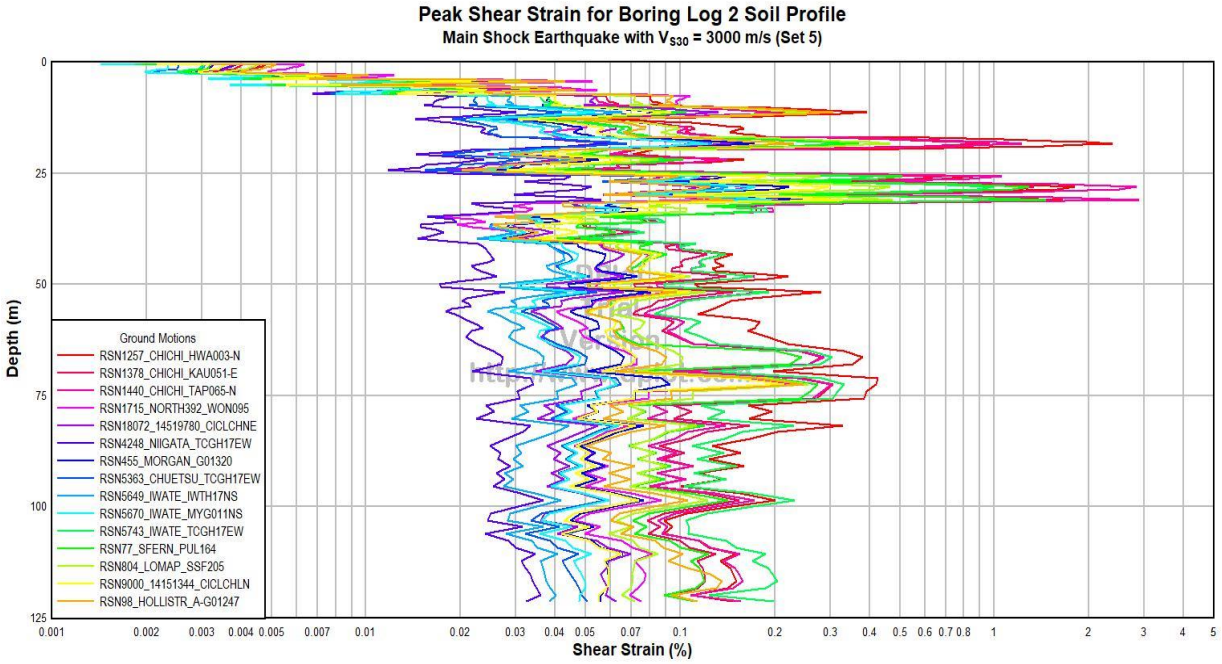

Figure D.25 Peak shear strain versus depth for Soil Profile 2, M_w7.8 April 25, 2015 main shock, V_{S30} = 3000 m/s, Set 5.

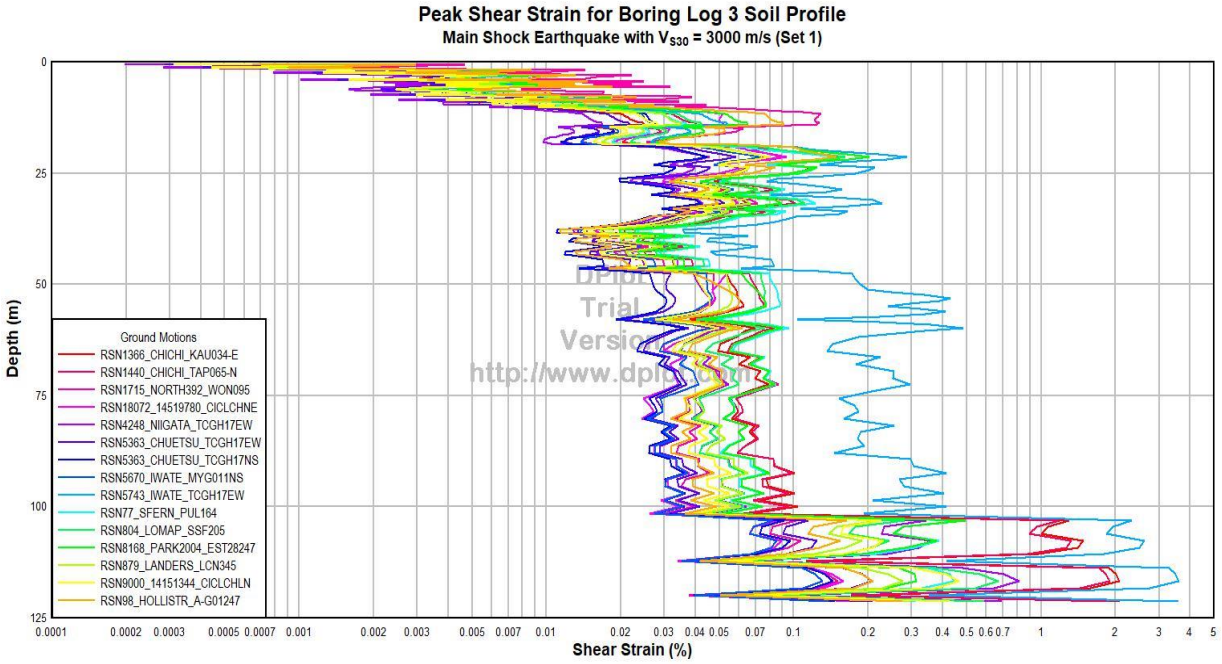

Figure D.26 Peak shear strain versus depth for Soil Profile 3, M_w7.8 April 25, 2015 main shock, V_{S30} = 3000 m/s, Set 1.

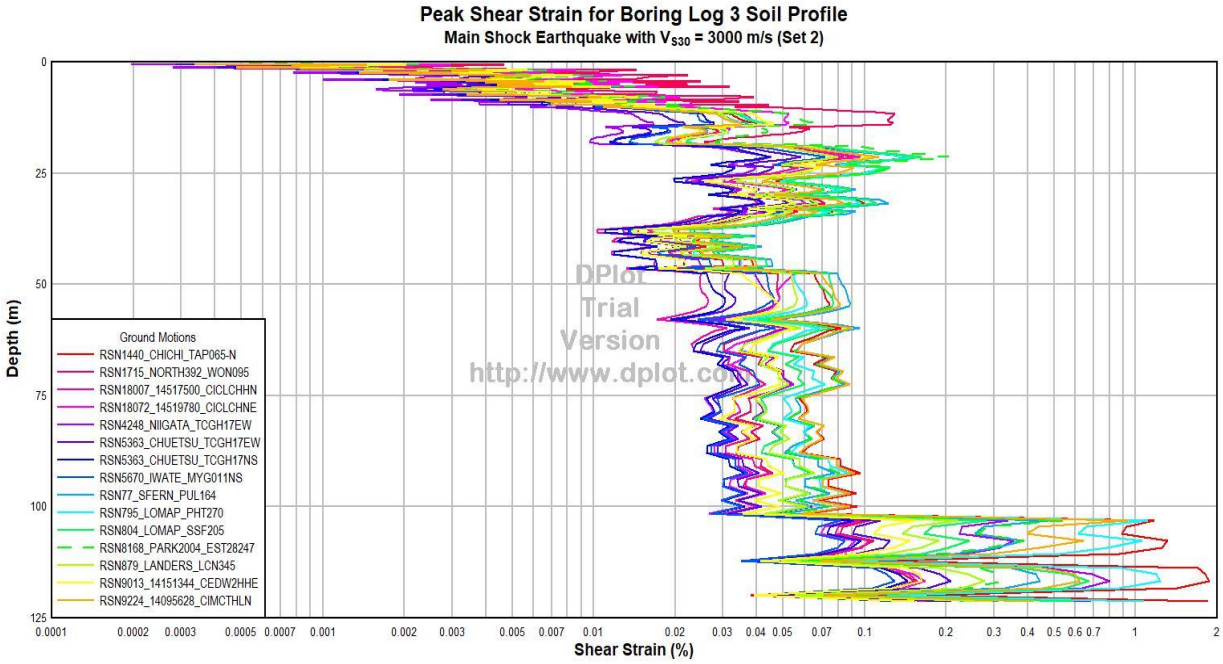

Figure D.27 Peak shear strain versus depth for Soil Profile 3, M_w7.8 April 25, 2015 main shock, V_{S30} = 3000 m/s, Set 2.

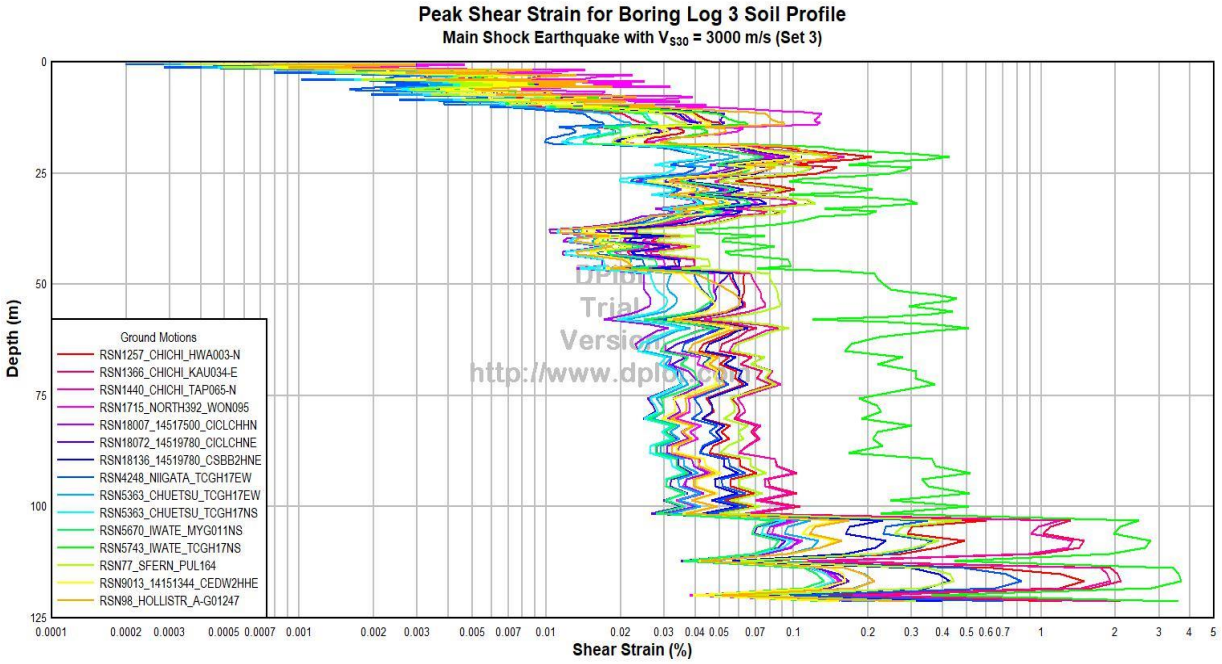

Figure D.28 Peak shear strain versus depth for Soil Profile 3, M_w7.8 April 25, 2015 main shock, V_{S30} = 3000 m/s, Set 3.

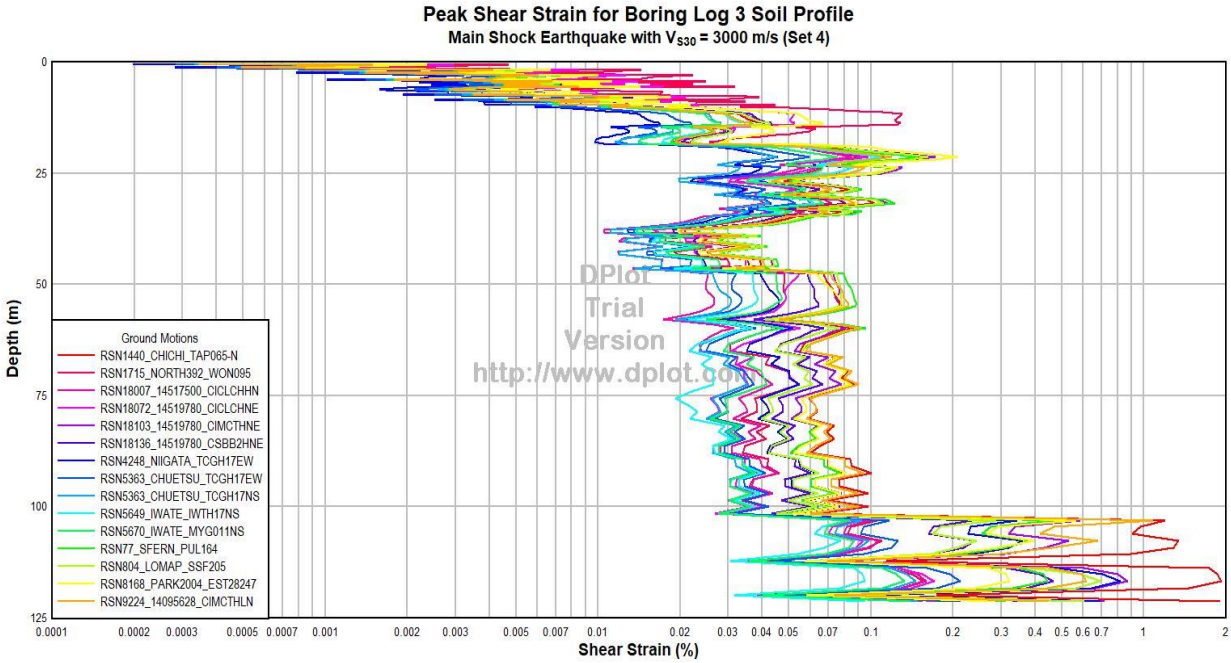

Figure D.29 Peak shear strain versus depth for Soil Profile 3, M_w7.8 April 25, 2015 main shock, V_{S30} = 3000 m/s, Set 4.

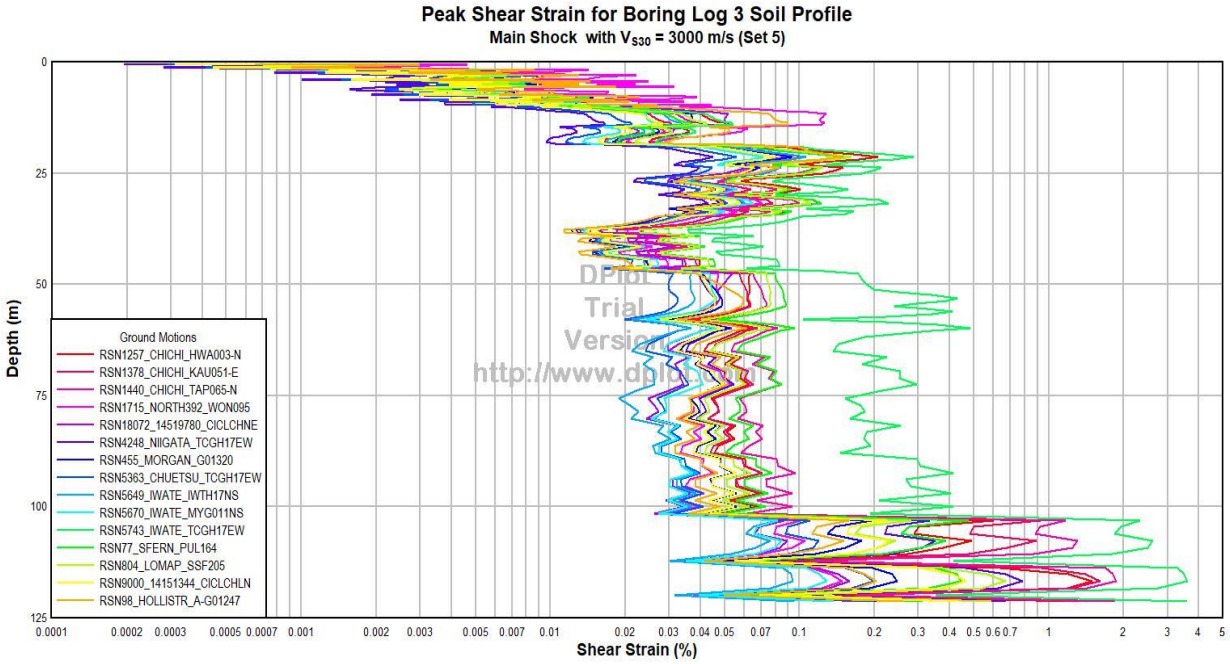

Figure D.30 Peak shear strain versus depth for Soil Profile 3, M_w7.8 April 25, 2015 main shock, V_{S30} = 3000 m/s, Set 5.

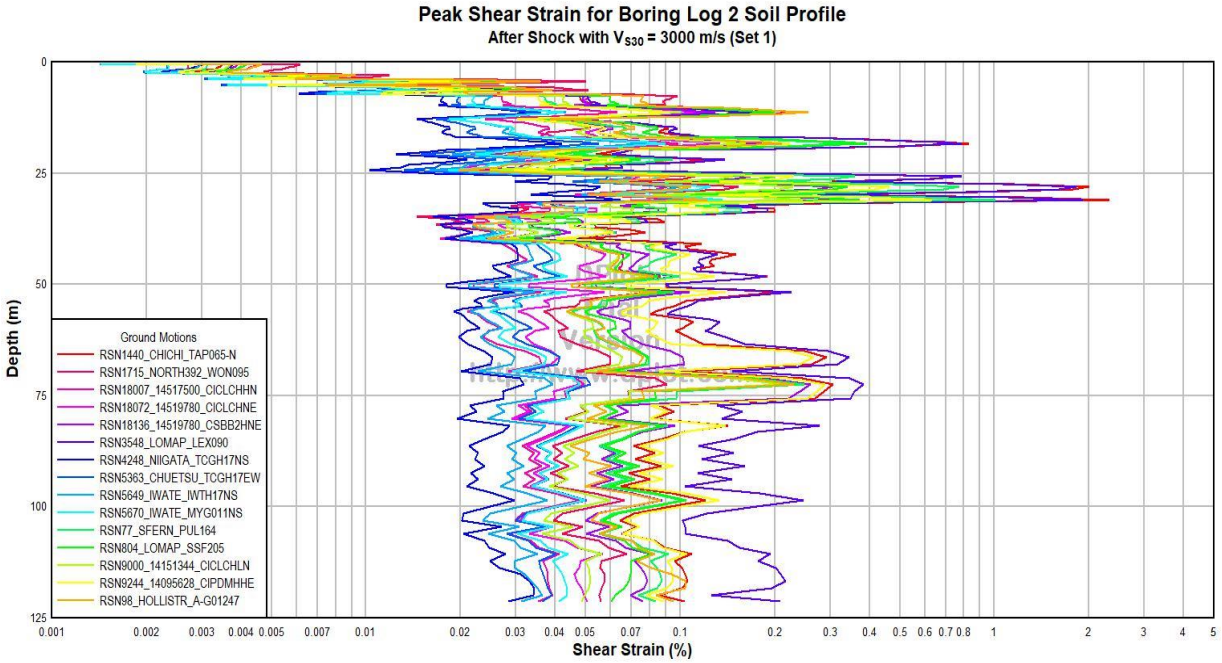

Figure D.31 Peak shear strain versus depth for Soil Profile 2, M_w7.3 May 12, 2015 aftershock, V_{S30} = 3000 m/s, Set 1.

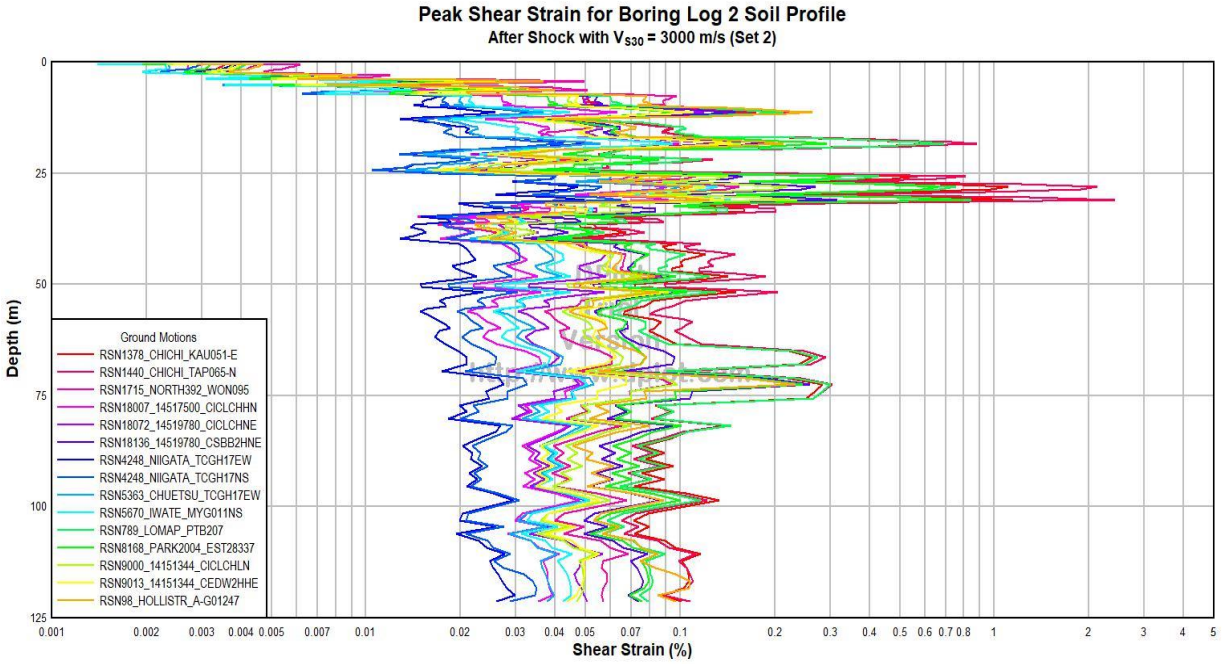

Figure D.32 Peak shear strain versus depth for Soil Profile 2, M_w7.3 May 12, 2015 aftershock, V_{S30} = 3000 m/s, Set 2.

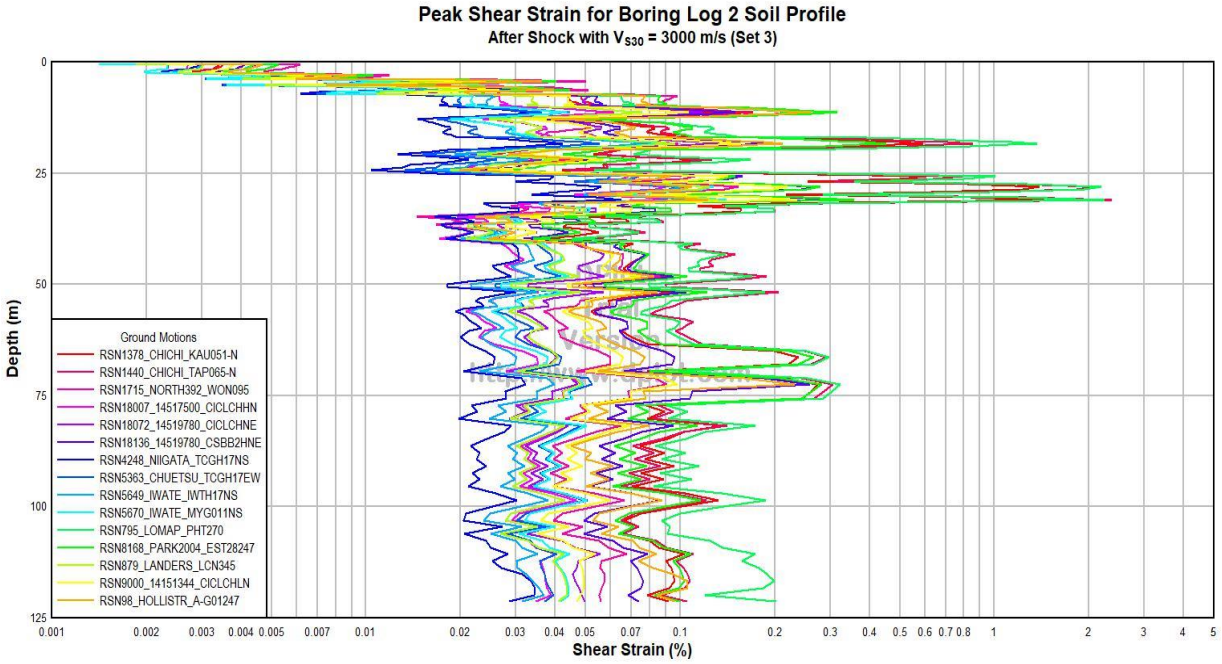

Figure D.33 Peak shear strain versus depth for Soil Profile 2, M_w7.3 May 12, 2015 aftershock, V_{S30} = 3000 m/s, Set 3.

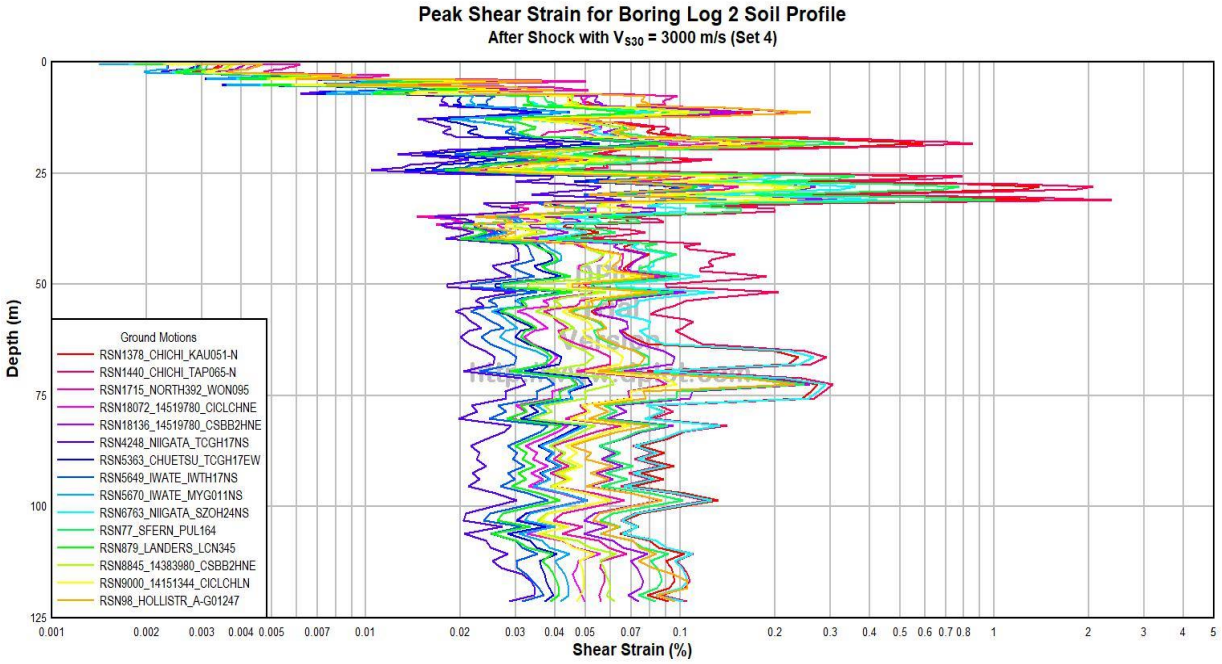

Figure D.34 Peak shear strain versus depth for Soil Profile 2, M_w7.3 May 12, 2015 aftershock, V_{S30} = 3000 m/s, Set 4.

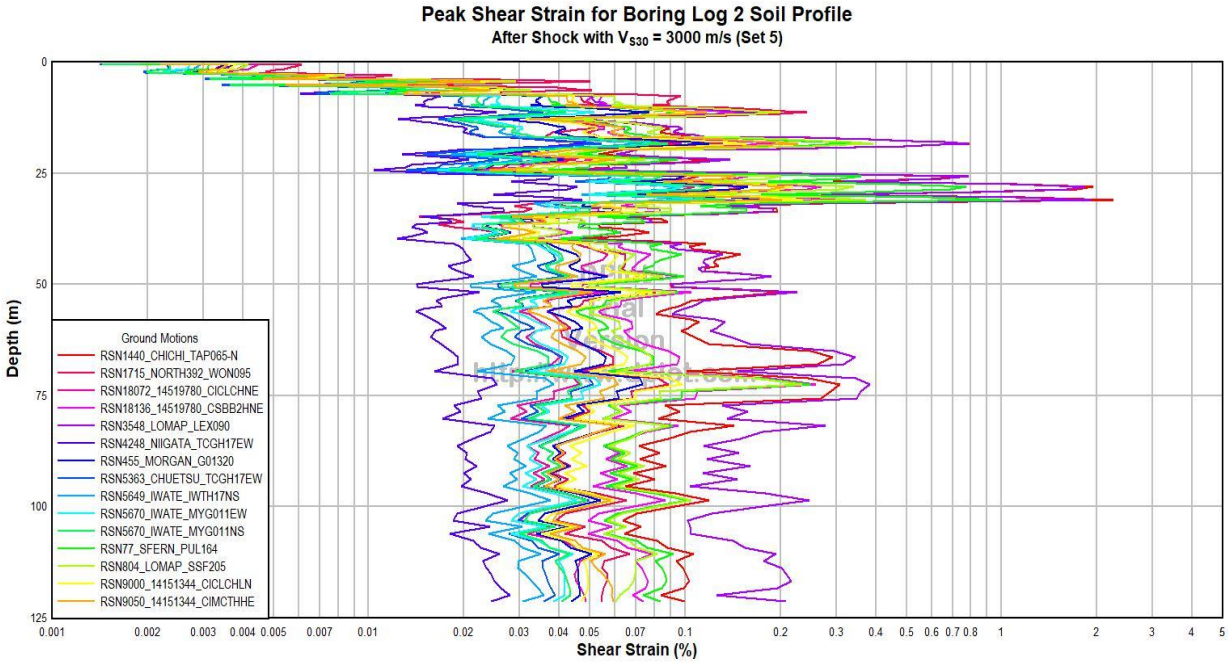

Figure D.35 Peak shear strain versus depth for Soil Profile 2, M_w7.3 May 12, 2015 aftershock, V_{S30} = 3000 m/s, Set 5.

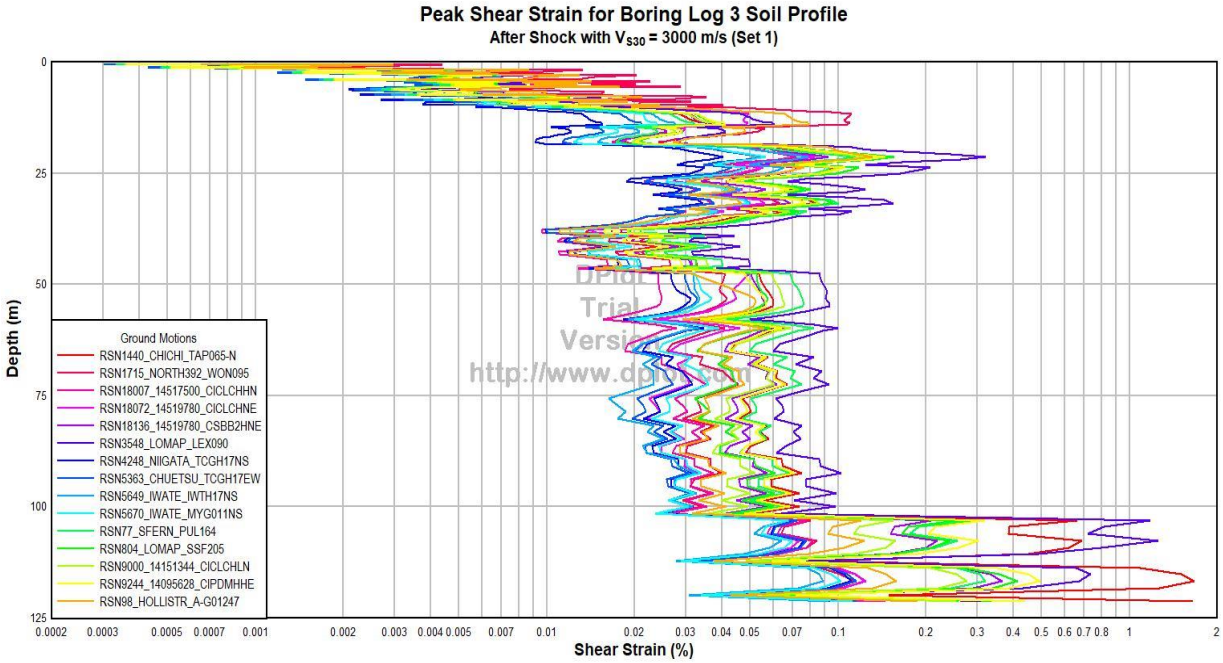

Figure D.36 Peak shear strain versus depth for Soil Profile 3, M_w7.3 May 12, 2015 aftershock, V_{S30} = 3000 m/s, Set 1.

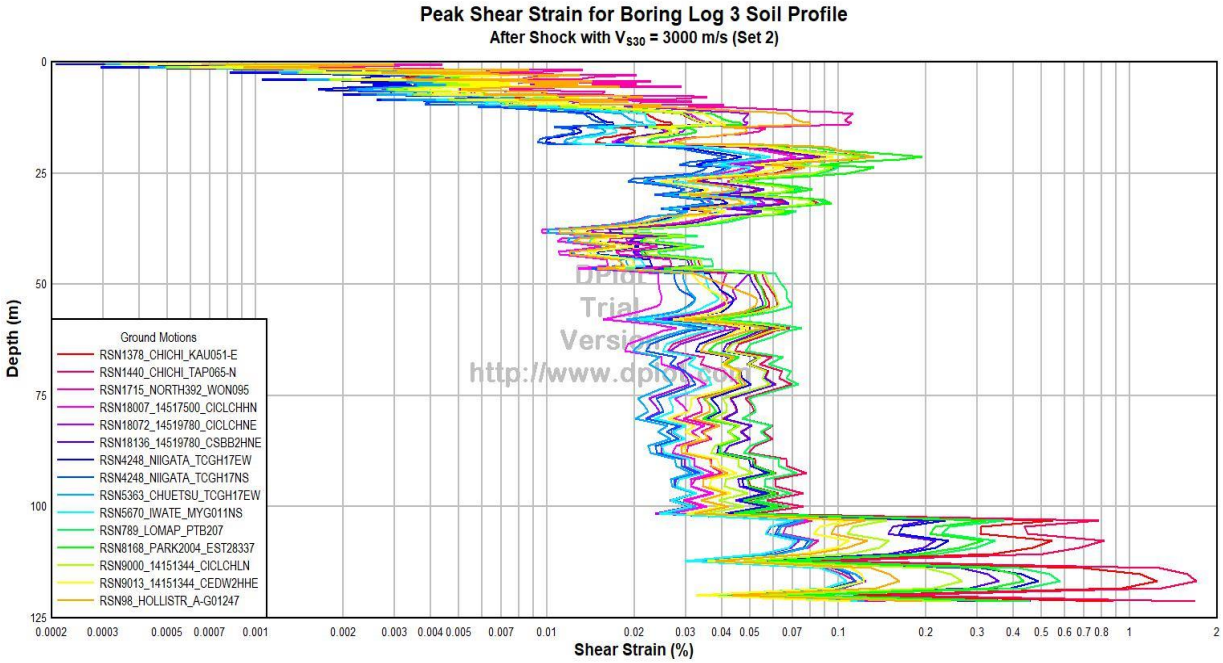

Figure D.37 Peak shear strain versus depth for Soil Profile 3, M_w7.3 May 12, 2015 aftershock, V_{S30} = 3000 m/s, Set 2.

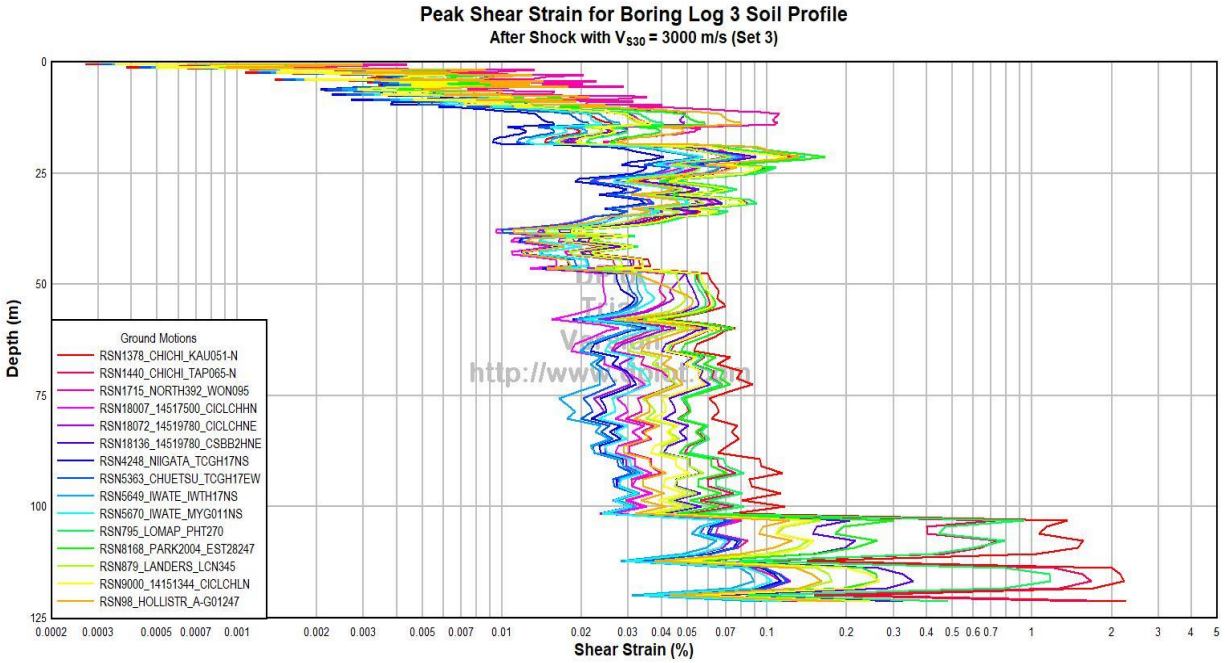

Figure D.38 Peak shear strain versus depth for Soil Profile 3, M_w7.3 May 12, 2015 aftershock, V_{S30} = 3000 m/s, Set 3.

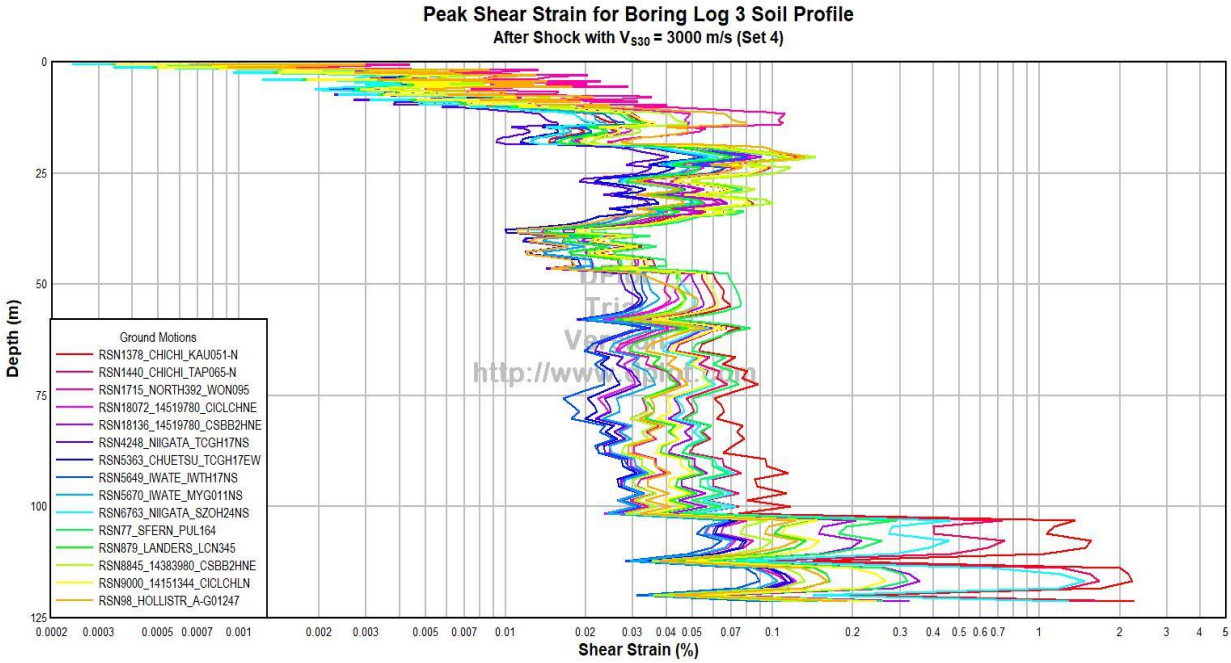

Figure D.39 Peak shear strain versus depth for Soil Profile 3, M_w7.3 May 12, 2015 aftershock, V_{S30} = 3000 m/s, Set 4.

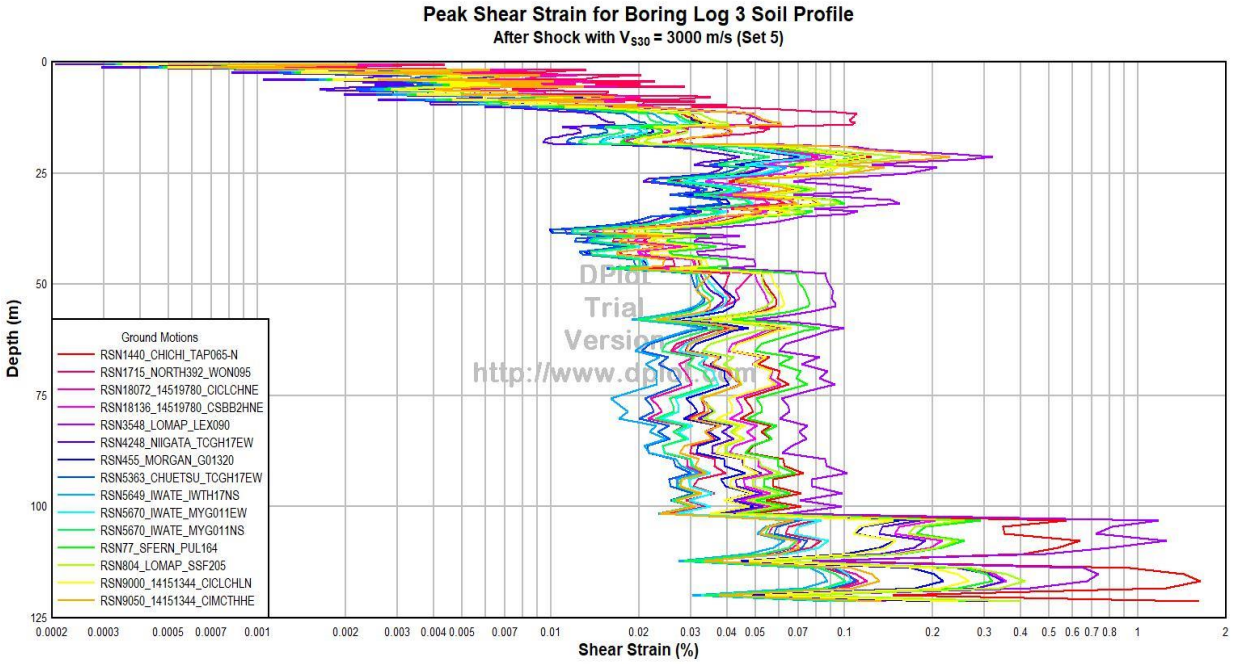

Figure D.40 Peak shear strain versus depth for Soil Profile 3, M_w7.3 May 12, 2015 aftershock, V_{S30} = 3000 m/s, Set 5.

APPENDIX E: MATLAB code used to compute seismic compression

The code used to compute seismic compression is below. Input parameters were read from an Excel spreadsheet that contained the parameters per soil profile, and each sheet is included in table form in this appendix. This code was used for both analyses.

```
%%Seismic Compression Code
clear all
%% Bring in soil profile parameters
N=readmatrix('Soil Profile','Sheet','Profile_3','Range','C2:C110').'; %N1,60
value for each soil layer in profile (minus clay layers)
FC=readmatrix('Soil Profile','Sheet','Profile_3','Range','D2:D110'); %Fines
content in % for each soil layer in profile (minus clay layers)
sigma=readmatrix('Soil Profile','Sheet','Profile_3','Range','G2:G110'); %
Effective confining stress in kPa for each soil layer in profile (minus clay)
Thickness=readmatrix('Soil Profile','Sheet','Profile_3','Range','K2:K110');
%Thickness of soil layer
C_d=readmatrix('Soil Profile','Sheet','Profile_3','Range','L2:L110').'; %Soil
specific parameter assumed to be 55 for now according to Skempton (1986)
C_2=readmatrix('Soil Profile','Sheet','Profile_3','Range','M2:M110').'; %1D-2D
scaling factor
atm=101.325; %Atmospheric pressure
y_tv=0.01; %threshold strain in %
%% Read shear strain time histories
d=dir('*.csv');
n=length(d);
for z=1:n
    D(z)=100*sqrt(N(z)/C_d(z)); % Relative density calculation
    Dr(z)=D(z);
end
for f=1:n
    if Dr(f)>100
        Dr(f)=100;
    else
        Dr(f)=Dr(f);
    end
end
for i=1:n
    data(i,:)=readmatrix(d(i).name,'Range','B4:B3203'); %Number of points in
the shear strain time history
    nam = d(i).name;
    for j = 1:length(nam)
        test(j) = str2double(nam(1:j));
        if isnan(test(j))
            val(i) = test(j-1);
            break
        end
    end
end
data1 = [val' data];
datas1 = sortrows(data1);
data_s = datas1(:,2:end);

for k=1:n
    indices=find(data_s(k,(2:end)).*data_s(k,(1:end-
1))<0);find(abs(data_s(k,:))<1e-07); %find the max point between two zero
crossings
    M2(k,1:length(indices))=indices;
end
%% Compute Seismic Compression
maxes2=zeros(n,110);
```

```
e_vi=0;
e_v=zeros(n,length(indices)-1);
 for count=1:n
     nmax=length(find(M2(count,:)))-1;
 for ii=1:nmax
      maxes(ii)=(max(abs(data_s(count,(M2(count,ii):M2(count,ii+1))))));
      maxes2(count,1:length(maxes))=maxes;
 end
 maxes=zeros(1,nmax);
 for j=1:length(maxes2)
     if maxes2(count,j)~=0
     F_p=2.149*(maxes2(count,j)^-0.2343)+4.337*exp(-66.56*maxes2(count,j));
     F(count,j)=F_p;
     KFC=exp(-0.042*(FC(count,:)-10));
     KFC_1(count)=KFC;
     KS=1;
     K_sigma(count)=(sigma(count)/atm)^-0.29;
     a=5.38*exp(-0.023*Dr(count));
     a1(count)=a;
     C1(count,j)=(1/(F(count,j))*KFC_1(count)*KS*K_sigma(count)*a1(count));
     if maxes2(count,j)>0.01
     P(count,j)=exp(0.405)*(maxes2(count,j)-y_tv)^0.3291;
     else P(count,j)=0;
     end
     C2(count,j)=P(count,j)/C1(count,j);
     C3=1.2;
     if maxes2(count,j)>0.01
          e_v(count,j)=0.5*((maxes2(count,j)-y_tv)^C3)*C1(count,j)*exp(-
C2(count,j)*(e_vi/((maxes2(count,j)-y_tv)^C3)));
          e_vi=e_v(count,j)+e_vi;
          h(count)=e_vi;
    else
         e_v(count,j)=0;
         e_vi=e_v(count,j)+e_vi;
         h(count)=e_vi;
     end
x(count)=h(count);
     end
Comp(count)=((x(count)/100)*Thickness(count))*C_2(count);
 end
e_vi=0;
end
SC=sum(Comp) %Total Seismic compression for the whole soil profile
SC_2=Comp(32)+Comp(33)+Comp(34)+Comp(35)+Comp(41)+Comp(42)+Comp(43)+Comp(44)+Co
mp(45)+Comp(46);
SC_3=Comp(48)+Comp(49)+Comp(50)+Comp(51)+Comp(52)+Comp(53)+Comp(54)+Comp(55)+Co
mp(66)+Comp(67);
SC_4=Comp(68)+Comp(70)+Comp(72)+Comp(73)+Comp(74)+Comp(75)+Comp(76)+Comp(77)+Co
mp(78)+Comp(79);
SC_5=Comp(80)+Comp(81)+Comp(82)+Comp(83)+Comp(84)+Comp(85)+Comp(86)+Comp(87)+Co
mp(88)+Comp(89);
SC_6=Comp(90)+Comp(91)+Comp(92)+Comp(93)+Comp(94)+Comp(95)+Comp(96)+Comp(97)+Co
mp(98)+Comp(99);
SC_7=Comp(100)+Comp(101)+Comp(102)+Comp(103)+Comp(104)+Comp(105)+Comp(106)+Comp
(107)+Comp(108)+Comp(109);
SC_Liq=SC-(SC_2+SC_3+SC_4+SC_5+SC_6+SC_7) %Calculate seismic compression
without layers that had FSliq <1
```

Table E.1 Input parameters per soil layer for Soil Profile 2

Layer #	$N_{1,60}$	Fines Content (%)	σ'_{vo_test} (kPa)	Layer Thickness (m)	C_d (Skempton 1986)	C_{2D} (Lasley and Green 2012)
1	55	15	8.209	1	55	2.10
2	48	15	30.120	0.8	85	1.80
3	49	15	47.443	0.56	85	1.80
4	48	15	55.678	0.65	65	1.89
5	61	15	65.480	0.3	85	1.87
6	60	15	72.420	0.7	55	2.10
7	59	15	81.487	0.8	65	2.03
8	58	15	87.662	0.2	85	1.84
9	43	15	94.626	1	55	1.93
10	41	15	108.799	1.55	65	1.80
11	46	15	118.160	0.1	55	1.97
12	45	20	120.688	0.35	65	1.85
13	20	20	137.204	2.55	65	1.77
14	32	15	166.436	1.55	55	1.80
15	33	15	178.989	0.45	65	1.80
16	39	15	189.836	1.55	55	1.86
17	32	15	200.684	0.45	65	1.80
18	13	15	217.769	2.55	65	1.70
19	29	15	244.494	1.4	55	1.80
20	16	25	256.834	0.6	85	1.70
21	28	15	265.967	0.8	55	1.80
22	20	15	271.962	0.2	100	1.70
23	53	15	281.966	1.55	55	2.07
24	53	15	293.894	0.45	65	1.95
25	12	15	306.364	1.55	65	1.70
26	12	15	318.834	0.45	65	1.70
27	14	15	333.556	2.55	65	1.71
28	11	15	353.912	0.8	65	1.70
29	11	15	361.860	0.7	65	1.70
30	17	15	369.299	0.5	100	1.70
31	23	15	385.459	2.5	65	1.80
32	23	15	402.428	0.5	100	1.72
33	32	15	413.684	1.5	55	1.80
34	33	25	441.184	2.5	65	1.80
35	16	25	468.951	1.55	55	1.76
36	13	25	495.586	2.55	55	1.72
37	16	25	522.221	1.55	55	1.76
38	22	15	548.856	2.55	55	1.80
39	28	15	564.891	0.45	55	1.80

40	28	15	575.581	1.55	55	1.80
41	21	15	586.271	0.45	55	1.80
42	22	15	602.306	2.55	55	1.80
43	33	25	628.941	1.55	55	1.80
44	22	25	655.576	2.55	55	1.80
45	30	15	687.556	2.55	55	1.80
46	24	15	703.749	0.45	55	1.80
47	25	15	719.941	2.55	55	1.80
48	25	25	751.921	2.55	55	1.80
49	26	25	775.616	1	55	1.80
50	13	25	789.246	1.55	55	1.72
51	24	25	815.881	2.55	55	1.80
52	19	25	847.861	2.55	55	1.79
53	19	25	876.901	2	55	1.79
54	30	25	890.531	0.55	55	1.80
55	16	25	896.034	0.45	55	1.76
56	10	25	913.119	2.55	55	1.70
57	21	25	945.991	2.55	55	1.80
58	19	25	977.971	2.55	55	1.79
59	22	15	1009.95	2.55	55	1.80
60	23	15	1041.93	2.55	55	1.80
61	15	25	1073.91	2.55	55	1.75
62	14	25	1090.10	0.45	65	1.71
63	15	25	1098.01	1	55	1.75
64	24	25	1108.70	1	55	1.80
65	18	25	1141.41	3.38	145	1.70
66	17	15	1192.32	2.52	145	1.70
67	17	15	1213.04	0.04	145	1.70
68	17	15	1226.40	2.29	65	1.74
69	17	15	1239.98	0.07	100	1.70
70	19	15	1242.65	0.4	55	1.79
71	13	15	1247.46	0.5	55	1.70
72	21	15	1257.53	1.3	65	1.78
73	16	15	1285.44	2.7	145	1.70
74	16	15	1323.80	2.35	145	1.70
75	15	15	1357.98	2.15	145	1.70
76	15	15	1390.49	0.75	145	1.70
77	15	15	1399.02	0.35	100	1.70
78	15	15	1405.09	0.4	100	1.70

Table E.2 Input parameters per soil layer for Soil Profile 3

Layer #	$N_{1,60}$	Fines Content (%)	σ'_{vo_test} (kPa)	Layer Thickness (m)	C_d (Skempton 1986)	C_{2D} (Lasley and Green 2012)
1	78	15	2.67	0.31	58	2.10
2	76	15	7.71	0.19	110	1.85
3	74	15	13.35	0.38	58	2.10
4	72	15	19.37	0.22	110	1.82
5	70	15	30.02	0.65	110	1.80
6	70	15	36.62	0.25	58	2.10
7	68	15	46.55	1	145	1.80
8	71	15	56.22	0.2	58	2.10
9	71	15	58.09	0.1	110	1.80
10	71	15	60.40	0.28	58	2.10
11	73	15	66.11	0.52	110	1.83
12	73	15	70.72	0.05	110	1.82
13	73	15	71.93	0.15	58	2.10
14	73	15	75.56	0.35	110	1.82
15	72	15	79.73	0.25	58	2.10
16	72	15	83.50	0.3	110	1.81
17	71	15	88.60	0.5	58	2.10
18	69	15	93.70	0.3	110	1.80
19	78	15	99.77	0.45	110	1.86
20	77	15	106.25	0.35	110	1.86
21	77	15	109.99	0.17	58	2.10
22	77	15	112.35	0.18	110	1.86
23	78	15	116.81	0.37	110	1.86
24	77	15	121.30	0.28	58	2.10
25	78	15	125.73	0.55	58	2.10
26	78	15	132.32	0.45	110	1.86
27	78	15	137.19	0.23	58	2.10
28	78	15	142.63	0.52	125	1.80
29	71	15	149.74	0.45	100	1.87
30	72	15	154.01	0.17	110	1.82
31	30	15	170.52	2.83	58	1.80
32	27	15	188.20	0.45	65	1.80
33	20	15	196.43	1.06	58	1.80
34	21	25	202.42	0.04	125	1.70
35	24	15	205.65	0.45	100	1.73
36	59	15	216.56	1.5	58	2.10
37	58	15	232.60	1.5	58	2.10
38	51	15	241.91	0.16	110	1.80
39	41	15	245.08	0.29	100	1.80

40	29	15	252.56	1.05	58	1.80
41	9	15	258.52	0.05	100	1.70
42	9	15	262.07	0.45	100	1.70
43	9	15	281.03	2.95	65	1.70
44	9	25	297.21	0.05	110	1.70
45	12	25	305.89	1.55	58	1.70
46	14	15	316.74	0.45	100	1.70
47	33	15	335.34	3	58	1.80
48	27	15	354.28	0.45	100	1.75
49	15	25	363.06	1.1	58	1.74
50	12	15	389.42	2.95	58	1.70
51	12	15	405.60	0.05	110	1.70
52	13	15	408.90	0.45	100	1.70
53	16	15	417.41	1.05	58	1.75
54	16	25	423.35	0.05	100	1.70
55	18	15	426.57	0.45	100	1.70
56	36	15	443.90	2.7	58	1.80
57	39	15	460.76	0.3	110	1.80
58	39	15	467.55	0.15	110	1.80
59	38	15	475.45	1.25	58	1.81
60	38	15	484.56	0.3	110	1.79
61	36	15	502.75	2.95	58	1.80
62	36	15	518.93	0.05	110	1.78
63	35	15	535.37	3	58	1.80
64	33	15	553.54	0.4	58	1.80
65	33	15	556.08	0.05	110	1.76
66	27	15	564.77	1.55	58	1.80
67	21	15	581.34	1.55	58	1.80
68	23	15	592.03	0.45	58	1.80
69	43	25	610.47	3	58	1.89
70	19	15	644.86	2.55	58	1.78
71	34	15	679.24	3	58	1.80
72	23	15	711.74	2	58	1.80
73	23	15	724.83	0.45	58	1.80
74	28	15	740.87	2.55	58	1.80
75	26	15	756.90	0.45	58	1.80
76	17	25	775.34	3	58	1.76
77	17	25	801.98	1.1	58	1.76
78	17	25	813.20	1	58	1.76
79	17	15	839.30	3	58	1.76
80	27	15	876.09	3	58	1.80
81	27	15	905.67	1.65	58	1.80
82	27	15	919.83	1	58	1.80

83	24	15	943.53	2.55	58	1.80
84	24	15	980.85	3.55	58	1.80
85	21	15	1012.83	1.55	58	1.80
86	19	15	1026.46	1	58	1.78
87	18	25	1034.21	0.45	58	1.77
88	13	25	1052.65	3	58	1.71
89	12	25	1089.44	3	58	1.70
90	13	25	1119.02	1.65	58	1.72
91	14	25	1136.12	1.55	58	1.73
92	13	25	1156.53	0.6	145	1.70
93	14	25	1171.74	2.05	58	1.73
94	13	25	1183.08	0.05	100	1.70
95	14	25	1190.41	1.3	58	1.73
96	22	25	1199.38	0.25	100	1.71
97	14	25	1202.74	0.25	58	1.73
98	22	25	1213.79	1.2	100	1.71
99	13	25	1227.25	0.7	58	1.72
100	21	25	1241.51	1.3	110	1.70
101	21	25	1258.51	0.8	110	1.70
102	21	25	1275.18	1	110	1.70
103	21	25	1296.14	1.2	110	1.70
104	21	25	1313.95	1	110	1.70
105	12	25	1339.89	2.35	142	1.70
106	12	25	1374.07	2.15	145	1.70
107	11	25	1406.58	0.75	145	1.70
108	11	25	1415.11	0.35	100	1.70
109	11	25	1421.18	0.4	100	1.70